Imperial College London

Emergent Dynamics of Confluent Tissues in Homeostasis and Growth

Andrew Killeen

Supervised by
Dr. Chiu Fan Lee, *Dept. of Bioengineering*
Dr. Thibault Bertrand, *Dept. of Mathematics*

Thesis submitted for the degree of Doctor of Philosophy
Department of Bioengineering
Imperial College London
March, 2023

Declaration

I declare that the work presented here is entirely my own with the exception of material cited from publications other than my own and developments to the lattice-Boltzmann method presented in Chapter 4. The method for simulating the tissue boundary was developed by previous PhD candidate Dr. Benjamin Partridge. The research carried out using the model, and the synthesis of that study, is my own work.

Publications

The work presented in Chapter 2 has been published as: A. Killeen, T. Bertrand and C.F. Lee, "Polar fluctuations lead to extensile nematic behaviour in confluent tissues", *Physical Review Letters*, **128**, 078001, 2022

The work presented in Chapter 3 is being submitted for publication as: A. Killeen, T. Bertrand and C.F. Lee, "Machine learning topological defects in confluent tissues", 2023. The paper is being submitted for review in *Biophysical Reports*.

The work presented in Chapter 4 is being submitted for publication as: A. Killeen, B. Partridge, T. Bertrand and C.F. Lee, "Modeling growing confluent tissues using a lattice Boltzmann method: interface stability and fluctuations", 2023. The paper is being submitted for review in *Physical Review Research*.

Copyright

,

Acknowledgements

This work would not have been possible without numerous people, who offered insightful guidance, warm support or just generally kept me sane over the last four years. It is safe to say this thesis would not exist without the support of my supervisors Dr. Chiu Fan Lee and Dr. Thibault Bertrand. Your guidance, scientific knowledge and willingness to help when I was frequently banging my head against a wall has helped this work immeasurably. More importantly, beyond these pages, you have taught me so much about how to think about and approach scientific questions, as well as what makes an exceptional researcher and mentor, thank you.

My research groups have also been an enormous help over the course of my PhD, in particular Henry Alston, Dr. Shalabh Anand, John-Antonio Argyriadis, Patrick Jenstch, Sulaimaan Lim, Dr. Benjamin Partridge and Sam Whitby. Be it feedback on my work, sharing your own ideas and knowledge, or simply being an interesting and engaging group to be around, thank you. I would also like to thank Prof. Cristina Lo Celso and her lab for exposing me to the terrifyingly complicated world of biology, teaching me so much about the incredible work they do, and putting up with my physics based group presentations. In particular, I thank Dr. Constandina Pospori for her guidance and encouragement in our work together.

I must also thank the members of my CDT, particularly Ali, Geraldine, Henrik, Henry, James, Lorna, Sam and Sophia. Whether it was a pub quiz, lockdown zoom call, watching an overzealous blues band or just a lunch where we discuss our work, you all had a hand in helping my research and keeping me sane, thank you.

Away from university, I would like to thank the small army of friends and family who have offered love, support and encouragement over the last four years. I could not possibly name everyone, but you have all had a hand in helping me be able to finish this work. In particular, I would like to thank my housemates throughout my PhD, Ant, Elliott, Kyle and Will. From lively debates to morning motivators, you ensured there was a never a dull moment either before I left for, or when I came home from, a long day on campus. Thank you as well to Christie and Lily for being so supportive, of my work and cooking attempts, while I have been writing up. I would also like to thank Joe and Sean, our trips and adventures over the last few years have been the perfect break when I've needed time away from science.

Finally, I would like to thank my parents, Brian and Suzanne, and my sister Daisy. While everyone mentioned on these pages had a hand in helping me complete this thesis, without you I would not have even been able to start it. For this, and so much more, thank you.

Abstract

Emergent dynamics in confluent tissues play an important role in many biological processes. Here, we study these dynamics through the lens of active matter physics, specifically focussing on two emergent phenomena: nematic collective behaviour in homeostasis and the dynamics of a growing tissue boundary.

We first examine the emergence of extensile nematic behaviour at the tissue level, and how a collection of contractile cells can give rise to it. By constructing and analysing a linearised hydrodynamic model, we show that this extensile behaviour results from fluctuating polar forces that arise from cell-substrate interactions. We show that polar fluctuations generically lead to extensile behaviour in the absence active contractile forces, and can still generate extensile behaviour in their presence. We then confirm our results by analysing the dynamics of nematic defects in a cell-based numerical model.

In order to analyse these nematic defects, one must have a reliable and efficient means of detecting them, which currently is not the case for many confluent tissues. Due to this, we then develop a machine learning model to detect nematic defects in confluent tissues that is readily implementable on experimental images of cell layers. We demonstrate that our model outperforms current detection techniques and that this manifests itself in our method requiring less data to accurately capture defect properties, improving the accuracy of experimental data interpretation.

Confluent tissue dynamics are not only important in homeostasis, but also during growth, such as in wound healing. As such, we also examine the dynamics of the

boundary of a growing tissue. We study this problem using a novel lattice-Boltzmann method for a growing tissue with a moving front. We find that, at small system sizes, the interface fluctuations grow with scaling in agreement with the Kardar-Parisi-Zhang universality class. However, when using a density-dependent growth regime, we find the onset of a novel instability at larger system sizes, which we develop an analytical theory to characterise.

In this thesis we have developed new fundamental understanding of confluent tissue dynamics in homeostasis and the physics of growing tissue interface stability. We have also developed new defect detection methodology and simulation methods for modelling growing tissues. The tools and understanding generated here provide fruitful avenues of future research, and equip biophysicists to tackle further questions, in these important biological systems.

Contents

List of Figures

List of Tables

Chapter 1

Introduction

The incredible complexity of living matter, and the hierarchical structure that brings about this complexity, is fundamental to the beauty of these systems and our fascination in them. It also makes them very hard to describe with physical theories. This is because at each level of complexity entirely new behaviour emerges, that can be very different from what one would expect to find from studying the individual constituents in isolation at the level below [1]. One cannot discern the function of proteins from analysing individual amino acids in much the same way that these individual proteins do not reveal the behaviour of organelles, or these organelles the dynamics of cells. One must study how different constituents interact to begin to connect dynamics at one scale to behaviour that emerges at another.

However, this hierarchical structure can also bring about a separation of scales that allows complexity to be stripped away and makes a physical description possible. It means one can understand dynamics at a given level in terms of the constituent units that comprise it, without worrying about the amazing complexity at smaller scales that brought about the behaviour of those constituents. This allows us to understand tissue level dynamics - as well as the multitude of biological processes that depend on it - from the behaviour and interactions of individual cells, without

worrying ourselves with having a complete description of the contents of these cells.

In this thesis, we are concerned with understanding and characterising emergent behaviour in confluent tissues, densely packed tissues in which cells are in contact with each other on all sides, due to the role they play in fundamental biological processes [2]. As we have discussed, one can do this by delineating how cellular processes and interactions manifest in tissue level dynamics. However, in addition to understanding how these dynamics emerge, we will also focus on accurately identifying and classifying tissue scale phenomena, as this can be a challenge in itself and provide insight into the system, along with being a prerequisite for determining the cellular mechanisms governing the phenomena.

1.1 Confluent tissues

While we do not need a complete understanding of cellular biology to study the dynamics of confluent tissues, we do need an understanding of the forces generated by and between cells, along with the different tissue level phenomena that arise from these forces. An idea of how these forces and interactions arise is also instructive and helps in formulating suitable descriptions of the tissue. As such, we will first delineate these forces and interactions before discussing some of the phenomena they lead to.

1.1.1 Single cells

Cells generate forces through their cytoskeleton, which also gives cells their rigidity and allows them to withstand tension. The cytoskeleton in eukaryotes can be broadly split into three components: microtubules, intermediate filaments and microfilaments (Fig. 1.1). Microtubules, constructed from the polymer tubulin, are

responsible for intracellular transport of organelles such as mitochondria, they also resist compressive forces [3]. Intermediate filaments are made from a variety of proteins, such as keratin in epithelial layers [4]. They maintain cell shape and can bear tension, they also serve to anchor organelles in position where necessary. Most pertinent to the study of tissues dynamics is the final component, microfilaments, which are composed of the protein actin [3].

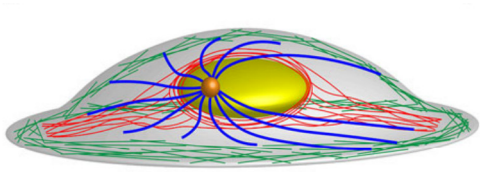

Figure 1.1: Schematic of the cytoskeleton. The cytoskeleton of the cell has three principal components: the actin cortex (green), intermediate filaments (red) and microtubules (blue). The nucleus is also shown in yellow. Microtubules branch off from the centre of the cell to aid in transporting proteins and organelles around the cell. Intermediate filaments are dispersed throughout the cell to provide rigidity, whereas actin filaments are concentrated towards the periphery of the cell. Adapted from [5]

Actin filaments, together with myosin molecular motors, are the apparatus that allow cells to actively generate forces: the actomyosin cortex. Concentrated around the periphery of the cell, these actin filaments act as tracks for myosin proteins that 'walk' along them, pulling the filament and generating a contractile force. These forces can then be transmitted to a substrate via protein complexes known as focal adhesions. For the cell to move there must be an asymmetry in the strength of these cell-substrate interactions. To accomplish this, the cell polarises and projects microfilament-based protrusions out through the cell membrane called lamellipodia or filopodia, which pull the cell forward in the direction of the protrusions while focal adhesions towards the rear of the cell are dismantled and the cortex retracts (Fig. 1.2). As this process requires the constant renewal of focal adhesions, and actomyosin machinery to which they bind, microfilaments are less stable than intermediate filaments and microtubules, whose demands are longer lasting.

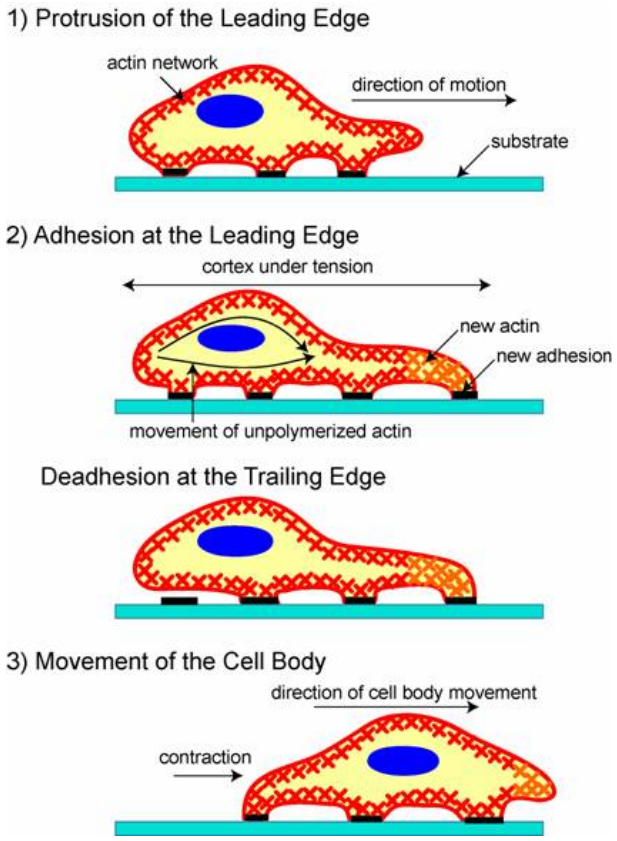

Figure 1.2: Self-propulsion of a single cell. To migrate in a given direction, cells (1) generate actin based protrusions from their actin cortex beyond their forward most focal adhesions, putting the cortex under tension. (2) They then form new focal adhesions under these protrusions. While doing this they dismantle focal adhesions at the rear of the cell, with unpolymerised actin being transported to the front to build the new adhesions. (3) The cortex at the rear of the cell is now free to contract, moving the cell body forward and starting the cycle again. Adapted from [6].

These active traction forces are balanced by friction between the cell and the substrate it is crawling on. As cell migration occurs at very low Reynolds numbers, where the dynamics are dominated by dissipative forces, this frictional force is usually taken to be proportional to the velocity of the cell in a similar manner to viscous drag [7].

A further source of force in single cells are those generated during cell division. While the process of mitosis is comprised of many steps involving a variety of cellular apparatus, from the perspective of cell level forces generated, these steps manifest as a dipolar force, perpendicular to the axis about which the cell divides [8]. While

this force may initially pull inwards, in a process known as mitotic rounding, the primary effect of division on other cells is a force pushing outwards along the same axis as the cell divides [9].

1.1.2 Cell-cell interactions

As discussed previously, in order to study the emergent properties of confluent tissues, as well as the forces generated by single cells we also need to understand how these cells interact with one another. These interactions can be long range, with cells secreting molecules that react with receptors on cells some finite distance away. They can also be more direct and immediate in the form of cell-cell contacts, which are more relevant to confluent tissues where cells are, by definition, in contact with other cells on all sides.

Such contacts can prompt the assembly of transmembrane protein complexes that physically bind the cytoskeleton of one cell to another, creating an adhesive force. These links between cells allow for force transmission and the support of forces throughout the tissue, giving it a finite bulk and shear modulus [10]. Due to the elasticity of the cytoskeleton, these junctions can also lead to the generation of repulsive forces between cells, in an effort to restore their original shape when compressed [11]. However, at longer times cells can regulate these forces by changing their volume via gap junctions, channels that form between cells that allow the transfer of ions and other molecules, with other cells [12]. Cell-cell junctions also generate frictional forces between cells as they move past one another, as this process is often mediated by the attachment and detachment of these junctions [13]. Some of these interactions, and others discussed below, are summarised in Fig. 1.3.

Cells can also construct junctions that support the transmission of active forces. Certain cell-cell junctions, known as desmosomes, do not support this kind of trans-

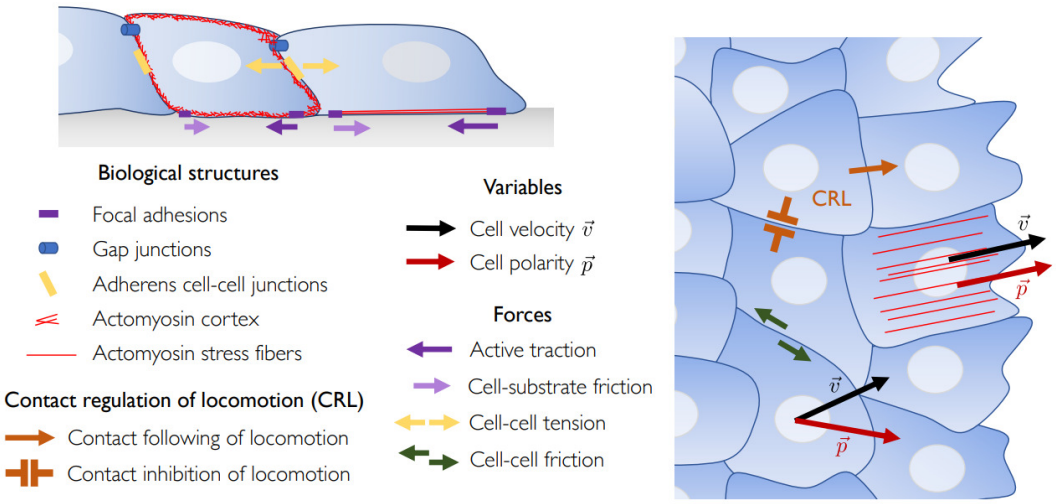

Figure 1.3: Forces and interactions in confluent tissues. Schematic overview - a (left) sideview and (right) top view - of some of the interactions and forces in confluent tissue layers. Adapted from [14].

mission as they specifically bind to intermediate filaments [15]. However, adherens and tight junctions link to actin filaments [16], with tight junctions also linking to microtubules [17], physically linking together the actomyosin machinery of one cell to another. This means that, when polarised, cells can transmit polar forces between cells and generate active forces at the tissue level.

Along with the transmission of forces between cells, they can also interact in more subtle ways that affect their polarity. Forces from neighbouring cells transmitted via cell-cell junctions can lead cells to regulate their own polarity internally and reorient their polarity in another direction. This is known as contact regulation of locomotion (CRL) [14]. CRL encompasses the phenomena of contact inhibition of locomotion (CIL), whereby cells reverse their polarity direction when their lamellipodia collide during a head on collision, but also contact following of locomotion (CFL). CFL is where cells tend to increase their polarisation upon contact with the rear of a polarised cell. In this scenario cells form 'cryptic' lamellipodia, or c-lamellipodia, that extend underneath the cell in front and allow for longer range ordering in the orientation of traction forces [18]. In this way cells can internally adapt their polarity

to align with the direction of the force exerted upon them. Adherens junctions are known to be crucial for this process and the stable formation of c-lamellipodia, further underlining the importance of these junctions in generating tissue level forces [19].

There is also interplay between cell-cell interactions and the cell-substrate interactions discussed in Section 1.1.1. This is due to lots of the machinery involved in producing these interactions being common to many of them. This leads to situations where increases in strength in one interaction occur at the expense of another, if there is a finite supply of a protein required for both interactions within the cell. An example of this is when active force transmission between cells is decreased. This was carried out in a study on a MDCK epithelial cell line that were modified such that they could not form E-cadherin junctions, a type of adherens junction [20]. It was found that E-cadherin knockout cells exerted larger forces on the substrate due to an increased number and strength of focal adhesions. The study found that this was accompanied by changes in the distribution of vinculin, a protein used to form both E-cadherin junctions and focal adhesions, in the different cell types. In E-cadherin knockout tissues, vinculin was concentrated at the cell-substrate interface, as opposed to the cell-cell interfaces in wild type tissues, suggesting having more of this protein available in E-cadherin knockout cells allows stronger cell-substrate interactions. This underlines the difficulty in isolating each of these interactions and examining their role in various phenomena experimentally.

1.1.3 Emergent behaviour

Nematic alignment and defects

The forces and interactions described manifest in a variety of tissue scale phenomena in confluent tissues, which play crucial roles in homeostatic and developmental

processes. Perhaps the most straightforward to understand is the emergence of large scale order in cellular alignment (Fig. 1.4a). We will define this type of alignment, known as nematic alignment, more thoroughly in Section 1.2.1. Here we just seek to describe the phenomenon and its role in biological processes. If cells are elongated in shape, at high densities - such as in confluent layers of fibroblasts - steric repulsion causes cells to align along their long axes, sometimes over millimetre length-scales [21]. However, cells that are round in shape can also deform and exhibit nematic order at high densities, such as epithelial cells [22]. This deformation can be due to confinement but also due to active forces in the tissue, where forces exerted on cells can deform and elongate them in the same direction locally. In other cases, persistent application of force can lead cells to remodel their cytoskeletons such that they elongate either parallel or perpendicular the direction of the force [23, 24]. This orientational order plays an important role in a variety of biological processes. It allows for macroscopic contraction of muscle tissues [25] and organising osteons to give bones their necessary mechanical properties [26]. It also improves endothelium integrity in blood vessels, protecting against the initiation of atherosclerosis [27].

More challenging to understand than the presence of this alignment is the presence of defects, or singularities, in this alignment. In many systems exhibiting nematic order two types are principally seen: comet-shaped and trefoil-shaped defects (Fig. 1.4b). Again, we characterise these defects more thoroughly, and discuss why they take the forms they do, and in Section 1.2.1, here we seek to discuss their significance in confluent tissues. These defects can arise in the tissue as it grows [28], or be spontaneously generated within the bulk [29]. These defects are not merely a lack of alignment, they are supercellular structures that can exist on length-scales far larger than individual cells. The mechanisms governing their emergence and dynamics is unclear in some cases, and deciphering them is becoming a pressing question, as these defects have been found to be involved in an increasingly wide array of biological processes. Comet-shaped defects have been found to control

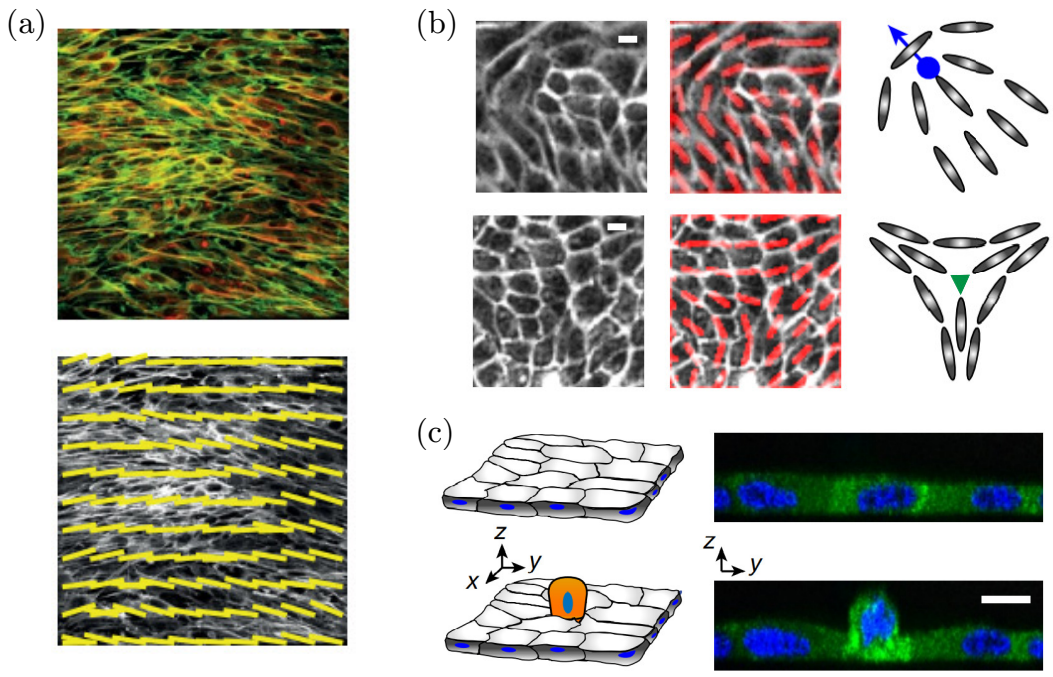

Figure 1.4: Emergent phenomena in confluent tissues. (a) Orientation alignment of fibroblasts,adapted from [28]. Top is a flourescent image of the tissue, bottom is the average local orientation direction overlaid on top of the image. (b) comet-shaped (top) and trefoil shaped (bottom) defects in cell alignment in an epithelial layer, adapted from [29]. (Left) experimental images of the defects in the cell layer, (middle) experimental images with the mean local cell orientation overlaid on top and (right) schematics of idealised defects. (c) Schematic and experimental images of a a cell being extruded from an epithelial layer, adapted from [29].

the collective dynamics of confluent layers of neural progenitor cells [30] and have been highlighted as organisation centres during Hydra morphonegenesis [31]. They also mediate processes in densely packed bacterial systems, triggering the formation of fruiting bodies in Myxococcus Xanthus colonies [32] as well as facilitating collective motion in Pseudomonas aeruginosa [33] and E. Coli colonies [34], while trefoil-shaped defects have been associated with controlling areas of cell depletion in bacterial colonies [32].

Furthermore, comet-shaped defects also play a functional role in an important homeostatic process known as cell extrusion. Extrusion is the process by which cellular layers remove unnecessary or unwanted cells. As opposed to the cell being

slowly broken down and removed via phagocytosis, the cell is quickly squeezed out from the layer, preserving its integrity (Fig. 1.4c). Cells can be extruded for a variety of reasons. Apoptotic cells are extruded by signalling to neighbouring cells, who form an actomyosin ring around the cell via adherens junctions before squeezing it out [35]. Live and healthy cells can also be extruded from the tissue. This was first reported in zebrafish models and is related to how much compression the system is under; it has been hypothesised to be a method for reducing overcrowding of cells in these systems [36]. Comet-shaped defects have been found to provoke apoptotic cell extrusion in epithelial layers [29]. The defects were found to generate compressive stresses in the head portion of the defect that triggered the activation of cell death signalling. The mechanisms driving defect formation, however, remain unclear.

In comparison to extrusion, compression plays an opposing role in cell proliferation, where it impedes rather than facilitates [37]. It has been shown to be suppressed by compressive forces, leading to cells becoming quiescent at sufficiently high densities [38]. Moreover, cells under tension have been found to divide preferentially about an axis perpendicular to the direction of the applied tension, as a means of reducing the stress experienced [39].

Collective motion and interface dynamics

Collective motion, the coordinated movement of many cells in a given direction, is vital for a variety of processes, such as embryonic development [40] and cancer cell invasion [41]. It often requires the large scale organisation of cells polarity direction via adherens junctions [42], with these anisotropic polar forces transmitted over tens of cells in distance [43]. Another process that relies on this phenomena is wound healing. During wound healing, cells polarise outwards in the direction of the leading edge to close the wound, with this effect transmitted into the bulk from the edge, albeit with the response diminishing with distance into the tissue [44].

The mechanism governing the dynamics of the tissue edge during this process, and its dynamics more generally, is interesting in itself, and has been the subject of much study in recent years. This is due to the tissue boundary not advancing in an ordered manner, but rather a chaotic one (Fig. 1.5a). Due to this, it is unclear precisely how to describe the dynamics, let alone how they emerge. The disordered nature of the interface growth has led studies to characterise the dynamics as being governed by the onset of an instability at the tissue interface, and numerous theoretical studies have found instabilities to emerge at the boundary of tissue models [14, 45, 46, 47]. Due to the links to collective motion, these studies tend to focus on, and have successfully delineated, how active traction forces can precipitate an instability, with the role of cell proliferation less explored.

However, instabilities are characterised by the growth of perturbations of a certain

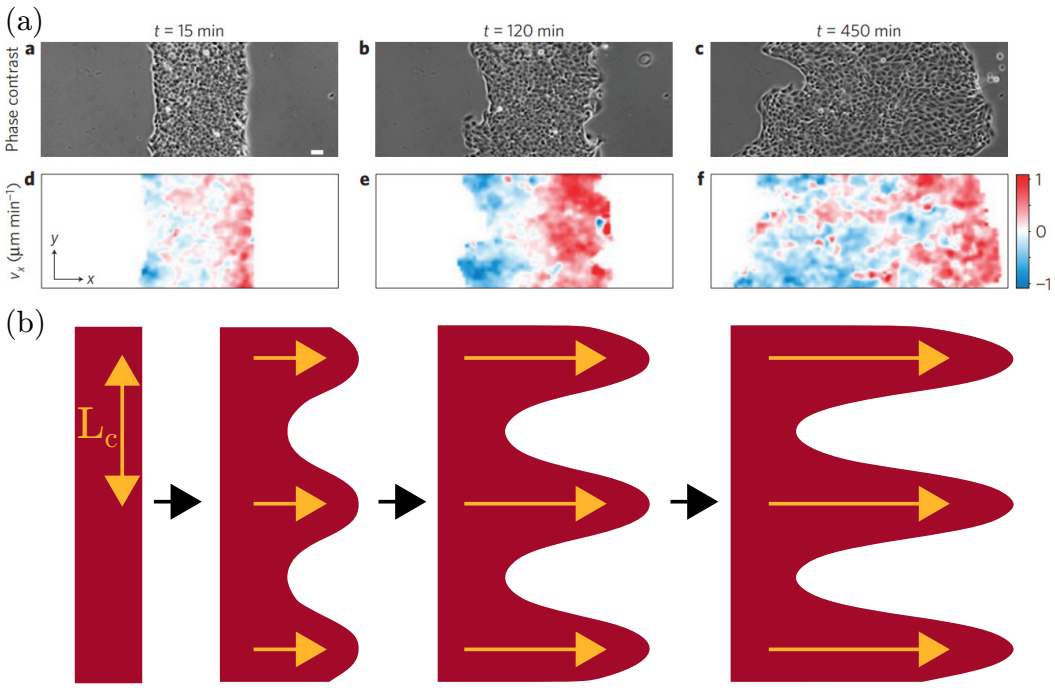

Figure 1.5: Collective migration and dynamics at the tissue edge. (a) Images (top) and heatmaps showing horizontal velocity (bottom) of expanding epithelial layer, adapted from [48]. (b) Schematic of the dynamics of a tissue edge if it were unstable. A certain wavelength of perturbation L_c would grow fastest, meaning with time the tissue edge should undulate with the wavelength to a greater degree.

wavelength (Fig. 1.5b), while the edge of an advancing tissue, such as in Fig. 1.5a is usually not well defined by fluctuations of a single wavelength. The fluctuations seen in the interface could, therefore, just be due to the intrinsic noise and fluctuations within the system. Experimental studies have sought to characterise this by examining how the width of the interface scales in space and time [49, 50, 51, 52]. The idea behind this is that, if the scaling for space and time can each be described by a single exponent, the values of these exponents can be used to deduce the mechanism by which the interface is growing. Experimental studies have thus far measured conflicting values for these exponents, meaning the processes governing the dynamics of the interface are still unclear.

1.2 Active matter

A suitable description of confluent tissues is a prerequisite to characterising these dynamics and the biological processes dependent upon them. The dynamics of the cells that compose these tissues arise from the internal consumption of energy within cells, allowing cells to exert forces on the substrate as well as each other. As such, active matter provides a natural framework for describing confluent tissues.

Active matter is an emergent field of physics for describing far from equilibrium many-body systems where the system is driven from equilibrium from energy expended by the individual constituents themselves [53]. As many biological systems consist of distinct constituents that constantly convert chemical energy to mechanical work to drive the system far from equilibrium, active matter offers a fruitful avenue for modelling such systems, be it herds of sheep [54], flocks of birds [55], colonies of bacteria [56], cytoskeletal filaments [57] or confluent tissues [58]. Given the diversity of systems active matter aims to describe, a plethora of different models, not all of them relevant to confluent tissues, have been developed that can

broadly be divided into different classes based on the different forces and interactions present in these systems [53]. We will first discuss these classes and how they relate to confluent tissues before focussing on specific modelling approaches taken to describe these systems, with a focus on cellular systems.

1.2.1 Classifying active systems

Dry and wet

Perhaps the primary distinction to make between active matter systems is whether they are wet or dry, meaning whether they are momentum conserving or not. In wet systems, active constituents are immersed in a medium whose dynamics are relevant and so must be properly resolved. This means momentum must be conserved between constituents and the medium, as the constituents transfer momentum to the medium while they self-propel and move around. To properly account for momentum conservation, the medium may also transfer momentum to the agents. This two-way coupling is encoded in the form of hydrodynamics interactions between individual agents. Examples of wet systems include swimmers such as spermatozoa [59]. The dynamics of the medium are generally deemed relevant, and the system described as wet, when the forces generated in the medium by the constituents generate hydrodynamic soft modes. Examples of such systems include suspensions of bacteria [60] or microtubules [61].

In dry systems, the dynamics of the medium in which active constituents are seeking to self-propel are either irrelevant to understanding the system or negligible, acting as a momentum sink upon which constituents can exert force. Hence momentum exchange between the particles and the medium need not be considered, and momentum is not conserved. Examples of dry systems in which the dynamics of the medium are negligible are flocks of birds [55]. In such systems where one is only con-

cerned with the dynamics of the birds, the birds can be considered as self-propelled particles as, assuming there is no wind, the air is far too compressible to induce any hydrodynamic soft modes. Herds of animals that move on land are an example of a dry system with a momentum sink because the animals can exert a force on the ground without it moving [54]. As such, confluent tissues containing cells that crawl on a rigid substrate are dry systems. This means that we need not conserve momentum to describe the system and need only model the cells themselves.

Polar and Nematic

The other important distinction between different types of active materials is whether or not the system is polar. In polar systems, constituents are asymmetric, either in their shape or dynamics, or both. In other words, each constituent has a clear 'head' and 'tail' and can be described by an arrow pointing towards the head. Apolar systems are systems where there is no distinguishable head and tail. While there are different classes of apolar systems, by far the most relevant to biology are nematic systems. In nematic systems, constituents still display a clear orientation, for example by being elongated as in many biological systems, but do not have a distinguishable head or tail along that orientation. They can therefore be described by a bar, or director, as opposed to an arrow. This indistinction could be due to the particle periodically reversing the direction of force generation, such that it oscillates back and forth, like *Myxococcus Xanthus* [32] or that the forces it generates are dipolar, such as the forces generated during cell division [9].

When systems are referred to as polar or nematic it is often in relation to the type of order they are exhibiting. If a system is displaying polar order, all the arrows that describe the constituents would be, at least locally, aligned in the same direction such that there is a non-zero mean force, and non-zero macroscopic velocity if the constituents are motile, in the direction the particles are aligned (Fig. 1.6a). Conflu-

ent tissues undergoing collective motion, discussed in Section 1.1.3, are an example of polar order being exhibited. However, confluent tissues may also display nematic order, usually through the alignment of cells' orientation, as was also highlighted in Section 1.1.3.

Nematic order is characterised by constituents showing local alignment in their orientations but with no discernible head or tail along this orientation (Fig. 1.6b). Consequently, a system of polar particles may exhibit nematic order if the particles move along some common axis but, due to the interactions between particles, show no bias in their direction of travel along that axis (Fig. 1.6c) [62]. For example, individual microtubules display a clear polarity, but when combined in a homogeneous mixture with molecular motors, the emerging order and, consequently, the emerging phenomena are nematic [61]. Similarly, cells in a tissue can be thought of as polar as they attempt to crawl on a substrate. However, if this crawling is not coordinated there is no polar order, but steric interactions between cells may align their long axes and generate nematic order. This demonstrates an important point: the order a system displays, and the emergent behaviour this order permits, is due to the interactions between constituents as well as the behaviour of the constituents themselves.

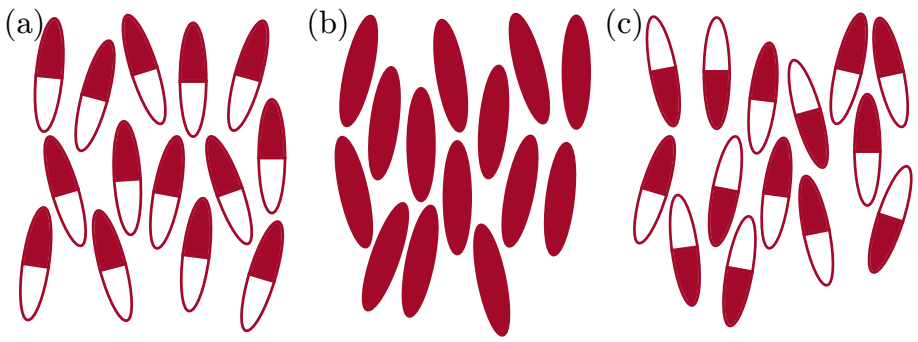

Figure 1.6: Orientational order in confluent tissues. (a)Polar particles exhibiting polar order, red represents the head of the particle and white the tail. (b) Nematic particles exhibiting nematic order and (c) polar particles aligning nematically, thus exhibiting nematic order are larger length-scales.

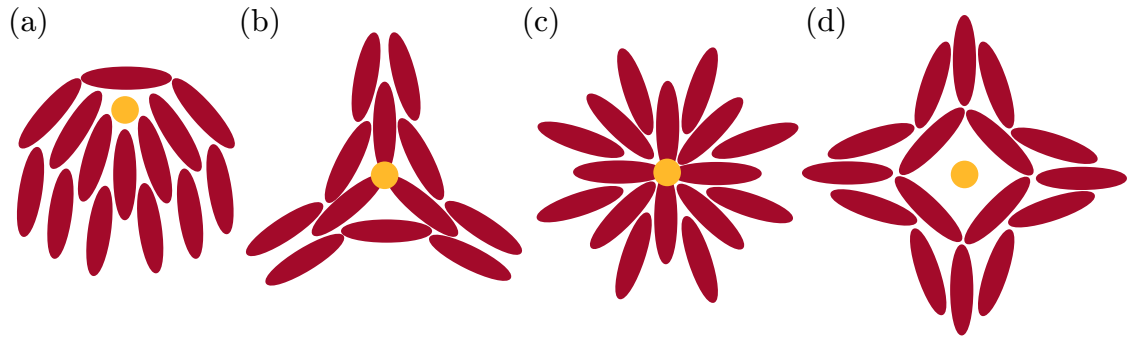

Figure 1.7: Defect types found in active systems. Topological defects of charge (a) $+1/2$, (b) $-1/2$, (c) $+1$ and (d) -1

Systems of polar or nematic particles can display no order in the alignment of either their polar or nematic field, if so the system is said to be isotropic. When order does emerge, due to either fluctuations or the initial conditions of the system, it is rarely perfect and the orientation of the fields often vary in space and time. Topological defects, or singularities, in these fields then arise where this variation is discontinuous. While there are, in theory, infinitely many types of topological defects one can observe, the symmetries of the system dictate and restrict the types of defects that stably form. In nematic systems, the types preferred are the comet and trefoil shaped defects seen in Section 1.1.3, known as $+1/2$ and $-1/2$ defects respectively. In polar systems, however, ± 1 defects are more prevalent [63]. Examples of the integer defects seen in polar systems, and half-integer nematic defects, are shown in Fig. 1.7.

Nematic systems favour $\pm 1/2$ defects over ± 1 as they lead to less distortion of the nematic field so require less energy to be created and sustained. They are not seen in polar systems, however, as the broken head-tail symmetry leads to completely anti-aligned particles adjacent to each other within the defect, which has a high energetic cost due to the large distortion in the polar field. Due to this, ± 1 defects are favoured as they allow constituents better local alignment.

Topological defects are characterised and so-called due to their topological charge,

or 'winding number'. This is the amount the field in question rotates as a closed loop is traversed around the centre of the defect [64] (Fig. 1.8). The half integer defects found in nematic systems are so called because the nematic field rotates by half a full rotation, or π radians, around the loop. The sign of the defects depends on whether the rotation of the nematic field is in the same direction as the direction in which the loop is being traversed. If the nematic field rotates clockwise as the loop is traversed in a clockwise direction, the defect is positive; if it rotates anti-clockwise, it is negative. The same is true for integer defects but with the field undergoing a full rotation.

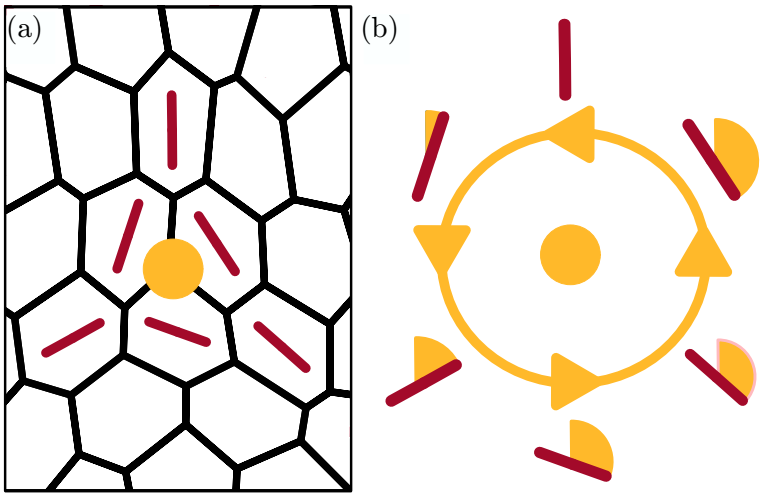

Figure 1.8: Calculating defect winding number.(a) Example of a trefoil-shaped $-1/2$ defects in a confluent cell layer with the orientation of the long axis of each cell plotted in red. (b) Characterising this defect by its winding number. As a closed loop is traversed around the $-1/2$ defect, the orientation of the cells rotate by π radians (half a full rotation), hence the defect is half-integer. The sign of the defect is negative as the cells rotate in the opposite direction to the direction of travel around the loop

Extensile and contractile

As nematic systems are defined by constituents being head-tail symmetric, for a system to be an active nematic the forces generated by individual constituents must also be head tail symmetric. This leads to a final important distinction is to be

made within active nematic systems. This is whether the system is extensile or contractile. In the context of active matter, these terms originally referred to the forces generated in the surrounding medium of a wet active system as swimmers self-propel. If a swimmer self-propels by pushing fluid out along its long-axis behind it, such as a spermatozoa, the dipolar forces generated in the fluid are said to be extensile (Fig. 1.9a). Conversely, if self-propulsion stems from the swimmer pulling itself forward through the fluid, such as *Chlamydomonas* algae [65], then the forces generated in the fluid pull in along its long axis and are said to contractile (Fig. 1.9b). These terms are now commonly applied to dry systems based on the type of force generated within the constituents themselves. If the force generated pushes out along its long axis, the constituents are said to be extensile, whereas if it pulls in it is contractile (Fig. 1.9c). As the actomyosin cortex is contractile, individual cells exhibit contractile forces, although they also generate extensile forces during cell division [7].

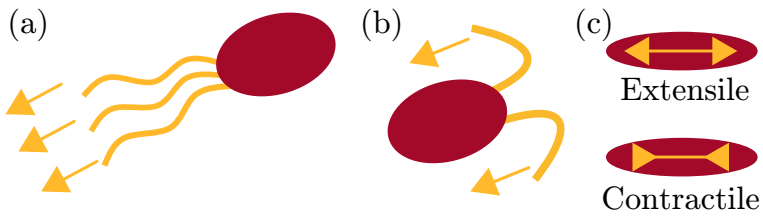

Figure 1.9: Extensile and contractile active nematic constituents. (a) Swimmers that self-propel by pushing fluid out behind them are known as extensile. (b) Swimmers pull fluid towards them are contractile. (c) Dry systems are extensile or contractile based upon the direction direction of the force dipole generated by constituents.

This microscopic dichotomy manifests itself macroscopically in the dynamics of nematic $+1/2$ defects. Due to their three-fold symmetry, the force generated around $-1/2$ defects balance and they display no net self-propulsion. However, due to their polarised shape, $+1/2$ defects generate a net self-propulsion force that depends on the nature of the active forces in the system. If they are extensile the $+1/2$ defect is pushed in a tail to head direction, whereas contractile forces pull the defect in a head to tail direction (Fig. 1.10) [66]. As individual cells are contractile, one would

anticipate that defects in confluent tissues would exhibit head to tail motion when the appear, which in some systems, such as collections of fibroblasts [28], they do. However, other tissue types display extensile defect motion, such as MDCK epithelial layers [29, 20] and neural progenitor cells [30], suggesting a switch in behaviour at the tissue level from the cell level that is not fully understood.

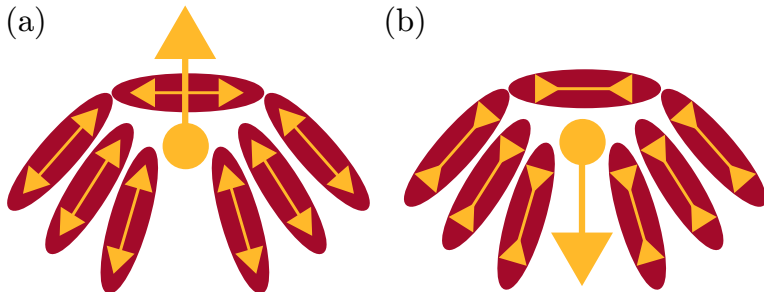

Figure 1.10: Defect motion under active nematic forces. (a) Extensile forces induce a tail-to-head motion in +1/2 defects and (b) contractile forces induce a head-to-tail motion.

1.2.2 Modelling approaches

There are myriad techniques for modelling the various types of systems and phenomena outlined above, although they can broadly be split into two categories: microscopic or coarse-grained. Microscopic approaches model the dynamics of each individual constituent, whereas coarse-grained models capture the local mean dynamics of a collection of constituents. As rules and parameters governing the dynamics and interactions of individual particles are explicitly established in microscopic models, they can be very useful for studying how macroscopic phenomena can arise from a minimal set of rules. Also, they provide a precise link between the microscopic parameters and these phenomena. However, explicitly modelling every constituent leads to an increase in computational complexity as the number of agents increases, meaning coarse-grained models are more appropriate for studying phenomena at hydrodynamic length-scales.

Microscopic

Vicsek Model

There are a wide variety of microscopic models, building in complexity from the Vicsek model, perhaps the most well-known. The Vicsek model consists of polar point particles that all move with the same constant velocity and seek to align their velocity with that of their neighbours [67]. This is done by each particle reorienting its polarity vector to that of the mean velocity direction of all neighbouring particles within some interaction range, with the addition of some random noise (Fig. 1.11). In the original model a complete reorientation is done at each time-step in the simulation, but it can also be implemented with a delay such that the polarity vector reorients over a given timescale [68]. These are minimal methods for introducing polarity alignment interactions. However, unlike those discussed in Section 1.1.2, where these interactions are a result of the force one cell exerts on another, here they are the result of a constituent 'sensing' the behaviour of nearby constituents in a more abstract way.

Like confluent tissues, this system can exhibit collective motion if at sufficiently low noise strengths or high particle densities. Many variations of this original model

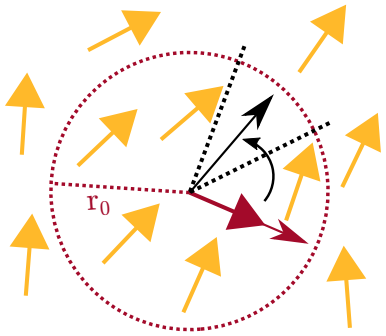

Figure 1.11: Schematic of the Vicsek model. Point particles, represented by arrows, interact with other particles with in some interaction range r_0. The seek to align their velocity (red arrow) with the mean velocity of other particles they are interacting with (black arrow), with additional random fluctuations (black dashed lines).

have been developed, such as the inclusion of alignment with topological nearest neighbours as opposed to neighbours within a given distance [69] or nematic alignment interactions between particles [62], which all show some transition to polar or nematic order. While the Vicsek model may be appropriate for capturing systems such as flocks of birds [70], where constituents are not in contact and interact over a finite distance, it is not appropriate for systems such as confluent cell layers where constituents are by definition always in contact with one another and so always, at a minimum, interact sterically.

Active Brownian particles

The simplest models to incorporate these volume exclusion effects are active Brownian particles (ABPs). While *a priori* point particles, ABPs are often implemented as self-propelled spherical particles, that can also undergo spatial diffusion as well as fluctuations in the direction of their polarity vector, and interact via hard or softcore repulsive energy potentials. Variations of this can introduce more biologically relevant forces, such as attractive forces between particles to model cell-cell adhesion [71]. Additionally, ABPs are usually modelled in the overdamped limit where inertia is negligible and dynamics are dominated by friction, the regime in which confluent tissues also operate. ABPs can have the same alignment interactions as in Vicsek models, with the additional option that now the particle can seek to align its polarity vector with that of its own velocity, as opposed to that of its neighbours. This is due to velocity and polarity no longer necessarily being the same due to steric interactions.

If the system is overdamped, this velocity corresponds to the forces being exerted on the particle and so this polarity realignment more accurately reflects the alignment interactions in confluent tissues, where cells reorient their polarities in response to the forces exerted on them by other cells. Inclusion of these interactions led to good qualitative agreement between an ABP model with softcore repulsion

and epithelial tissue dynamics [72], although obviously ABPs can only begin to appropriately describe confluent tissues at very high particle densities. Using non-spherical particles introduces additional repulsive torques to the steric interactions [73]. In the case of elongated, rod-shaped particles, these torques promote nematic alignment and can lead to a transition from an isotropic to nematic state at sufficiently high densities [74], similar to what is seen in systems of spindle shaped cells [28].

While the models discussed thus far are primarily biologically inspired and illustrate how generic interactions between individual constituents can spawn larger scale emergent phenomena, they were not developed with the express purpose of describing confluent tissues. Other modelling approaches, where the forces and interactions are explicitly based on those experienced by cells in these systems, promise more insight into these biological systems.

Cellular Potts model

The first such model to attempt this was the Cellular Potts model (CPM), a lattice based model where contiguous portions of the lattice are grouped together to form cells (Fig. 1.12a) [75]. The dynamics of the cells minimise a Hamiltonian with terms that account for the compressibility of cells and interfacial tensions between neighbouring lattice sites belonging to different cells. The model is then updated using a Monte Carlo scheme with Metropolis dynamics. Traction forces can implemented by decreasing the energy for configurations whose cells' centre of mass moves in the direction of its polarity vector. CPMs have been used to study velocity correlations in confluent tissues [76] and fingering instabilities in growing tissue fronts [77]. However, it is unclear how well these relaxational dynamics naturally describe the far from equilibrium nature of active forces in confluent tissues.

Phase field model

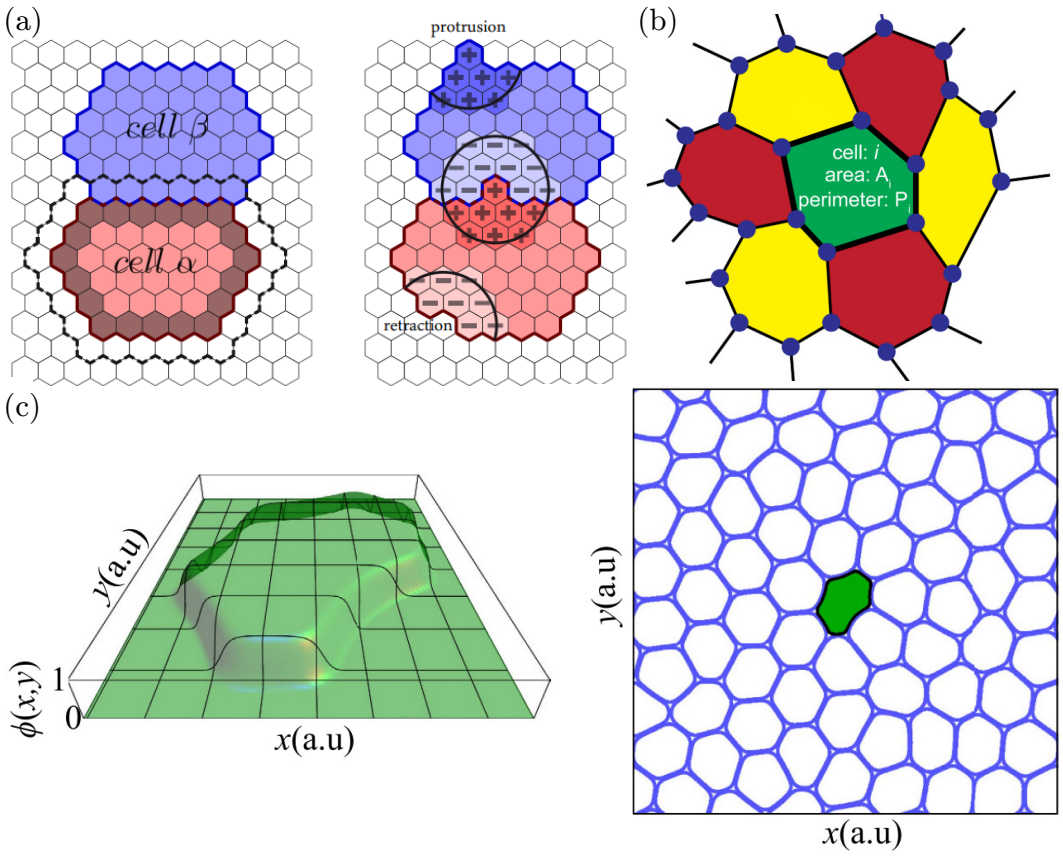

Figure 1.12: Cell-based tissue modelling approaches. (a) A Cellular-potts model showing two cells represented by contiguous blocks of lattice sites. Adapted from [78]. (b) A vertex model showing a tiling of cell whose degrees of freedom are the cell vertices (blue dots).Adapted from [79]. (c) The phase field model, in which cells are each represented by a distinct phase field ϕ_i. Adapted from [80].

A more natural description of confluent tissues can be found in off-lattice models, such as the phase-field model. Initially developed to study interfacial dynamics of single cells [81], phase-field models have also been used hard condensed contexts to study phase boundaries [82]. They have more recently been extended to study collections of cells and confluent tissues. Each cell is represented as a distinct scalar phase field ϕ_i. A free energy is then constructed in terms of ϕ_i and $\nabla\phi_i$ that encodes the integrity of the cell and interactions between cells (Fig. 1.12c). Repulsive forces and cell-cell adhesive forces then arise from gradients in this free energy. Activity can be introduced in a variety of ways. Each cell can experience a polar self-propulsive across its surface akin to ABPs [83, 84]. Additionally, by tying forces to $\nabla\phi_i$, they

can be implemented explicitly at cellular interfaces. In this way active nematic forces have been implemented around the boundary of cells [85, 86]. This captures the active intercellular forces cells can exert on another through cell-cell junctions.

Although phase-field models allow for a clear definition of forces at cellular interfaces, defining the forces cells experience via the scalar field ϕ_i introduces additional parameters and requires the inclusion of Cahn-Hilliard free energy terms to stabilise the interface. This adds unnecessary complexity and, as cells are bound by lipid membranes, this is not the physical mechanism by which cells maintain a stable shape.

Active vertex model

A simpler class of models that have nevertheless provided much insight into confluent tissues are vertex models. Vertex models represent the cell layer as a confluent tiling of polygons, the degrees of freedom being the cell vertices (Fig. 1.12b) [87]. Cell stiffness, cortical tension and cell-cell adhesion are typically encoded via some form of an effective tissue energy function, with gradients in this energy then governing the forces each cell experiences.

While vertex models have their roots in describing the physics of foams, polar self-propulsive forces have recently been included to create active vertex models (AVMs) [88]. By using the cell vertices to define a long-axis for each cell, active nematic forces have also been implemented [89]. This intuitive description of cellular forces has led to AVMs becoming increasingly popular, with variations looking at the effects of active cell-edge tensions [90], cell division and apoptosis [91]. It has been used to study a variety of phenomena from embryo development [92], to epithelial tissue folding [93] and cancer metastasis [94].

Self-propelled Voronoi model

A related class of vertex models are self-propelled Voronoi (SPV) models [95, 79].

These operate under the same principles as AVMs but each cell is defined by a single degree of freedom, a point called its cell 'centre'. A Voronoi tessellation is performed based on the positions of the centres from which the cell vertices found. This halves the number of degrees of freedom in the system compared to AVMs, as there are $2N$ vertices for every N cells, but requires an extra calculation to determine how the movement of the cell vertices translates to movement of the cell centre. Moreover, as the tissue is defined using a Voronoi tessellation, all the cell are by definition convex in shape, meaning this model is only appropriate for studying scenarios where cellular deformation is low. Nevertheless, SPVs have successfully captured several phenomena seen experimentally, from the emergence of wavelike modes in confined epithelia [96] to tissue organisation in corneal epithelia [58].

Coarse-grained

As illuminating as microscopic models are, their complexity often increases rapidly with the number of constituents being modelled. Also, as the length-scale of the system and phenomena being studied becomes orders of magnitude larger then the scale of the constituents and their interactions, the behaviour of individual constituents ceases to be of concern and their average behaviour becomes more appropriate for describing system dynamics. One does not model fluid flow by simulating the dynamics of every molecule in the fluid, instead one solves the hydrodynamic equations of motion (EOM), which are determined by the symmetries of the system at hand.

This is incredibly powerful, as each hydrodynamic model describes a whole class of microscopic models that possess the same symmetries. The Vicsek model, ABPs and AVMs, provided they are dry and their self-propulsion is polar, are all described by the same model in the hydrodynamic limit: the Toner-Tu equations [97, 98]. Similarly, wet passive nematic systems are all described by the Beris-Edwards equations [99]. The inclusion of activity then allows for the inclusion of additional terms [34].

Collectively migrating tissues could therefore be described using the Toner-Tu equations, or the dynamics of a cellular orientation field by the Beris-Edwards equations with additional active terms. However, due to the many non-linearities that arise in these equations, they can be very difficult to analyse. They can be solved by direct numerical simulation, and numerous studies have implemented different approaches, such as finite difference [100] and spectral methods [101], to simulate these hydrodynamic equations under various conditions. This has been done to investigate the dynamics of nematic defects [66] and the dynamics of polar defects during the transition to order [102]. Nonetheless, the non-linearities in these equations can still cause these methods to be slow and cumbersome.

One potential remedy for this problem is to use a mesoscopic approach such as lattice-Boltzmann methods (LBMs). LBMs solve a simplified mesoscale model, a discretised form of the Boltzmann equation, of the system of interest. The underlying principle is that if this simplified system obeys the same symmetries as the system we seek to model, then it must produce the correct behaviour in the hydrodynamic limit as this is determined by the symmetries of the system.

This was the foundation for work done on lattice gas cellular automata models, the predecessor to LBMs, which consist of particles moving and colliding on a lattice. These lattice gas models are able to generate Navier-Stokes like behaviour [103], however these models are still microscopic and the mean behaviour can only be found by averaging over many realisations. LBMs solve this problem by moving a distribution of particles around the lattice, effectively performing the averaging in advance. It has since been shown analytically that LBMs of passive fluids correspond exactly to solving the Navier-Stokes equations in the hydrodynamic limit [104]. Similarly, the same has been done for nematic systems, with an LBM for simulating the nematic field being shown to correspond to the Beris-Edwards equation in the hydrodynamic limit [105]. Of particular pertinence here is the recent development

and application of LBMs to active systems. An LBM developed for dry active matter has been shown to correspond to the Toner-Tu equations in the hydrodynamic limit [106]. This same model has also reproduced several canonical dry active matter emergent phenomena, such as collective motion. Moreover, a variety of phenomena in wet active nematic systems have been studied using a 'hybrid' LBM, where the velocity field is solved using a LBM and the nematic field is solved using finite differences [100]. It has been used to investigate the onset of turbulence in these systems [107, 108] and also the roles of nematic defects as organisational centres in bacterial colonies [34]. Most work using LBMs has focussed on models where cell proliferation and death is ignored, although the hybrid LBM has been used to study the role of cell division in tissue dynamics [109].

One of the main draws of LBMs is their simplicity; solving a simplified minimal model of the system we seek to describe strips away complexity and consequently computational cost. They do, however, have their limitations. A key assumption in their derivation is that the velocities present in the system are much lower than the speed of sound; note that this is not an issue for cellular systems, which typically operate in the overdamped limit.

One of the key challenges in modelling systems using LBMs and hydrodynamic models is ascertaining the correct values for the parameters of the system one is seeking to describe. This is because, when using models derived from the symmetries of the system, any link to the specific microscopic system of interest is lost. One approach recently developed to combat this is the development of machine learning models to infer these parameters from experimental data [110].

1.2.3 Machine learning in active matter

Like in so many scientific fields, machine learning, or 'data-driven', approaches are being increasingly used in active matter for problems where theoretical techniques either do not yet exist or are inadequate [111]. Machine learning is an incredibly broad field of study in which, often large amounts of, data are used to fit, or 'train', a high dimensional model such that when new data is input into the trained model it can make a prediction or decision without being explicitly programmed to do so. Most of the approaches used to date in active matter are classed as 'supervised' learning methods.

In supervised methods, the model is trained by being given a set of inputs along with the desired corresponding outputs [112]. Its parameters are then fitted such that they provide the best mapping between them. This is in contrast to unsupervised methods, where the training inputs are not labelled with a desired output. The model is then trained to minimise some other cost function, as opposed to the difference between the predicted output and the desired output, meaning the number of outputs and the values they can take are not predetermined. In both these methods, model parameters are usually fitted using some form of stochastic gradient-based optimisation method, where the parameters are initialised and gradually adjusted based on approximating the gradient of the cost function with respect to the parameters [113].

Supervised models can be broadly split into two categories: regression models and classification models [112]. In classification models, each input is labelled to correspond to a single output, or 'class', with the model trained to assign the correct class for a given input. In practise this means that all possible outputs are zero except the output corresponding to the predicted class of the input, which would be one. In regression models, however, the model is trained to predict some numerical value or values, so outputs are not binary and, if there are multiple, can all take

different values.

It is regression models that are used to determine parameters in hydrodynamic models, with the most common used thus far are linear regression methods. In these methods, the measured hydrodynamic variables are used as inputs. From these fields, all derivatives, and combinations of variables and derivatives, appearing in the equations can be calculated at each point in the field. A linear fit is then performed on the coefficients to the hydrodynamic equations such that the equation is satisfied at each point in the field. This method even allows for the formulation of hydrodynamic equations, as generalised equations can be postulated, containing all terms allowed by the symmetries of the system being studied, and terms discarded if their accompanying parameter is negligibly small, leaving a minimal set of terms that adequately match the data. This approach has been successfully implemented on microtubule active nematic systems [114, 115] and systems of polar particles [116].

Another method for determining hydrodynamic coefficients is to use a neural network. Based on biological neural networks in the brain, artificial neural networks are collections of nodes, or 'neurons', that receives either input data or signals from other neurons and, based on this information, transmits a signal to neurons it is connected to [113]. Typically these neurons are arranged into distinct layers which are often 'fully-connected', with each neuron in one layer providing an input to every neuron in the subsequent layer (Fig. 1.13a). Each neuron's output is some function of the weighted sum of its input, and so can be thought of as combining information from different parts of the input data (Fig. 1.13b). The parameters that are fitted during training are then the weights of the connections between each neuron. The weights determines the strength of the signal through each neuron and by adjusting them one can identify combinations and correlations in the input data that are important for predicting the output accurately. However, as opposed to linear regression

where the parameters being trained are the coefficients of the equations themselves, and the cost function is the error in some postulated equation of motion, in neural networks the parameters are fitted to predict these coefficients and the error is the difference between this prediction and the actual coefficients. As such, data where the actual hydrodynamic coefficients are known is needed. This has been achieved for an active nematic system by training a neural network on data from a simulated nematohydrodynamic model, where the parameters are known, before testing it on experimental data for a microtubule system [110].

In this study, the first layers in the neural network were convolutional layers. Convolutional layers take advantage of spatial structure in the input by passing a 2D array of neurons known as a feature detector, over the input data to test whether a feature or structure is present in the data at each point (Fig. 1.13b). Multiple feature detectors identifying different structures and patterns are used simultaneously, with the output signal being how strongly each feature is detected at each point in the field. The parameters that are then trained are the weights of each neuron in the feature detector, such that the model is trained to detect pertinent features [113]. Convolutional layers are more effective than fully-connected layers when the input data for a given problem is an image or 2D field, as they preserve the 2D structure of the image. Fully-connected layers flatten the image into one dimension when feeding the input data into the first layer of the network.

Due to this, convolutional neural networks (CNNs) are widely used in classification tasks where objects need to be detected in an image. Neural networks are commonly used in classification tasks and can be very useful in classifying phenomena and behaviour in active systems. They have been used to identify distinct phases in a system of polar particles [117] and detect topological defects in nematic systems [118, 119]. As previously discussed, correctly classifying behaviour in biological systems can be a challenge in itself and a prerequisite for understanding the mecha-

nisms driving such behaviour. Machine learning and neural networks therefore offer a promising avenue for assisting in this regard, where theory based methods are currently lacking.

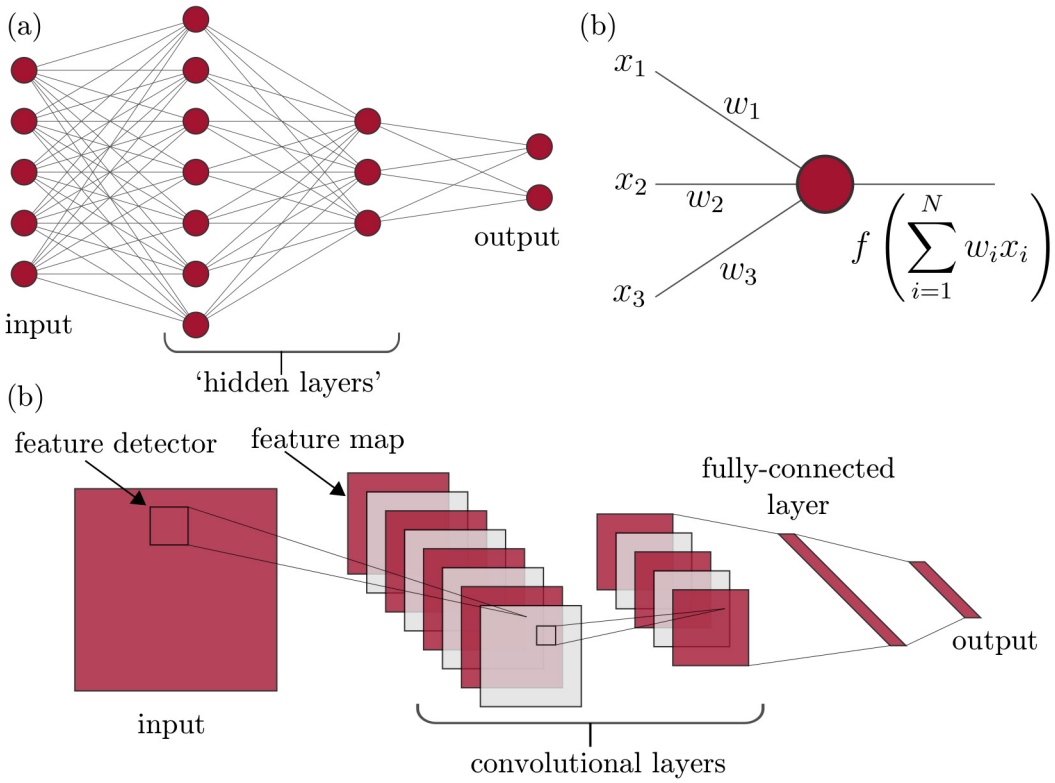

Figure 1.13: Schematics of neural network architectures. (a) A fully-connected feed forward network. Input data is fed into intermediate, or 'hidden', layers who in turn transmit signals to subsequent layers or the output layer. (b) Each input x_i to a neuron is weighted by w_i, the parameter that is fitted during training, such that each neuron produces an output signal that is a function of the weighted sum of its N inputs. (c) A convolutional neural network. Feature detectors, scan the 2D input data to create a map of the degree to which a given pattern is detected at each point in the input. Further layers of feature detectors can be scanned across these maps the search for higher order correlations in the input data. These layers are typically succeeded by a fully connected layer to collate the information into form that can be fed into the output layer.

1.3 Overview and scope

Thus far we have discussed some of the behaviours exhibited by confluent tissues, their role in important biological processes and why the most effective way of understanding them can often be from the forces generated, and interactions that arise, at the cellular level. We have also outlined some of these forces and interactions, where the link between them and the emergent behaviour can sometimes be clear but is often uncertain. In the following chapters, we will develop tools and concepts from active matter, introduced above, to gain insight into the emergence of different tissue scale phenomena.

In Chapter 2, we investigate the emergence of extensile nematic behaviour in confluent tissues. As discussed previously, the actomyosin machinery within cells means the active forces they generate are contractile, meaning one would reasonably assume that behaviour at the tissue level is also contractile. However, some tissues exhibit extensile collective behaviour, evidenced by the motion of $+1/2$ defects in the tissue. To investigate how extensile behaviour can emerge from a collection of contractile constituents, we construct a linearised hydrodynamic model of a confluent tissue on a substrate which describes tissue velocity and nematic fields in the limit of small fluctuations. By calculating correlations between the velocity field and the nematic field, we show that the polar traction forces cells generate to self-propel manifest as extensile behaviour in the nematic field. This can drive extensile nematic behaviour in systems with contractile constituent forces. We then demonstrate an example of this result by examining the motion of nematic defects detected in an AVM whose only active forces are polar. As the active forces are solely polar, from our analytical theory we expect this model to exhibit extensile motion, which is exactly what we find.

In seeking to examine the motion of defects in an AVM in Chapter 2, one of the

key challenges was detecting nematic defects when they appear in the tissue. One cannot begin to understand or study these phenomena and the biological processes they mediate if they cannot even be reliably identified. Current methods break down and are inefficient in systems of cells where the long-axis is less well-defined, as as often the case in confluent tissues such as epithelial layers. This is evidenced through the vast amounts of data required to obtain the extensile velocity field around the defects detected in our AVM. In Chapter 3 we address this deficiency by developing a machine learning model to detect defects in confluent tissues, designed such that it is easy to use and suitable for experimental data. We train it using data from our AVM and show that it outperforms current defect detection techniques. We demonstrate this improved performance with improved capturing of the velocity field around $+1/2$ defects using a limited amount of data. This highlights that our method has the potential to improve experimental outcomes where the amount of available data can be limited.

In Chapter 4, we study a different tissue scale behaviour, the dynamics of a growing tissue boundary. We examine the dynamics and stability of the interface of a growing tissue, focusing on the role of cell proliferation in the dynamics of the interface. To do this we develop a novel LBM that incorporates friction with the substrate, cell proliferation and, crucially, a sharp, growing front. We find that, for two different growth regimes at small system sizes, the growth and dynamics of the interfaces are characterised by fluctuations in the interface width that scale in agreement with the Kardar-Parisi-Zhang (KPZ) universality class. However, we find that, for sufficiently large system sizes, the width of the interface becomes unstable and a system spanning instability emerges. By constructing a minimal analytical model for the dynamics of the interface, we show that this instability emerges due to a coupling between the number of constituents actively proliferating and the position of the interface.

In Chapter 5, we summarise our findings, their implications, the limitations of our work, and future directions for each of the studies.

Chapter 2

Emergent active nematic collective behaviour

2.1 Introduction

Collective nematic behaviour in planar confluent epithelial tissues represent a prime example of emergent behaviour at the macroscopic level being very different from what one would expect from the microscopic picture. While a single motile epithelial cell on a substrate can exhibit polar dynamics [78, 18] and generate contractile nematic stress when its cell shape is elongated [120], a confluent monolayer of these cells can instead act like an extensile nematic [29]. Intriguingly, this disconnect between the cellular and tissue dynamics is robust and present no matter whether the tissue is in a liquid or solid state. The cause of this discrepancy remains poorly understood in both cases. Resolving the seemingly contradictory behaviour at the single-cell versus the tissue level is not only important to active matter physics, but is also crucial to a number of fundamental biological processes. As discussed in Section 1.1.3, in confluent cell layers, extensile nematic defects have been shown to mediate cell extrusions in epithelial monolayers [29] and control the collective dynamics

of neural progenitor cell cultures [30]. In collectives of micro-organisms, they are responsible for initiating layer formation in *Myxococcus xanthus* colonies [32], mediating the morphologies of growing *E. coli* colonies [34], controlling morphogenesis in *Hydra* [31] and increasing collective migration velocities of *Pseudomonas aeruginosa* [33].

Due to the presence of nematic defects, these biological systems are increasingly being characterised using active nematic theories [121, 122, 123]. As active nematic systems are typically characterised by elongated constituents possessing apolar motility [124], where it is well established that activity can induce local nematic order [125, 126, 127], it is not surprising that previous studies focused on describing these systems as active nematics. For example, in *Myxococcus xanthus* colonies, individual bacteria are rod shaped and display periodic reversals of velocity direction [128]. Other biological constituents that exhibit collective nematic behaviour usually possess at least one of these two features, such as the spindle shape of fibroblasts or the active forces involved in cell division being inherently dipolar [21, 109, 56]. However, epithelial cells are not rod-shaped and display polar dynamics [78, 18], calling into question whether active nematic theories capture the fundamental physics of epithelial monolayers.

Recent studies have tried to resolve the discrepancy between cell-level and tissue-level dynamics in epithelial tissues [85, 129, 86], with one study notably linking polar activity to extensile active nematic behaviour [129]. However, these studies either directly incorporate *ad-hoc* extensile nematic terms into the equations of motion (EOM), either in the deterministic part [85] or the fluctuation part [129]. *Ad-hoc* anisotropic noise terms with no biological motivation have also been added to nematic models to achieve the extensile behaviour [86]. Doing so begs the following question: Are we missing key microscopic, cell-level ingredients to justify these terms?

In this chapter, we refute this need by showing, analytically and by simulation, that polar fluctuations (due to cell-substrate interactions) generically lead to extensile nematic behaviour in a confluent tissue, in *both* liquid and solid states. Our conclusion applies universally in the small fluctuation limits when active contractile nematic stresses are absent in the system. When contractile stresses are switched on at the cellular level (due to cellular contractility and cell-cell interactions [130]), the nematic nature of the confluent tissue can be either extensile or contractile depending on, e.g., the relative strengths of the polar fluctuations and the fluctuations of the active nematic stresses.

We will first analyse a generic set of linearised EOM describing the velocity and nematic fields of confluent cell tissues in both solid and liquid states. We then illustrate our findings by simulating liquid and solid confluent tissues using an AVM and determine their collective behaviour by examining the dynamics of nematic defects in the system.

2.2 Analytical hydrodynamic modelling

2.2.1 Incompressible fluid case

We first consider a hydrodynamic model of a 2D confluent cell tissue in the liquid state. Consistent with previous studies, we will treat confluent tissues with polar fluctuations as an incompressible active fluid on a frictional substrate [97, 98, 60, 131], in which the polar fluctuations originate from cell-substrate interactions as the cells generate active traction forces; we ignore thermal fluctuations as they are negligible in cellular and tissue dynamics. To capture the coarse-grained cell shape anisotropy, we use the nematic tensor field $\mathbf{Q} = S(2\hat{\mathbf{n}}\hat{\mathbf{n}} - 1)$, where S is the scalar nematic order parameter and $\hat{\mathbf{n}}$ is the local coarsed-grained unit director that

corresponds to the local average orientation of cell elongation. The scalar order parameter S takes a value of 1 if cells are perfectly aligned locally and zero if they are in an isotropic state.

The equations of motion are the active nemato-hydrodynamic equations of motion for a dry system, which are

$$\partial_t \mathbf{v} + \mathbf{v} \cdot \boldsymbol{\nabla} \mathbf{v} = \mu \nabla^2 \mathbf{v} - \nabla P - \Gamma \mathbf{v} + \alpha \nabla \cdot \mathbf{Q} + \boldsymbol{\xi} \tag{2.1a}$$

$$\partial_t \mathbf{Q} + \mathbf{v} \cdot \nabla \mathbf{Q} = \boldsymbol{\Omega} + D \nabla^2 \mathbf{Q} - \eta \mathbf{Q} \ , \tag{2.1b}$$

where P is our tissue pressure. In the language of optimisation, the "pressure" P in Eq. (2.5a) acts as a Lagrange multiplier that enforces the incompressibility condition $\nabla \cdot \mathbf{v} = 0$. In other words, it takes the value that minimises the free energy $F = \frac{1}{2} \int_x \mu |\nabla \mathbf{v}|^2$ subject to the constraint $\nabla \cdot \mathbf{v} = 0$.

Our tissue viscosity is μ, Γ the effective friction with the substrate and α the nematic activity. The active nematic term $\alpha \nabla \cdot \mathbf{Q}$ stems from the active stress $\alpha \mathbf{Q}$. As our system is active, force densities need not arise from a free-energy functional and the active stress is a simple, apolar means of representing the coarse-grained dipolar force fields generated by cells' cytoskeleton and transmitted via cell-cell junctions [132]. Taking $\alpha > 0$ encodes the active contractility exhibited by individual cells. The polar fluctuations $\boldsymbol{\xi}$, originating from cell-substrate interactions such as transient lamellipodia activity [130, 18], are represented by a Gaussian white noise with

$$\langle \xi_i(t, \mathbf{r}) \rangle = 0 \ , \ \langle \xi_i(t, \mathbf{r}) \xi_j(t', \mathbf{r}') \rangle = 2\Delta \delta_{ij} \delta(t - t') \delta^2(\mathbf{r} - \mathbf{r}') \ , \tag{2.2}$$

where Δ is the strength of the fluctuations. Indeed, while the cells' polar fluctuations typically display some persistency, this length and time-scale of this persistency is lower than hydrodynamic scales. This means that, in the hydrodynamic limit (i.e. at long enough time and length-scales), this persistency is irrelevant and these

fluctuations can be described as δ-correlated noise terms as in Eq. (2.2). This is akin to systems of self-propelled particles being described by the Toner-Tu equations in the hydrodynamic limit [53, 97, 98].

In our EOM for $\mathbf{Q}$, $\mathbf{\Omega}$ is the corotational derivative, capturing the response of the nematic field to gradients in the flow, in addition to the advective term on the LHS. It is given by

$$\begin{aligned}\Omega_{ij} = (2\lambda S_{ik} + \omega_{ik})\left(Q_{kj} + \frac{\delta_{kj}}{2}\right) \\ + \left(Q_{ik} + \frac{\delta_{ik}}{2}\right)(2\lambda S_{kj} - \omega_{kj}) - 2\lambda\left(Q_{ij} + \frac{\delta_{ij}}{2}\right)(Q_{kl}\partial_k v_l)\ ,\end{aligned} \tag{2.2}$$

where $S_{ij} = (\partial_j v_i + \partial_i v_j)/2$ is the strain rate tensor, $\omega_{ij} = (\partial_i v_j - \partial_j v_i)/2$ is the vorticity tensor and λ is our flow alignment parameter. The other two terms on the RHS of our EOM for $\mathbf{Q}$ describe the relaxational dynamics of of system. The are governed by the de Gennes-Ginzburg-Landau free energy $F = \frac{1}{2}\int_x (aTr[\mathbf{Q}]^2 + K(\nabla\mathbf{Q})^2)$, where K is the nematic stiffness (in the one-elastic constant approximation) [133, 129]. As, in the absence of activity, our system will relax to an isotropic state ($S = 0$), $a > 0$ and we neglect stabilising higher order terms in $\mathbf{Q}$. The two terms in our EOM then come from the system seeking to relax to a minimum in this free energy

$$-\frac{1}{\gamma}\frac{\delta F}{\delta \mathbf{Q}} = -\eta\mathbf{Q} + D\nabla^2\mathbf{Q}\ , \tag{2.4}$$

where γ describes the rotational viscosity of the material, $D = K/\gamma$ is the diffusivity parameter and $\eta = a/\gamma$ can be thought of as an inverse relaxation time.

Motivated by *in vitro* experimental studies on epithelial tissues, we focus on the regime without long-range order in the velocity field $\mathbf{v}$ [131] or quasi-long-range order in the nematic field $\mathbf{Q}$ [134, 135, 136], and away from the order-disorder critical region [137]. While we do not expect the system to develop any hydrodynamic soft modes in this regime, it is still of interest to use the hydrodynamic equations to

study the system at length-scales beyond the microscopic (cellular) length-scale. In the small fluctuations regime, the magnitudes of both $\mathbf{v}$ and $\mathbf{Q}$ are small and thus the linearised EOM are expected to apply universally; these are of the form:

$$\partial_t \mathbf{v} = \mu \nabla^2 \mathbf{v} - \nabla P - \Gamma \mathbf{v} + \alpha \nabla \cdot \mathbf{Q} + \boldsymbol{\xi} \tag{2.5a}$$

$$\partial_t \mathbf{Q} = \lambda \left[\boldsymbol{\nabla} \mathbf{v} + (\boldsymbol{\nabla} \mathbf{v})^{\mathsf{T}} \right] + D \nabla^2 \mathbf{Q} - \eta \mathbf{Q} \ . \tag{2.5b}$$

We will focus first on the case of passive nematics, without any contractility ($\alpha = 0$ in Eq. (2.5a)). In the highly damped limit (large Γ and η), we can set both temporal derivatives in Eq. (2.5) to zero. To ascertain the extensile or contractile nature of the nematic field, we calculate the equal-time, equal-position correlation $\langle \mathbf{v} \cdot (\nabla \cdot \mathbf{Q}) \rangle$. The motivation behind doing so is that an active nematic material is usually characterised as extensile or contractile by the sign of the coefficient α in front of the active nematic term $\alpha \nabla \cdot \mathbf{Q}$ when present [53, 138, 139]. Focusing on Eq. (2.5a) and ignoring all spatial and temporal variations, it is clear that the sign of α is the same as that of the correlation $\langle \mathbf{v} \cdot (\nabla \cdot \mathbf{Q}) \rangle$. Therefore, even if $\alpha = 0$, calculating such a correlation, or just determining whether it is positive or negative, enables us to ascertain effectively the extensile or contractile nature of the nematic field under the system's dynamics.

We can express $\langle \mathbf{v} \cdot (\nabla \cdot \mathbf{Q}) \rangle$ as inverse Fourier transforms (where the Fourier transform is defined as: $\tilde{\mathbf{v}}(\mathbf{k}) \equiv \mathcal{F}[\mathbf{v}(\mathbf{r})] = (2\pi)^{-1} \int \mathrm{d}^2\mathbf{r}\, \mathbf{v}(\mathbf{r}) e^{-\mathrm{i}\mathbf{k}\cdot\mathbf{r}}$) by

$$\langle \mathbf{v} \cdot (\nabla \cdot \mathbf{Q}) \rangle = \left\langle \mathcal{F}^{-1}[\tilde{\mathbf{v}}(\mathbf{k}')] \cdot \mathcal{F}^{-1}[\mathrm{i}\mathbf{k} \cdot \tilde{\mathbf{Q}}(\mathbf{k})] \right\rangle \tag{2.6a}$$

$$= \left\langle \int \frac{\mathrm{d}^2\mathbf{k}\, \mathrm{d}^2\mathbf{k}'}{(2\pi)^2} \tilde{v}_i(\mathbf{k}') (\mathrm{i} k_j \tilde{Q}_{ij}(\mathbf{k})) e^{\mathrm{i}(\mathbf{k}+\mathbf{k}')\cdot\mathbf{r}} \right\rangle \ . \tag{2.6b}$$

We now seek to write our velocity and nematic field in terms of our stochastic fluctuations, which we can then average over to calculate our correlation. In the

large damping limit with $\alpha = 0$, Eq. (2.5a) reads

$$\Gamma \mathbf{v} = -\nabla P + \mu \nabla^2 \mathbf{v} + \boldsymbol{\xi} \ . \tag{2.7}$$

Taking the divergence of Eq. (2.7) and applying the incompressibility condition ($\nabla \cdot \mathbf{v} = 0$) gives a Poisson equation in the pressure

$$\nabla^2 P = \nabla \cdot \boldsymbol{\xi} \ . \tag{2.8}$$

Assuming our pressure and fluctuations decay to zero at infinity, we can thus eliminate the pressure from our velocity equation to obtain

$$\Gamma \mathbf{v} - \mu \nabla^2 \mathbf{v} = \mathcal{P} \boldsymbol{\xi} \ , \tag{2.9}$$

where we have introduced the incompressibility projection operator $\mathcal{P}$, $\mathcal{P}_{ij} = \delta_{ij} - \hat{k}_i \hat{k}_j$ in Fourier transformed space. Fourier transforming the whole expression above and using Einstein's summation convention, we can write our velocity field in terms of our stochastic fluctuations

$$(\Gamma + \mu k^2) \tilde{v}_i(\mathbf{k}) = \mathcal{P}_{ij} \tilde{\xi}_j(\mathbf{k}) \ . \tag{2.10}$$

For the nematic field, taking the divergence of Eq. (2.5b) and using the incompressibility condition, we obtain in index notation

$$(\eta - D\partial_{kk}) \partial_j Q_{ij} = \lambda \partial_{jj} v_i \ , \tag{2.11}$$

which in Fourier space leads to

$$\mathrm{i} k_j \tilde{Q}_{ij}(\mathbf{k}) = -\frac{\lambda k^2 \tilde{v}_i(\mathbf{k})}{\eta + Dk^2} = -\frac{\lambda k^2}{\eta + Dk^2} \frac{\mathcal{P}_{ij} \tilde{\xi}_j(\mathbf{k})}{\Gamma + \mu k^2} \ , \tag{2.12}$$

as required. Substituting Eq. (2.10) and Eq. (2.12) into Eq. (2.6b) gives

$$\langle \mathbf{v} \cdot (\nabla \cdot \mathbf{Q}) \rangle = \left\langle \int \frac{\mathrm{d}^2\mathbf{k}\,\mathrm{d}^2\mathbf{k}'}{(2\pi)^2} \frac{\mathcal{P}_{ij}\tilde{\xi}_j(\mathbf{k}')}{\mu k'^2 + \Gamma} \left(-\frac{\lambda k^2}{\eta + Dk^2} \frac{\mathcal{P}_{il}\tilde{\xi}_l(\mathbf{k})}{\Gamma + \mu k^2} \right) e^{i(\mathbf{k}+\mathbf{k}')\cdot\mathbf{r}} \right\rangle \tag{2.13}$$

$$= -\lambda \int \frac{\mathrm{d}^2\mathbf{k}\,\mathrm{d}^2\mathbf{k}'}{(2\pi)^2} e^{\mathrm{i}(\mathbf{k}+\mathbf{k}')\cdot\mathbf{r}} \frac{k^2 \left\langle (\delta_{ij} - \hat{k}'_i\hat{k}'_j)\tilde{\xi}_j(\mathbf{k}')(\delta_{il} - \hat{k}_i\hat{k}_l)\tilde{\xi}_l(\mathbf{k}) \right\rangle}{(\mu k'^2 + \Gamma)(\mu k^2 + \Gamma)(\eta + Dk^2)} \,. \tag{2.14}$$

When averaging over the noise the incompressibility projection operator drops out to give as a final result

$$\langle \mathbf{v} \cdot (\nabla \cdot \mathbf{Q}) \rangle = -2\lambda\Delta \int \frac{\mathrm{d}^2\mathbf{k}}{(2\pi)^2} \frac{k^2}{(\eta + Dk^2)(\Gamma + \mu k^2)^2} \,. \tag{2.15}$$

The integral above is always positive (in fact, it equals $\frac{D\Gamma+\mu\eta[\log(\mu\eta/(D\Gamma))-1]}{4\pi\mu(D\Gamma-\mu\eta)^2}$ when integrating over all wavelength $\mathbf{k}$). Therefore, the correlation depends only on the sign of λ. Specifically, the nematic field is statistically extensile if $\lambda > 0$, and contractile if $\lambda < 0$. In the case of confluent cell tissues, it is clear that a positive velocity gradient will cause a cell to stretch in the direction of that gradient. Hence, λ is positive and thus statistically, the velocity field is negatively correlated with the divergence of the nematic field. In other words, in the highly damped limit, a polar fluctuation in confluent cell tissues will generically lead to the appearance of active extensile nematics.

However, active contractile nematic behaviour in cell tissues has also been observed experimentally, e.g. in fibroblasts cells [28, 20]. In the context of active nematics, one can recover this behaviour by setting $\alpha > 0$ in Eq. (2.5a). Additionally, since the nematic field $\mathbf{Q}$ can now generate active stresses, fluctuations in the EOM of $\mathbf{Q}$ are also generically present. Specifically, one needs to include a Gaussian noise term

$\boldsymbol{\Theta}$ on the R.H.S. of Eq. (2.5b), with statistics given by

$$\langle \Theta ij(t, \mathbf{r}) \rangle = 0 \ , \tag{2.16a}$$

$$\langle \Theta ij(t, \mathbf{r}) \Theta kl(t, \mathbf{r}') \rangle = 2\Delta_Q \delta(t - t') \delta^2(\mathbf{r} - \mathbf{r}') \epsilon_{ijkl} \tag{2.16b}$$

where, for symmetry reasons,

$$\epsilon_{ijkl} = \frac{1}{2} \left(\delta_{ik}\delta_{jl} + \delta_{il}\delta_{jk} - \delta_{ij}\delta_{kl} \right) \ . \tag{2.17}$$

We now repeat the analysis with the terms $\alpha \nabla \cdot \mathbf{Q}$ and $\boldsymbol{\Theta}$ included Eq. (2.5a) and Eq. (2.5b), respectively, assuming no correlation between $\boldsymbol{\Theta}$ and $\boldsymbol{\xi}$. In the highly damped limit, our governing equations in the linear regime are thus

$$0 = \mu \nabla^2 \mathbf{v} - \nabla P + \alpha \nabla \cdot \mathbf{Q} - \Gamma \mathbf{v} + \boldsymbol{\xi} \tag{2.18a}$$

$$0 = \lambda \left[\boldsymbol{\nabla} \mathbf{v} + (\boldsymbol{\nabla} \mathbf{v})^{\mathsf{T}} \right] + D \nabla^2 \mathbf{Q} - \eta \mathbf{Q} + \boldsymbol{\Theta} \ . \tag{2.18b}$$

In Fourier transformed space, the above two equations become

$$(\mu k^2 + \Gamma) \tilde{v}_i = \mathcal{P}_{ij} \left[\mathrm{i} \alpha k_k \tilde{Q}_{jk} + \tilde{\xi}_j \right] \tag{2.19a}$$

$$(D k^2 + \eta) \tilde{Q}_{ij} = \mathrm{i} \lambda (k_i \tilde{v}_j + k_j \tilde{v}_i) + \tilde{\Theta}_{ij} \ , \tag{2.19b}$$

where once again $\mathcal{P}_{ij}(\mathbf{k}) = \delta_{ij} - \hat{k}_i \hat{k}_j$ and is there to enforce the incompressibility condition. Using Eq. (2.19b) to eliminate $\tilde{\mathbf{Q}}$ in Eq. (2.19a), we have

$$\left[\mu k^2 + \Gamma + \frac{\lambda \alpha k^2}{D k^2 + \eta} \right] \tilde{v}_i = \mathcal{P}_{ij} \left[\frac{\mathrm{i} \alpha k_k \tilde{\Theta}_{jk}}{D k^2 + \eta} + \tilde{\xi}_j \right] \ . \tag{2.20}$$

We now consider the equal-time correlation $\langle \mathbf{v} \cdot (\nabla \cdot \mathbf{Q}) \rangle$, which can be expressed as

$$\begin{aligned}
\langle \mathbf{v} \cdot (\nabla \cdot \mathbf{Q}) \rangle &= \left\langle \mathcal{F}^{-1}[\tilde{\mathbf{v}}(\mathbf{k}')] \cdot \mathcal{F}^{-1}[\mathrm{i}\mathbf{k} \cdot \tilde{\mathbf{Q}}(\mathbf{k})] \right\rangle \\
&= \left\langle \int \frac{\mathrm{d}^2\mathbf{k}}{2\pi} \frac{\mathrm{d}^2\mathbf{k}'}{2\pi} \tilde{v}_i(\mathbf{k}')[\mathrm{i}k_j \tilde{Q}_{ij}(\mathbf{k})] e^{\mathrm{i}(\mathbf{k}+\mathbf{k}')\cdot\mathbf{r}} \right\rangle \\
&= \int \frac{\mathrm{d}^2\mathbf{k}\mathrm{d}^2\mathbf{k}'}{(2\pi)^2} \frac{e^{\mathrm{i}(\mathbf{k}+\mathbf{k}')\cdot\mathbf{r}}}{Dk^2+\eta} \left[-\lambda k^2 \langle \tilde{v}_i(\mathbf{k}') \tilde{v}_i(\mathbf{k}) \rangle + \mathrm{i}k_j \langle \tilde{v}_i(\mathbf{k}') \tilde{\Theta}_{ij}(\mathbf{k}) \rangle \right] \\
&= \int \frac{\mathrm{d}^2\mathbf{k}}{(2\pi)^2(Dk^2+\eta)} \Bigg\{ -2\lambda\Delta k^2 G(k)^2 \\
&\quad + \alpha\Delta_Q k^2 \left[\frac{G(k)}{Dk^2+\eta} - \frac{\alpha\lambda k^2 G(k)^2}{(Dk^2+\eta)^2} \right] \Bigg\},
\end{aligned} \tag{2.22}$$

where $G(k) \equiv \left[\mu k^2 + \Gamma + \frac{\lambda\alpha k^2}{Dk^2+\eta} \right]^{-1}$.

For passive nematics ($\alpha = 0$), the above expression corresponds to Eq. (2.15). The second and third terms are the new terms due to the nematic activity. Denoting the term in the square brackets as

$$I(k) = \frac{G(k)}{Dk^2+\eta} - \frac{\alpha\lambda k^2 G(k)^2}{(Dk^2+\eta)^2}, \tag{2.22}$$

one finds that $\lim_{k\to 0} I(k) = (\Gamma\eta)^{-1}$ and $\lim_{k\to\infty} I(k) = 0$. Further, for contractile nematics, $\alpha > 0$, given that all parameters Γ, μ, η, λ and D are also positive, one can show that $I(k)$ is a monotonically decreasing function by checking that $I'(k) < 0$. We thus conclude that the sign of the term in the square brackets is always positive. Hence, the system can transition from exhibiting extensile nematic behaviour to contractile nematic behaviour when the terms in the square bracket dominate over the first one. As the contractile and extensile terms are proportional to $\alpha\triangle_Q$ and $\lambda\triangle$ respectively, this shows that the extensile-to-contractile transition occurs when $\alpha\triangle_Q \gg \lambda\triangle$.

To better estimate when the transition occurs, we can focus on the high damping

limit ($\Gamma, \eta \gg 1$) and re-write the above integral as

$$\int_0^\Lambda \frac{\mathrm{d}k}{2\pi} \left[\frac{\alpha\Gamma\triangle_Q k^3 + (2D\Delta\lambda - \alpha\triangle_Q\mu)k^5}{\Gamma^2\eta^2} - \frac{2\Delta\lambda k^3}{\Gamma^2\eta} + \mathcal{O}\left(\frac{1}{\eta^3}, \frac{1}{\Gamma^3}\right) \right] , \tag{2.23}$$

where we have integrated out the angular direction and imposed an ultra-violet cutoff Λ. Integrating the integral, we find that, in the limits of large Γ, η and Λ, the extensile-to-contractile transition occurs when

$$\frac{\alpha\Delta_Q}{\lambda\Delta} > \frac{2D}{\mu} . \tag{2.24}$$

We note here that our results so far are qualitatively and quantitatively different from a recent work linking polar forces to extensile behaviour [129] in the following ways: (1) both the active stress term ($\propto \alpha$) and fluctuations in $\mathbf{Q}$ are crucial for the extensile-contractile transition in our work (since it is the product $\alpha\Delta_Q$ that appears in the correlation Eq. (2.21)), (2) we do not assume that the nematic field influences the polar fluctuations, and (3) nonlinear advective coupling is not needed in our treatment. Indeed, while nonlinear effects may be crucial in the high fluctuation limit, it remains unclear how to gauge the importance of a particular nonlinear term in relation to (many) other nonlinear terms that are intrinsically present in the EOM. In the present theory, we focus exclusively on the small fluctuation limit.

2.2.2 Compressible fluid case

To underline the generality of our result, we now look at a tissue away from the incompressible limit, in the case without active contractility. Introducing compressibility to our system means we must now include a continuity equation for our density field ρ. Our initial EOM are thus

$$\partial_t \rho + \mathbf{v} \cdot \boldsymbol{\nabla} \rho = -\rho(\boldsymbol{\nabla} \cdot \mathbf{v}) \tag{2.25a}$$

$$\partial_t \mathbf{v} + \mathbf{v} \cdot \boldsymbol{\nabla} \mathbf{v} = \mu_1 \nabla^2 \mathbf{v} + \mu_2 \boldsymbol{\nabla}(\boldsymbol{\nabla} \cdot \mathbf{v}) - c^2 \boldsymbol{\nabla} \rho - \Gamma \mathbf{v} + \boldsymbol{\xi} \tag{2.25b}$$

$$\partial_t \mathbf{Q} + \mathbf{v} \cdot \boldsymbol{\nabla} \mathbf{Q} = \boldsymbol{\Omega} + D \nabla^2 \mathbf{Q} - \eta \mathbf{Q} \ , \tag{2.25c}$$

where we have used an equation of state for the pressure $P = c^2 \rho$ and now have an additional contribution from viscous stresses in Eq. (2.26) due to relaxing the incompressibility condition. As we are concerned with the small fluctuation limit, we linearise the continuity equation around a mean density ρ_0. Our linearised EOM now read

$$\partial_t \rho = -\rho_0(\boldsymbol{\nabla} \cdot \mathbf{v}) \tag{2.26a}$$

$$\partial_t \mathbf{v} = \mu_1 \nabla^2 \mathbf{v} + \mu_2 \boldsymbol{\nabla}(\boldsymbol{\nabla} \cdot \mathbf{v}) - c^2 \boldsymbol{\nabla} \rho - \Gamma \mathbf{v} + \boldsymbol{\xi} \tag{2.26b}$$

$$\partial_t \mathbf{Q} = \lambda(\boldsymbol{\nabla} \mathbf{v} + \boldsymbol{\nabla} \mathbf{v}^T) + D \nabla^2 \mathbf{Q} - \eta \mathbf{Q} \ . \tag{2.26c}$$

In Fourier transformed space, the density is given by

$$\tilde{\rho} = \frac{\rho_0 \mathbf{k} \cdot \tilde{\mathbf{v}}}{\omega} \ , \tag{2.27}$$

which can be substituted into the Fourier transformed equation for the velocity field to give

$$[\mathrm{i}\omega - \mu_1 k^2 - \Gamma]\tilde{\mathbf{v}} - \left[\mu_2 k^2 + \mathrm{i} c^2 \frac{\rho_0}{\omega}\right] \mathbf{k}(\mathbf{k} \cdot \tilde{\mathbf{v}}) + \tilde{\boldsymbol{\xi}} = 0 \ . \tag{2.28}$$

By separating $\tilde{\mathbf{v}}$ into its longtudinal and transverse components $\tilde{\mathbf{v}} = \tilde{v}^L(\mathbf{k})\hat{\mathbf{k}} + \tilde{\mathbf{v}}^T(\mathbf{k})$, where $\mathbf{k} \cdot \tilde{\mathbf{v}}^T = 0$ by definition, and substituting this into Eq. (2.28) we can obtain

expressions for each of these components in terms of the polar fluctuations

$$\tilde{v}^L = \frac{\tilde{\xi}^L}{\mu_L k^2 + \Gamma + \mathrm{i}\left(c^2 k^2 \frac{\rho_0}{\omega} - \omega\right)} \tag{2.29a}$$

$$\tilde{\mathbf{v}}^T = \frac{\tilde{\boldsymbol{\xi}}^T}{\mu_1 k^2 - \mathrm{i}\omega} \ , \tag{2.29b}$$

where $\mu_L = \mu_1 + \mu_2$. Now writing the equation for the nematic field in Fourier space and taking the divergence we have

$$\mathrm{i}\mathbf{k}\cdot\tilde{\mathbf{Q}} = \frac{-\lambda\left[k^2\tilde{\mathbf{v}} + \mathbf{k}(\mathbf{k}\cdot\tilde{\mathbf{v}})\right]}{Dk^2 + \eta - \mathrm{i}\omega} \tag{2.30}$$

$$= \frac{-\lambda k^2\left[2\tilde{v}^L\hat{\mathbf{k}} + \tilde{\mathbf{v}}^T\right]}{Dk^2 + \eta - \mathrm{i}\omega} \ . \tag{2.31}$$

We again consider the correlation $\langle \mathbf{v}\cdot(\nabla\cdot\mathbf{Q})\rangle$, which is of the form

$$\left\langle \int \frac{\mathrm{d}^2\mathbf{k}\mathrm{d}^2\mathbf{k}'\mathrm{d}\omega\mathrm{d}\omega'}{(2\pi)^3}\tilde{v}_i(\omega',\mathbf{k}')[\mathrm{i}k_j\tilde{Q}_{ij}(\omega,\mathbf{k})]e^{\mathrm{i}[(\mathbf{k}+\mathbf{k}')\cdot\mathbf{r}-(\omega+\omega')t]}\right\rangle \ . \tag{2.32}$$

Substituting in Eq. (2.31) and $\tilde{\mathbf{v}} = \tilde{v}^L\hat{\mathbf{k}} + \tilde{\mathbf{v}}^T$ gives

$$-\lambda\int \frac{\mathrm{d}^2\mathbf{k}\mathrm{d}^2\mathbf{k}'\mathrm{d}\omega\mathrm{d}\omega'}{(2\pi)^3}\frac{e^{\mathrm{i}[(\mathbf{k}+\mathbf{k}')\cdot\mathbf{r}-(\omega+\omega')t]}}{Dk^2+\eta-\mathrm{i}\omega'}k^2(\langle\tilde{v}^L(\omega,\mathbf{k})\tilde{v}^L(\omega',\mathbf{k}')\rangle + \langle\tilde{\mathbf{v}}^T(\omega,\mathbf{k})\tilde{\mathbf{v}}^T(\omega',\mathbf{k}')\rangle) \ , \tag{2.33}$$

which, using Eq. (2.29), we calculate to be

$$\langle\mathbf{v}\cdot(\nabla\cdot\mathbf{Q})\rangle = -2\lambda\Delta\int\frac{\mathrm{d}^2\mathbf{k}\mathrm{d}\omega}{(2\pi)^3}\frac{k^2(\eta+Dk^2)}{(\eta+Dk^2)^2+\omega^2} \tag{2.34}$$

$$\left[\frac{2}{(\mu_L k^2+\Gamma)^2+\omega^{-2}(c^2k^2\rho_0-\omega^2)^2} + \frac{1}{(\mu_1 k^2+\Gamma)^2+\omega^2}\right] \ . \tag{2.35}$$

This, like the incompressible case, is always negative, further confirming that polar fluctuations drive extensile behaviour in the nematic field.

2.2.3 Solid case

Having established the expected extensile nematic behaviour in confluent tissues in the liquid state, we now repeat the analysis in the solid state, again in the highly damped limit. Here, the relevant hydrodynamic variables are the displacement field $\mathbf{u}$ from the stress-free configuration, as well as the velocity field $\mathbf{v}$ and the passive nematic field $\mathbf{Q}$. Our EOM in this case read [140]

$$\Gamma\mathbf{v} = A\nabla^2\mathbf{u} + B\nabla(\nabla\cdot\mathbf{u}) + \boldsymbol{\xi} \tag{2.36a}$$

$$\partial_t\mathbf{Q} = \boldsymbol{\Omega} + C\left[\boldsymbol{\nabla}\mathbf{u} + (\boldsymbol{\nabla}\mathbf{u})^{\mathsf{T}}\right] + D\nabla^2\mathbf{Q} - \eta\mathbf{Q}\ , \tag{2.36b}$$

where the constants A and B are the shear modulus and bulk modulus of the material respectively, both of which are positive [140], and $\boldsymbol{\xi}$ is a polar fluctuation term again given by Eq. (2.2). The coupling constant C between the strain and nematic fields leads to the development of strain anisotropy either parallel ($C > 0$) or perpendicular ($C < 0$) to $\mathbf{Q}$ [141]. We expect it to be positive for the same reason - outlined previously - that we expect λ to be positive, although the sign does not effect our result.

We then linearise again and focus on the highly damped limit to give

$$\Gamma\mathbf{v} = A\nabla^2\mathbf{u} + B\nabla(\nabla\cdot\mathbf{u}) + \boldsymbol{\xi} \tag{2.37a}$$

$$\eta\mathbf{Q} = C\left[\boldsymbol{\nabla}\mathbf{u} + (\boldsymbol{\nabla}\mathbf{u})^{\mathsf{T}}\right] + \lambda\left[\boldsymbol{\nabla}\mathbf{v} + (\boldsymbol{\nabla}\mathbf{v})^{\mathsf{T}}\right] + D\nabla^2\mathbf{Q}\ . \tag{2.37b}$$

We can now analyse Eq. (2.37) following a similar procedure as in the liquid case. In Fourier transformed space, we have

$$\tilde{\mathbf{v}} = -(A+B)k^2\tilde{u}^L\hat{\mathbf{k}} - Ak^2\tilde{\mathbf{u}}^T + \tilde{\boldsymbol{\xi}} \tag{2.38a}$$

$$\tilde{\mathbf{Q}} = \frac{\mathrm{i}C\left[\mathbf{k}\tilde{\mathbf{u}} + (\mathbf{k}\tilde{\mathbf{u}})^{\mathsf{T}}\right] + \mathrm{i}\lambda\left[\mathbf{k}\tilde{\mathbf{v}} + (\mathbf{k}\tilde{\mathbf{v}})^{\mathsf{T}}\right]}{Dk^2 + \eta}\ , \tag{2.38b}$$

where we have defined the coefficients A and B to eliminate Γ to ease notation. We have also decomposed $\tilde{\mathbf{u}}$ into longitudinal and transverse components, $\tilde{\mathbf{u}} = \tilde{u}^L(\mathbf{k})\hat{\mathbf{k}} + \tilde{\mathbf{u}}^T(\mathbf{k})$. In Fourier (spatial and temporal) transformed space, the expressions for $\tilde{\mathbf{u}}$ are

$$\tilde{u}^L = \frac{\tilde{\xi}^L}{-\mathrm{i}\omega + (A+B)k^2} \tag{2.39a}$$

$$\tilde{\mathbf{u}}^T = \frac{\tilde{\boldsymbol{\xi}}^T}{-\mathrm{i}\omega + Ak^2} \ . \tag{2.39b}$$

We are again interested in the sign of the equal-time equal-position correlation $\langle \mathbf{v} \cdot (\nabla \cdot \mathbf{Q}) \rangle$, which, from Eq. (2.6b), is of the form

$$\left\langle \int \frac{\mathrm{d}^2\mathbf{k}\mathrm{d}^2\mathbf{k}'\mathrm{d}\omega\mathrm{d}\omega'}{(2\pi)^3} \tilde{v}_i(\omega', \mathbf{k}')[\mathrm{i}k_j\tilde{Q}_{ij}(\omega, \mathbf{k})] e^{\mathrm{i}[(\mathbf{k}+\mathbf{k}')\cdot\mathbf{r} - (\omega+\omega')t]} \right\rangle \ , \tag{2.40}$$

where we now also have the time/frequency argument in the above expression since $\mathbf{v} = \partial_t \mathbf{u}$. With the above results, the equal-time correlation function is thus

$$\langle \mathbf{v} \cdot (\nabla \cdot \mathbf{Q}) \rangle = -\lambda \int \frac{\mathrm{d}^2\mathbf{k}\mathrm{d}\omega}{(2\pi)^3} \frac{k^2 \langle \tilde{v}_i(-\omega, -\mathbf{k}) \tilde{v}_i(\omega, \mathbf{k}) \rangle}{Dk^2 + \eta} \ , \tag{2.41}$$

where we integrate over all wavelengths up to an ultra-violet cut off. This integral is always negative if $\lambda > 0$, since the correlation $\langle \tilde{v}_i(-\omega, -\mathbf{k}) \tilde{v}_i(\omega, \mathbf{k}) \rangle$ is always positive (see Eq. (2.38)). The above results underline that, in the small fluctuations limit, polar fluctuations generically drive extensile nematic forces in the solid state.

2.3 Numerical Cell-resolution modelling

To validate our analytical results, we perform simulations on cell-based models of confluent tissues in both liquid and solid states [142]. We use the active vertex model (AVM) to explore the dynamics of the tissue in both solid and liquid states.

As in previous studies, we focus on the dynamics of +1/2 defects to determine the extensile or contractile nature of the nematic field [66]. In addition, we also calculate the isotropic stress fields around these defects arising from cell-cell interactions, to underline the consistency between our modelling and experimental results [29]. Finally, we then calculate the correlation $\langle \mathbf{v} \cdot (\nabla \cdot \mathbf{Q}) \rangle$ to demonstrate the consistency between using this method and examining defect dynamics as a means of determining nematic behaviour.

We first detail how we implement the AVM and our procedure for calculating the stress in the tissue, before describing how we detect defects in our system and analysing their dynamics. We then calculate $\langle \mathbf{v} \cdot (\nabla \cdot \mathbf{Q}) \rangle$.

2.3.1 Active vertex model implementation

The AVM represents the monolayer as a tiling of polygons; the cell vertices are the degrees of freedom in this model, and each cell is endowed with a self-propulsive motile force (Fig. 2.1). In addition to self-propulsion, vertices move in response to mechanical interactions stemming from an effective tissue energy function. As the only active forces explicitly included are polar, this model is comparable to our analytical model without the inclusion of active contractility and extensile behaviour is expected universally. Our effective tissue energy function is defined as

$$E = \sum_{a=1}^{N} K_A (A_a - A_0)^2 + K_P (P_a - P_0)^2 \ , \tag{2.42}$$

where N is the number of cells, K_A and K_P are the area and perimeter moduli, A_a and P_a are the area and perimeter of cell a, and A_0 and P_0 are the target area and perimeter common to all cells. The first term in Eq. (2.42) is quadratic in the cell areas and encodes a combination of cell volume incompressibility and the monolayer's resistance to height fluctuations. The second term in the energy

function is quadratic in the perimeter of the cells and encodes a competition between the cytoskeleton and cell membrane tension from cell-cell adhesion and cortical tension. The interaction force on vertex m is then $\mathbf{F}_m = -\nabla_m E$, which we calculate to be

$$\mathbf{F}_m = -\frac{\partial E}{\partial \mathbf{r}_m} = -\sum_{a\in\mathcal{N}(m)} \frac{\partial E_a}{\partial \mathbf{r}_m} \ , \tag{2.43}$$

where $a \in \mathcal{N}(m)$ denotes the 3 cells indexed by a that are neighbours to vertex m. The interaction force experienced by cell a is due to the shape of the cells that neighbour it. The energy derivatives are then

$$\begin{aligned}\frac{\partial E_a}{\partial \mathbf{r}_m} &= \frac{\partial E_a}{\partial A_a}\frac{\partial A_a}{\partial \mathbf{r}_m} + \frac{\partial E_a}{\partial P_a}\frac{\partial P_a}{\partial \mathbf{r}_m} \\ &= 2K_A(A_a - A_0)\frac{\partial A_a}{\partial \mathbf{r}_m} + 2K_P(P_a - P_0)\frac{\partial P_a}{\partial \mathbf{r}_m} \ .\end{aligned} \tag{2.44}$$

The area and perimeter derivatives are given by

$$\frac{\partial A_a}{\partial \mathbf{r}_m} = \frac{1}{2}(|\mathbf{r}_{mn}|\hat{\mathbf{n}}_{mn} + |\mathbf{r}_{mp}|\hat{\mathbf{n}}_{mp}) \quad , \quad \frac{\partial P_a}{\partial \mathbf{r}_m} = \hat{\mathbf{r}}_{mn} + \hat{\mathbf{r}}_{mp} \ , \tag{2.45}$$

where vertices p and n are the two vertices directly before and after m (respectively) when traversing the vertices of cell a in a clockwise loop. We denote $\mathbf{r}_{mn} = \mathbf{r}_m - \mathbf{r}_n$ as the cell edge connecting vertices m and n, $\hat{\mathbf{n}}_{mn}$ is the outward facing normal unit vector to that edge and $\hat{\mathbf{r}}_{mn} = \mathbf{r}_{mn}/|\mathbf{r}_{mn}|$.

To model cell motility, each cell is endowed with a self-propulsion force of constant magnitude f_0. This self-propulsion force acts along a polarity vector, $\hat{\mathbf{n}}_a = (\cos\theta_a, \sin\theta_a)$, where θ_a is an angle measured from the x-axis. The resultant self-propulsion force on each vertex is the average of the three self-propulsion forces of the cells that neighbour vertex m, $\mathbf{f}_m = \frac{f_0}{3}\sum_{a\in\mathcal{N}(m)} \hat{\mathbf{n}}_a$, where $\mathcal{N}(m)$ denotes the list of cells that share vertex m. Assuming overdamped dynamics and a large supply of

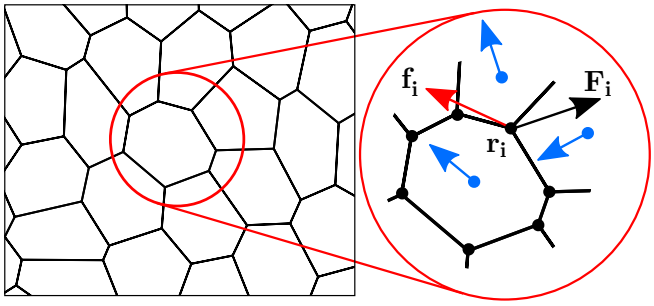

Figure 2.1: Schematic of the active vertex model. The degrees of freedom are the cell vertices (black dots). Each vertex experiences two types of forces, an active force from cellular self-propulsion, $\mathbf{f}_i$ (red arrow), which is the mean self-propulsive force from the 3 cells that neighbour each vertex (blue arrows), and the mechanical response of the tissue to this driving, $\mathbf{F}_i$ (black arrow).

ATP, the EOM of each vertex is defined as

$$\frac{d\mathbf{r}_m}{dt} = \frac{1}{\zeta}(\mathbf{F}_m + \mathbf{f}_m) \ , \tag{2.46}$$

where ζ is the damping coefficient. The polarity vector of each cell also undergoes rotational diffusion according to

$$\frac{d\theta_a}{dt} = \sqrt{2D_r}\xi_a(t) \ , \tag{2.47}$$

where $\xi_a(t)$ is a white noise process with zero mean and unit variance and D_r is the rotational diffusion coefficient. We implement the Euler-Mayurama method in C++ and numerically integrate Eq. (2.46) and Eq. (2.47) forward in time with time-step $\Delta t = 0.01$, and D_r^{-1} as our unit time.

We initialise the simulation by arranging N cells on a hexagonal lattice, with grid spacing $d = \sqrt{2/\sqrt{3}}$, in a periodic domain with dimensions $dN \times (\sqrt{2}/3)dN$. We then draw a Voronoi diagram from the seeded points to obtain the initial positions of the vertices. The choice of grid spacing gives edges of length $a = d/\sqrt{3}$ and ensures that all cells initially have unit area. This means the average cell area throughout the simulation $\bar{A} = 1$ and we use $\sqrt{\bar{A}}$ as our unit length. To ensure different realisations

of the system are independent, cells have random initial polarities and we integrate through at least 2×10^3 time units in the liquid state to initialise the system. We then quench the system at the desired p_0 value and run our simulations for 10^4 time units.

Prior to initialising, we create a series of lists storing each cells neighbours, which vertices belong to each cell and which three cells neighbour each vertex. The information is stored in a clockwise order and updated as cells rearrange, making accessing information much quicker when marching forward in time. These lists are then used throughout each time-step. For example, the list of which vertices belong to each cell is used when calculating the cellular area, perimeter and long axis direction, and the list of which cells neighbour each vertex is used when calculating both the active and interaction force on each vertex. At each time-step, we then calculate the area and perimeter of each cell, calculate the active force and interaction force on each vertex, update the vertex positions, update the polarisation directions and check if any cell rearrangements are required.

The vertex model has been shown to undergo a rigidity transition that is controlled by a single non-dimensional parameter, the target shape index $p_0 = P_0/\sqrt{A_0}$ [87]. In passive systems, where $f_0 = 0$, this transition occurs at $p_0 = p_0^* \approx 3.81$, although this decreases with increasing motility [95]. Above this critical value of p_0^* there are no energy barriers to cell rearrangements and the cell layer enters a liquid-like phase. We thus choose pairs of values of p_0 and f_0 to ensure $p_0^* < 3.81$ for our solid simulation and $p_0^* > 3.81$ for our liquid simulation.

We implement cell rearrangements in the form of T1 transitions when a cell edge length becomes lower than a threshold value, l_{T1} (Fig. 2.2). To perform a T1 transition, we rotate the edge to be switched (the edge shared by cells 2 and 3 in Fig. 2.2) about its centre such that it is parallel to a line connecting the centres of mass of the old neighbouring cells. The new edge length is then set to be equal to $1.5l_{T1}$ to

avoid switching back and forth of neighbours. After performing the exchange, we update the relevant neighbour and cell vertex lists, ensuring all elements are still stored in a clockwise order.

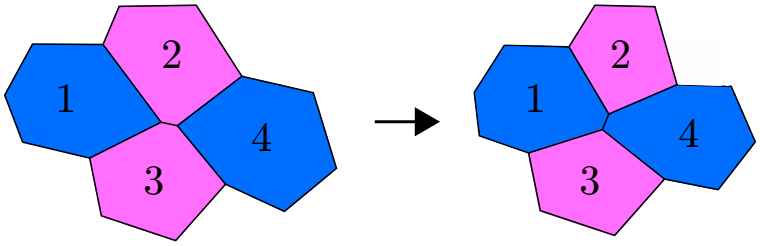

Figure 2.2: Cell rearrangements are performed via T1 transitions. When an edge becomes shorter than a threshold value, such as between cells 2 and 3 on the left, the edge is changed such that neighbours are exchanged and cells 1 and 4 become neighbours.

Unless otherwise stated, in the AVM we simulate $N = 400$ cells with parameters $A_0 = 1$, $D_r = 1$, $\Delta t = 0.01$ and a T1 transition threshold length, $l_{T1} = 0.01$. For the liquid state we use $P_0 = 3.7$ and $f_0 = 0.5$, and for the solid state $P_0 = 3.4$ and $f_0 = 0.5$. As the total area of the domain is N, the average area of each cell is $\bar{A} = A_0$. This models the cell layer as just reaching confluence.

2.3.2 Computing cell-cell interaction stress

To further compare our findings to experimental results, we calculate the mechanical stress in the tissue arising from cell-cell interactions, which we refer to as the interaction stress. Following a previous study on calculating stresses in vertex models [143], we calculate our interaction stress from gradients in the energy functional governing mechanical interactions in each model. We adopt the convention that the stress is negative when the cell is under compression. Specifically, for cell a, the

interaction stress is given by

$$\sigma_a = \frac{\partial E}{\partial A_a}\mathbb{1} + \frac{1}{2A_a}\sum_{mn\in\mathcal{V}(a)} \mathbf{T}_{mn}\mathbf{r}_{mn} \ , \tag{2.48a}$$

$$\frac{\partial E}{\partial A_a} = 2K_A(A_a - A_0) \ , \quad \mathbf{T}_{mn} = \frac{\partial E}{\partial \mathbf{r}_{mn}} = 2K_P[(P_a - P_0) + (P_b - P_0)]\hat{\mathbf{r}}_{mn} \ , \tag{2.48b}$$

where $\mathbf{T}_{mn}$ is the cell-edge tension and the summation is over all the edges in cell a, with mn being the cell edge connecting vertices m and n that separates cells a and b. The factor of $1/2$ in the cell-edge tension term is due to each edge being shared by two cells. From here, we find the normal stress on each cell to be the average of the diagonal terms. For the purposes of calculating the average properties of defects, this is defined at the centre of mass of each cell.

2.3.3 Computing the local cell orientation field

To analyse the properties of nematic defects, we must first calculate the average local orientation of cells in our system, which means we must define the long axis of each cell. We calculate the orientation of each cell's long axis by finding the eigenvector associated with the largest eigenvalue of each cell's shape tensor, S_a, which is a rank-2 tensor given by

$$S_a = \frac{1}{N_a}\sum_{m\in\mathcal{V}(a)} \mathbf{r}_{am}\mathbf{r}_{am} \ , \tag{2.49}$$

where $m \in \mathcal{V}(a)$ denotes the vertices of cell a and $\mathbf{r}_{am} = \mathbf{r}_m - \mathbf{r}_a$ is the vector from the centroid of the cell a, denoted by $\mathbf{r}_a$, to each vertex, m. The shape tensor S_a has two eigenvalues and the eigenvector associated with the larger (smaller) eigenvalue determines the major (minor) principal axis of the cell (Fig. 2.3a).

To find the local cell orientation field, or director field, we follow the methods used

in recent experimental studies [29, 20]. The domain is split into a grid, with each point on the grid representing the centre of a square window. The dimensions of the window are chosen such that each window contains on average 4–6 cells (Fig. 2.3b). A cell counts as being within a window if one of its vertices lies within that window. We then calculate the director field at each point on the grid by determining the nematic order tensor $\mathbf{Q}$ of the cells within the window associated with that point. In two dimensions, $\mathbf{Q}$ is given by

$$\mathbf{Q} = \begin{bmatrix} \langle \cos 2\theta_a \rangle & \langle \sin 2\theta_a \rangle \\ \langle \sin 2\theta_a \rangle & -\langle \cos 2\theta_a \rangle \end{bmatrix} , \tag{2.50}$$

where θ_a is the long axis orientation of cell a and $\langle \cdot \rangle$ represents an average over all the cells in the window. The eigenvector associated with the largest eigenvalue of $\mathbf{Q}$ is the local orientation of the cells in the window (Fig. 2.3c). The sizing of the windows to contain 4–6 cells acts to reduce nose in the director field and is in line with previous studies [29, 20]. This means, using the parameters detailed in the sections above, our director field is defined on an 18 by 18 grid, with a grid spacing in the x and y directions of $\Delta x = 1.19$ and $\Delta y = 1.03$ respectively. These points define the centre of our square windows, which have a side length of 1.19.

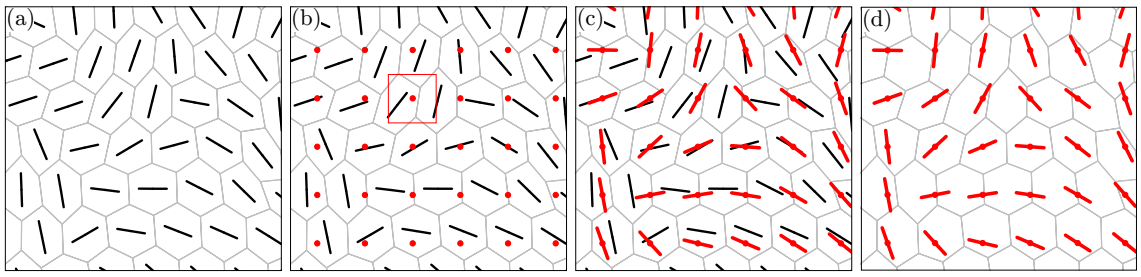

Figure 2.3: Procedure for calculating the director field. (a) The long axis of each cell is found. (b) A grid is overlaid on the domain, with each grid point defining the centre of a box (one shown in red for clarity) sized to contain vertices from 4–6 cells. (c) The mean orientation of the cells in each box is calculated from finding the largest eigenvalue of the nematic tensor. (d) The final director field.

2.3.4 Defect detection and analysis

Similarly to previous work [29, 20], we detect defects at a particular point in the director field by calculating the winding number, which is a measure of the angle of rotation of the director field along a closed loop of nearest neighbours (Fig. 2.4). The winding number around a given point in our director field is given by [64]

$$\Delta\beta = \sum_a \delta\beta_a \ , \tag{2.51}$$

where the sum is over the eight nearest neighbours around the point for which we are calculating the winding number and $\delta\beta_a$ is the change in the angle β of the director field when moving from neighbour a to neighbour $a+1$ in an anticlockwise direction. It is given by

$$\delta\beta_a = \beta_{a+1} - \beta_a + \gamma \ , \tag{2.52}$$

where γ is

$$\gamma = 0 \quad \text{if} \quad |\beta_{a+1} - \beta_a| \leq \pi/2 \tag{2.53a}$$

$$\gamma = +\pi \quad \text{if} \quad \beta_{a+1} - \beta_a < -\pi/2 \tag{2.53b}$$

$$\gamma = -\pi \quad \text{if} \quad \beta_{a+1} - \beta_a > +\pi/2 \ . \tag{2.53c}$$

The addition of γ ensures $\delta\beta_i$ is the smallest angle needed to turn from β_a to β_{a+1}. The topological charge, which we expect to be $\pm 1/2$ if it is non-zero, is then $\Delta\beta/2\pi$. To avoid double counting of defects these closed loops must not overlap, so we only detect defects at every other point, horizontally and vertically, on our grid.

To determine whether the defects behave in a contractile or extensile manner, we look at the behaviour of defects as they form. Indeed, in active solids where constituents fluctuate around an equilibrium position, such as in the solid state of our AVM, restoring forces will eventually pull the tissue back to equilibrium as the active

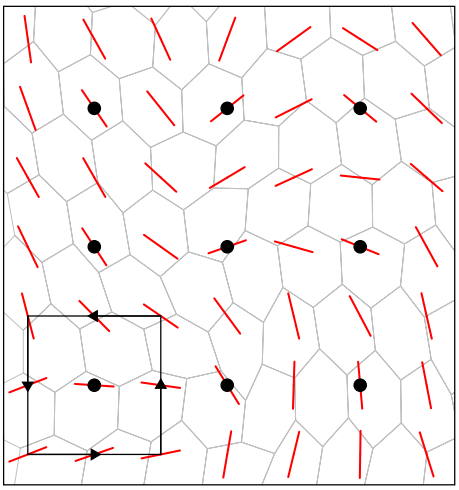

Figure 2.4: Defects are detected at every other director field grid point (black dots). The winding number is calculated by summing the change in angle α of the director field when traversing an anti-clockwise closed loop around the nearest neighbours of each detection site. An example is shown in the bottom left.

behaviour varies with the diffusion of the polarity vector [66]. When the material behaves in an extensile manner, we expect the defect to initially move in a tail-to-head direction; however, the restoring force may eventually pull the defect back making it move in a head-to-tail direction (while the material remains extensile). To analyse the properties of defects, we thus only examine defects that have formed in the previous ten time-steps, however, we note that this is not necessary when analysing the behaviour of defects in the liquid state, as the tissue can rearrange. In this regime, we can average behaviour over all detected defects and obtain similar results to those found when studying 'new' defects.

We ensure that we detect defects at statistically independent times by calculating the temporal autocorrelation function for the velocity field $\mathcal{C}_v$ and nematic tensor field $\mathcal{C}_Q$ which are defined as

$$\mathcal{C}_v(\tau) = \left\langle \frac{1}{2}\sum_{i=1}^{2}\frac{1}{Ts_i^2}\sum_{t=1}^{T-\tau}[v_i(t)-\bar{v}_i][v_i(t+\tau)-\bar{v}_i]\right\rangle \tag{2.54a}$$

$$\mathcal{C}_Q(\tau) = \left\langle \frac{1}{4}\sum_{i=1}^{2}\sum_{j=1}^{2}\frac{1}{Ts_{ij}^2}\sum_{t=1}^{T-\tau}[Q_{ij}(t)-\bar{Q}_{ij}][Q_{ij}(t+\tau)-\bar{Q}_{ij}]\right\rangle , \tag{2.54b}$$

where s^2 is the variance of the component, T is the length of the time-series, τ is the time-lag and angled brackets represent a spatial average. We then fit an exponential function to the plots to obtain decorrelation times, which are approximately 0.5 and 6 time-units for $\mathbf{v}$ and $\mathbf{Q}$ respectively in the AVM (Fig. 2.5). Similar values were found for the solid state. We thus sample for detects every 10 time units (1000 time-steps). To summarise, every 1000 time-steps we save the winding number at each defect detection point for ten time-steps. For each defect detection point we then check whether a defect has appeared at that point in any of the previous saved time-steps (i.e. has the winding number changed from zero to a non-zero value). If it has we then save the position and topological charge at that point.

We analyse the properties around defects by first finding their orientation using the process described in [144]. Specifically, the orientation of a defect is defined as

$$\psi = \frac{k}{1-k} \arctan\left[\frac{\mathrm{sgn}(k)\partial_x Q_{xy} - \partial_y Q_{xx}}{\partial_x Q_{xx} + \mathrm{sgn}(\partial_y Q_{xy})}\right], \tag{2.55}$$

where k is the topological charge of the defect and ψ is defined in Fig. 2.6. For $+1/2$ defects, it is the angle between the vector from the defect core to the tail of the

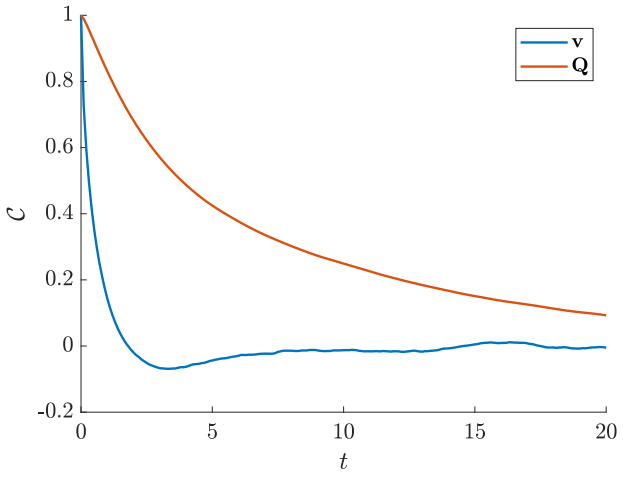

Figure 2.5: Temporal autocorrelation functions for the velocity field $\mathcal{C}_v$ and nematic tensor field $\mathcal{C}_Q$ in the AVM liquid state. Similar results were found for the solid state.

defect and the x-axis and, for $-1/2$ defects, ψ is the angle between a vector from the defect core to one of the points of the trefoil shape and the x-axis (Fig. 2.6). We calculate the derivatives of $\mathbf{Q}$ at the defect site using a central difference scheme on our director field grid. We then align the defects and crop the field of interest around them before interpolating the points at which they are defined, either the cell vertices when calculating the velocity field or the cell centres when calculating the stress field, to a grid. We then average over detected defects of a particular type. All results shown are averaged over approximately 10000 defects from at least ten independent simulations.

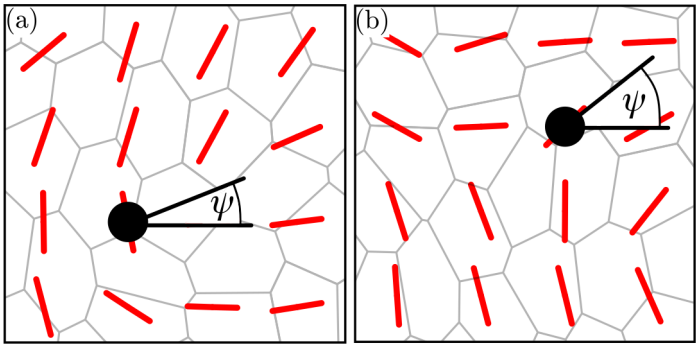

Figure 2.6: Example calculated defect orientation ψ for (a) $+1/2$ defects and (b) -1/2 defects.

Despite its simplicity, we observe that the AVM, in both solid and fluid states, displays $\pm 1/2$ defects generated randomly within the tissue in a similar manner to those observed in epithelial layers *in vitro* [29] (Fig. 2.7a-d, left). Upon computing mean properties of the tissue around these defects, we observe velocity fields indicative of extensile active nematic behaviour, with the $+1/2$ defect moving in a tail to head direction (Fig. 2.7a and c, middle) [66].

We also show the mean isotropic stress due to cell-cell interactions in Fig. 2.7a-d(right). The patterns show good qualitative agreement with those found in epithelial layers [29], with same compressive stresses in the head portion of $+1/2$ defects in our model as those found to trigger extrusion in the experimental system.

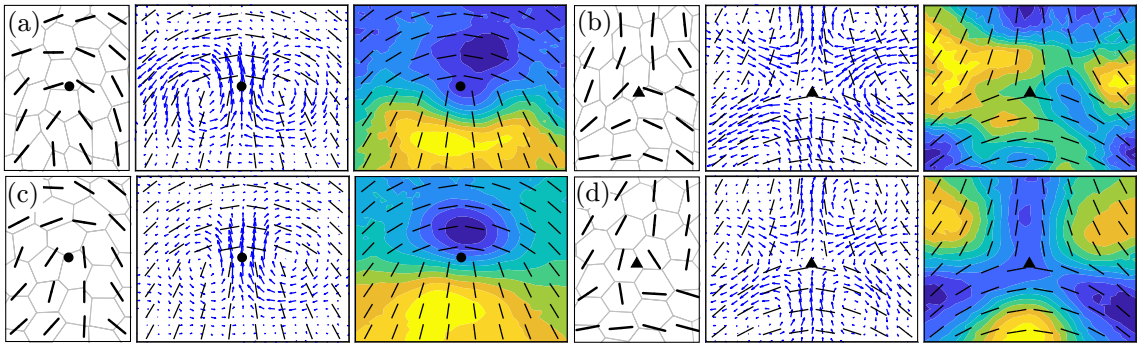

Figure 2.7: Simulation results of confluent tissues in their liquid ((a) and (b)) and solid ((c) and (d)) states. Nematic configurations, dynamics, and passive stress fields around detected $+1/2$ defects in the (a) liquid state and (c) solid state, and those of detected $-1/2$ defects in the (b) fluid state and (d) solid state. In each case, we show representative defects (left), mean velocity fields around defects (middle), and heat maps of mean isotropic passive stress $(\sigma_{xx} + \sigma_{yy})/2$ due to cell-cell interactions around defects (right). Heat maps have been normalised such that blue represents maximum compression and yellow maximum tension. We use $A_0 = 1$, $K_A = 1$, $K_P = 1$, $f_0 = 0.5$ and $D_r = 1$. In the liquid state we use $P_0 = 3.7$ and in the solid state $P_0 = 3.4$.

We note that the only type of topological defects consistently observed were defects with half-integer charges. Further, the extensile behaviour is apparent over a range of stiffnesses and activities, and collective contractile behaviour was never seen over the parameter ranges explored, in full support of our analytical findings.

2.3.5 Numerical calculation of correlations

We further support our analytical results by calculating the correlation $\langle \mathbf{v} \cdot (\nabla \cdot \mathbf{Q}) \rangle$ in our numerical models in both solid and liquid states. To do this we calculate the spatially averaged cross-correlation coefficient function $\mathcal{C}$ between $\mathbf{v}$ and $\nabla \cdot \mathbf{Q}$. The cross-correlation function measures the correlation between a time series and lagged versions of another time series as a function of the lag, τ. We then integrate this correlation function over the time-lag. A negative integral corresponds to a negative correlation and extensile behaviour. We do this, as opposed to calculating the average correlation coefficient between the two quantities at the same time-step,

because our analytical model is coarse-grained in time, so any correlation calculated implicitly includes some averaging in time. For two arbitrary 2D vectors $\mathbf{x}$ and $\mathbf{y}$ the cross-correlation coefficient function is

$$\mathcal{C}_{xy}(\tau) = \begin{cases} \left\langle \frac{1}{2}\sum_{i=1}^{2} \frac{1}{T s_i^x s_i^y} \sum_{t=1}^{T-\tau} [x_i(t) - \bar{x}_i][y_i(t+\tau) - \bar{y}_i] \right\rangle, & \tau > 0 \\ \left\langle \frac{1}{2}\sum_{i=1}^{2} \frac{1}{T s_i^x s_i^y} \sum_{t=1}^{T+\tau} [x_i(t) - \bar{x}_i][y_i(t+\tau) - \bar{y}_i] \right\rangle, & \tau < 0 \end{cases} \tag{2.56}$$

where $\bar{x}$ and $\bar{y}$ denote the means x of y, s the standard deviation and angled brackets denote a spatial average. To calculate the correlation of interest $C_{\mathbf{v}\cdot(\nabla\cdot\mathbf{Q})}$, we interpolate the velocity field to the grid points at which our director field, and therefore $\mathbf{Q}$, is defined. We then obtain the necessary gradient information using a central differencing scheme on this grid. We then calculate $C_{\mathbf{v}\cdot(\nabla\cdot\mathbf{Q})}$ at spatially independent points in our director field and take the average before integrating over time.

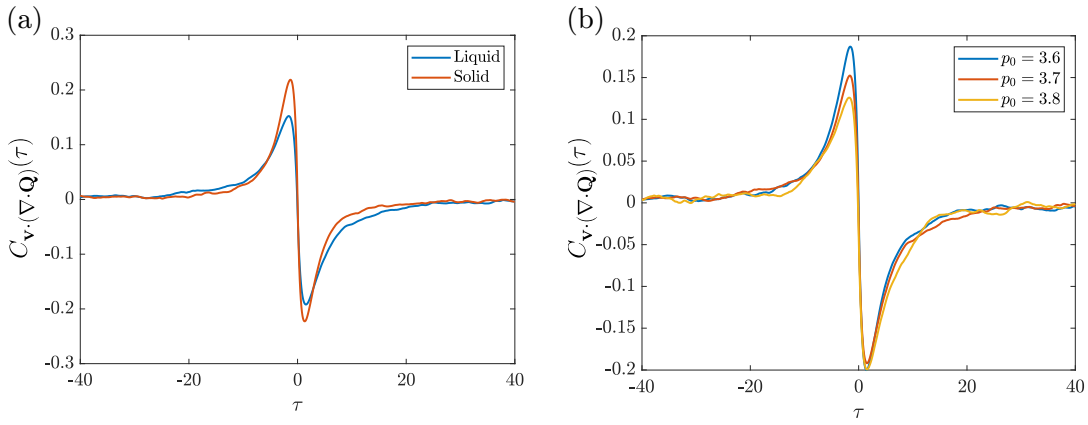

Figure 2.8: Temporal cross-correlation coefficient functions between $\mathbf{v}$ and $\nabla\cdot\mathbf{Q}$ (a) for the liquid and solid states and (b) for different values of p_0. While the peak of the negative portion of the curves is similar in magnitude for all values of p_0, the peak of the positive contribution decreases with increasing p_0.

Both solid and liquid states have a negative correlation at positive lags in time, but a positive correlation at negative lags (Fig. 2.8a). The negative contribution is due to the self-propulsive active force $\mathbf{f}$, while the positive contribution is due to the passive response of the material $\mathbf{F}$ generating contractile forces (Fig. 2.9). These contractile forces arise because, while the average cell area in the domain is equal to

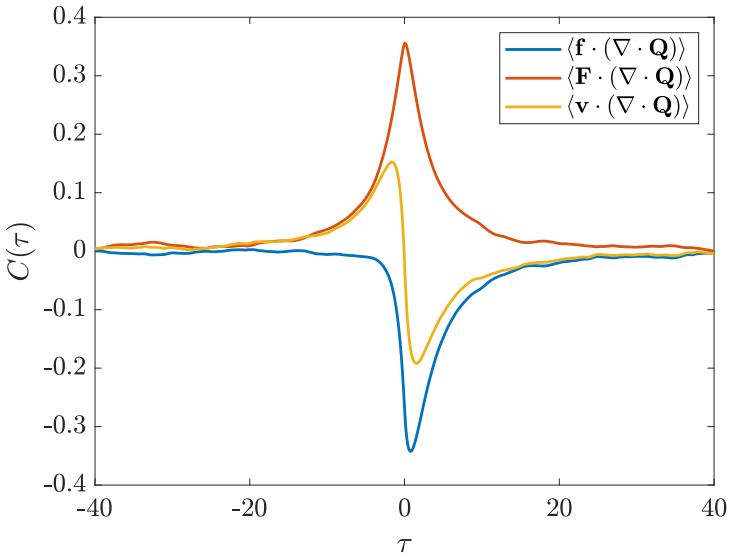

Figure 2.9: Temporal cross-correlation coefficient functions between the self-propulsive force $\mathbf{f}$ and $\nabla \cdot \mathbf{Q}$, the mechanical response of the material $\mathbf{F}$ and $\nabla \cdot \mathbf{Q}$, as well as between $\mathbf{v}$ and $\nabla \cdot \mathbf{Q}$ for the liquid state. While the correlation is exclusively negative for $\mathbf{f}$, it is exclusively positively for $\mathbf{F}$, meaning the correlation for $\mathbf{v}$ has a positive and negative component.

their target area, the average perimeter of cells in the model is always larger than their target perimeter, even in the liquid state (Fig. 2.10).

This is further evidenced by the positive contribution in the correlation decreasing as we move deeper into the liquid state, where the mechanical response of the tissue plays a smaller role in the dynamics (Fig. 2.8b). However, the integrals for both liquid and solid states in Fig. 2.8a are negative overall (-3.224 and -0.281 respectively) indicating statistically extensile behaviour, in agreement with our analytical results and observed defect motion. This highlights the compatibility of the measure of extensility we use in our analytical model with that more commonly used experimentally. Moreover, the purely negative correlation between $\mathbf{f}$ and $\nabla \cdot \mathbf{Q}$ further underlines that polar forces drive extensile behaviour in the nematic field (Fig. 2.9). Overall, our simulation results thus fully support our analytical findings.

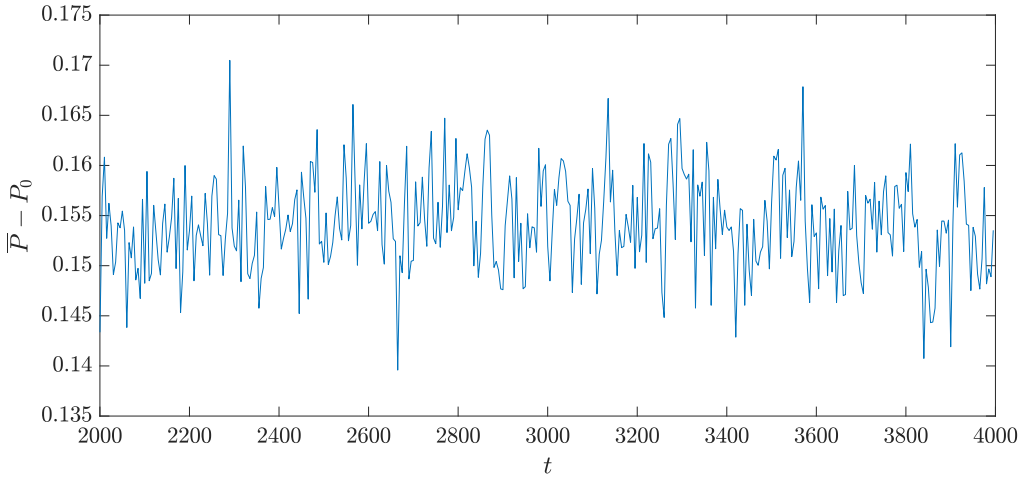

Figure 2.10: Time evolution of the average cell perimeter $\overline{P}$ relative to the target perimeter P_0.

2.4 Discussion

We demonstrate analytically that planar confluent tissues with polar fluctuations lead generically to extensile nematic behaviour with regards to cell shape orientation in the limit of small fluctuations. In contrast to previous studies, our analysis does not require the addition of *ad-hoc* extensile nematic terms [34, 85, 129]. Further, our analytical treatment applies universally in the small fluctuation regime and thus elucidates how extensile behaviour can emerge even though contractile nematic stresses are prevalent at the cellular scale. We confirm all our findings by simulating models of confluent tissues in both liquid and solid states.

Our findings highlight the role cell-substrate interactions, arising from fluctuating polar traction forces, play in governing collective tissue behaviour. With previous emphasising the importance of cell-cell interactions [85, 20, 86], one key conclusion of this work is that key physics of the system are not captured if cell-substrate interactions, specifically polar cell-substrate interactions, are not included. A further crucial point this work highlights is the effect fluctuations can have on system dynamics. Although biological systems are clearly very noisy environments, they

are often omitted from studies using active nematic models, although their importance is beginning to be recognised [145, 86]. This work underlines further their importance in properly characterising biological systems.

We note that a recent joint experimental and theoretical work investigating the switch from contractile cells to extensile tissues concluded that the extensile behaviour of epithelial tissues may come from strong intercellular interactions mediated by cadherins [20]. Our result here is consistent with their findings if stronger intercellular interactions lead to a reduction in the fluctuations/strength of the active nematic contractility due to the increased rigidity at the cellular level. Additionally, a recent study has found that cadherin-mediated cell-cell contacts support the formation of cryptic lamellipodia [19], meaning stronger intercellular interactions could also facilitate stronger polar traction forces.

We also note that our findings have been subsequently corroborated by numerical simulations of a hydrodynamic nematic model [145]. This study focussed of the role of the flow alignment parameter λ in inducing defect dynamics in a passive nematic material with fluctuations. They concluded that the sign of λ controls whether the defects move in an extensile-like or contractile-like manner, in full agreement with our passive findings. Finally, since our main motivation comes from experiments, we focus here exclusively on confluent tissues, however, due to the use of hydrodynamic models we expect our theory to apply equally to many-body systems of deformable particles or elongated particles. Indeed, we argue that our results could explain the previously unresolved extensile motion of $+1/2$ defects seen in 2D layers of rod-shaped molecules on a vibrating substrate [146].

Chapter 3

Machine learning of nematic defects

3.1 Introduction

Due to the prevalence and functional role of $\pm 1/2$ defects in many systems [124], the efficient detection and characterisation of topological defects in confluent tissues, and cellular systems generally, is of fundamental interest to both biology and physics. The application of defect detection algorithms to imaging data often requires a sophisticated understanding of the underlying physics. Current algorithms usually entail locating degenerate points in the nematic field followed by inspecting how the orientation of the nematic field changes around this point [147], usually by calculating the winding number. This can be effective in systems where the nematic field is well defined across the domain [148, 149] including tissues where cells are elongated or rod-like, such as spindle shaped fibroblasts [28]. However, this method is not suited to systems where the nematic field is not well-defined everywhere, as degenerate points in the field could just be areas of low order and do not necessarily indicate the existence of a defect.

This is often the case in confluent tissues such as epithelial layers, which are similar in morphology to our active vertex model (AVM), where the cells are not rod-like and can be nearly isotropic in shape at times. Indeed, the large areas with low nematic ordering raises questions as to how appropriate modelling these systems as nematic truly is; a question that our work in Chapter 2 also raises. There have been recent proposals that a more general description p-atic, particularly hexatic, order may be more relevant [150]. However, a growing number of experimental studies are seeking to detect nematic defects in these systems and finding that they are playing functional roles in biological processes [29, 20, 151, 152], meaning there is still a growing need for efficient detection methods.

Previous work studying defects in these systems used the method we implemented in Chapter 2 [29, 20, 151]. As opposed to locating degenerate points in the nematic field, we searched for defects by calculating the winding number on a pre-defined grid of points in the field. However, while analysing defects in our AVM in the previous chapter, it became clear that this method for detecting defects, which is the current standard technique for epithelial tissues, was cumbersome and inefficient. This was evidenced by the many steps needed to successfully implement the method, and the need for thousands of defects to be detected to adequately discern the average tissue stress and velocity fields, which are often the target of experimental studies. The necessity of such large amounts of data suggests the method of defect detection is inefficient and imprecise, which begs the question as to whether better methods of detection are possible for these systems.

One possibility is to utilise machine learning to improve defect detection. Machine learning methods are being exploited in an increasing variety of applications in active nematic systems [153, 110, 154]. They have also been used to detect topological defects in various systems [155, 118, 156], including cellular systems [119]. This previous study identified degenerate points in the nematic field of a cellular layer and

then used a four layer, fully-connected neural network to perform a binary classification by labelling the points as either $+1/2$ or $-1/2$ defects. However, as previously discussed, this method is less applicable to experimental cellular systems where the nematic field is not well-defined everywhere, and points with low nematic order do not necessarily indicate the existence of a defect. Additionally, this study did not demonstrate that its machine learning method outperformed existing techniques for detection. As such, there is still a need to develop a machine learning method that can be readily utilised in an experimental setting.

In this chapter, we address this problem by developing a methodology to detect nematic defects in confluent tissues using a convolutional neural network (CNN). We design the method such that it is well suited for use in systems that currently lack effective detection techniques, is user-friendly and readily implementable on experimental data. In contrast to previous work, we show that it outperforms current detection techniques and further demonstrate its efficacy by finding the mean velocity field around $+1/2$ defects. We compare this to defects detected using the winding number method, highlighting the improvement in capturing properties of topological defects with limited data.

3.2 Defect detection methodology

3.2.1 Acquisition of test and training data

For our method to be valuable, it needs to be suitable for use on experimental data. For this reason, it takes as its input the x and y coordinates of each cells centre of mass and the orientation of the long axis of each cell, both of which can be readily acquired using standard segmentation software [157]. However, a large amount of data is required to adequately train and test the model. To obtain sufficient

amounts of data, we train and test our model using simulated data from the AVM developed in Chapter 2. We implement it in an identical manner as that described in Section 2.3.1, using the same parameter values as those used for the liquid state, although we do not anticipate the state of the tissue affecting the validity of the method. We then find the angle of the long axis of each cell using the method described in Section 2.3.3 and its x and y coordinate from the centre of mass of its vertices.

3.2.2 Identifying inputs to machine learning model

To process our input such that it is in a form that a machine learning model can classify $\pm 1/2$ defects, we first identify 'regions of interest' (ROIs) within the domain. As defects by definition occur in regions with low nematic order, we identify these areas as ROIs. To do this, we interpolate our cell orientation data to a fine grid, with grid spacing $\Delta x = \Delta y = 0.2$, where the average cell length is approximately 1 length unit. We then average each point over a sliding window, of size $9\Delta x \times 9\Delta x$, to smooth out the data and create a nematic field (Fig. 3.1a and b). At each grid point we then calculate the scalar nematic order parameter $S = \langle \cos 2\theta \rangle$, where θ is the orientation of the field at that point and $\langle \cdot \rangle$ represents a spatial average over a sliding window of the same size as that used for the nematic field.

As we seek areas of low order, we identify contiguous areas in our domain where S is below a threshold value $S_{th} = 0.15$. We then take the centres of mass of these areas to be the centres of our ROIs, cropping the field in a square around these points (Fig. 3.1b). The value of S_{th} is chosen such that it is high enough to capture all disordered regions that may contain defects, but low enough such that these regions are distinct and do not coalesce. Our ROIs are 9×9 grid points in size. We size our ROIs such that they contain 4-6 cells, large enough so as to capture the core of the defect but small enough to isolate the defects and avoid capturing multiple defects

in a single ROI. We then use our ROIs as inputs into a machine learning model that classifies them as containing a $+1/2$ defect, $-1/2$ defect or neither (Fig. 3.1c).

The ROIs in our method are approximately two length units across, as this is the approximate size of the defect cores in the AVM. However, this may not be the case in experimental systems, where defects could be a variety of sizes relative to the size of the cell. As such, when applying this method to the systems, the input coordinates should be scaled such that the width of the defect core corresponds to two units in the coordinate length-scale.

As the position of potential defect locations (the centres of our ROIs) can be located anywhere in the system domain, our method is effectively off-lattice in its detection, although they still lie on a fine grid. This is in contrast to the previously developed method used in Chapter 2 [29, 20], which can only detect defects at predefined locations on a coarse-grained lattice.

3.2.3 Model architecture and training

We use a CNN to classify our ROIs. A schematic of the architecture can be seen in Fig. 3.1c. We use two convolutional layers, each detecting 32 features, the first has feature detectors of size 6×6 and the second 3×3. We then follow these convolutional layers with an additional fully-connected layer of 100 artificial neurons before our output layer of three neurons, representing our three possible outputs, or classes, of a $+1/2$ defect, $-1/2$ defect or no defect. We chose this architecture as it achieved the highest classification accuracy on the training data, although we note that our results are not sensitive to the particular architecture used and similar architectures achieved a comparable, albeit slightly lower, accuracy.

Having a third output of no defect is key here and what makes our method particularly well suited to epithelial tissues. As the cells in our tissue do not have a

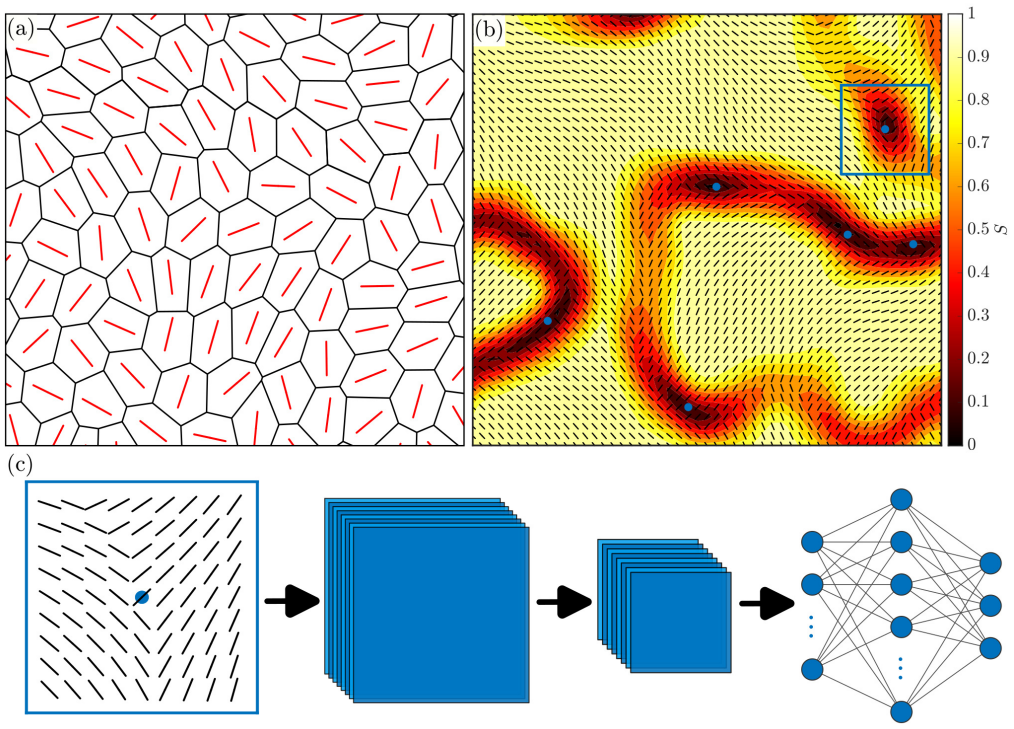

Figure 3.1: Defect identification and classification procedure. (a) The x and y coordinates of each cells centre of mass are found, the orientation of each cells long axis is then plotted at these points. (b) This information is then interpolated to a finer grid to form the nematic field of the system, where the average local scalar nematic order parameter S can be calculated at each grid point using a sliding window. Areas of low order ($S_{th} < 0.15$) are identified as possible defect regions and the centres of mass of these regions are identified (blue dots). The nematic field around these points is then cropped to form a region of interest (ROI) (blue box). (c) These ROIs are then input into a machine learning model which classifies them as a $+1/2$ defect, a $-1/2$ defect or not a defect.

well defined long axis, neighbouring cells are not always nematically aligned and there can be regions with low nematic order that do not necessarily contain nematic defects. Including an option for our CNN to classify an ROI as having no defect accounts for this possibility.

The output of our convolutional and fully-connected layers are rectified linear units, which take the form

$$a_j^i = \max\left(0, \sum_{k=1}^{K} w_{jk}^i a_k^{i-1}\right) , \tag{3.1}$$

where a^i_j is the output of the j^{th} neuron in layer i, K is the number of inputs to this neuron and w^i_{jk} is the weight of the connection from the k^{th} neuron in the previous layer to j^{th} in layer i. The output from the output layer L is known as a 'softmax' function, which takes the form

$$a^L_j = \frac{e^{z^L_j}}{\sum_{j=1}^{3} e^{z^L_j}} \ , \tag{3.2}$$

where z^L_j is the weighted sum of all the outputs from the previous the layer $z^L_j = \sum_{k=1}^{K} w^L_{jk} a^{L-1}_k$. The idea behind softmax is that the outputs sum to one, meaning they can be thought as the probability each class is the correct classification for the current ROI. We define the classification of each ROI as the class with the largest probability.

To generate training and testing data we manually label 5000 ROIs, using 4500 to train our model and saving 500 for testing. Manually labelling entails classifying by eye each automatically detected ROI as containing no defect, a $+1/2$ defect, or a $-1/2$ defect. To enlarge our training data we generate three new copies of each training ROI by rotating each one by angles $-\pi/2$, $\pi/2$ and π. Also, as the type of defect is invariant under reflections, we double this enlarged training data by reflecting each ROI about its centreline, leading to 36000 training inputs. As we only enlarge our training data so as to better tune the performance of our model, and the testing data serves to check model performance, we do not enlarge our testing data set.

We train our model by minimising the cross-entropy cost function, with an additional regularisation term, defined as

$$C = -\sum_{i=1}^{N}\sum_{c=1}^{3} y_{i,c} \log p_{i,c} + \frac{\lambda}{2} \sum_{j \in \mathrm{FC}} w_j \ , \tag{3.3}$$

where N is the number of items in each batch of training data, $y_{i,c}$ is the correct

label (0 or 1) for class c of the i^{th} ROI and $p_{i,c}$ is the output from the softmax layer of the network, the probability calculated by the model that the i^{th} ROI belongs to class c. To reduce overfitting to the training data, we use a process known as regularisation on the fully-connected layer. This entails adding the second term to the cost function, where the sum j is over weights connecting inputs or outputs to the fully-connected layer FC and $\lambda = 0.01$ is the regularisation parameter. This term penalises large weights and so favours correct classifications with smaller weights that are less likely to get trapped in local minima upon fitting.

We minimise C using a stochastic gradient descent algorithm with a batch size of $N = 64$ ROIs. That is, we calculate the cost function for groups of 64 ROIs, we then use this to estimate the gradient of our cost function with respect to the weights of our neurons and update our neuron weights according to

$$w_i \mapsto \begin{cases} w_i - \eta \frac{\partial C}{\partial w_i} - \lambda w_i \ , & \text{if } w_i \in \text{FC} \\ w_i - \eta \frac{\partial C}{\partial w_i} \ , & \text{otherwise} \end{cases} \tag{3.4}$$

where η is our learning rate. We then repeat this for another batch of ROIs, repeating until we have used all of our training data. One run through all of the training data is called an 'epoch'. We train over 20 epochs with a learning rate of 0.05 for the first ten epochs and 0.005 for the following ten. For each epoch, a random 10% of our training images are held back for validation and used at the end of the epoch to assess the accuracy of our model. Training for more than 20 epochs did not lead to any appreciable improvements in validation accuracy.

When training the model we use a concept known as dropout on the fully-connected layer, which involves not using a random 50% of the neurons in each training batch. This helps to reduce overfitting to the training data, as the network is not over-reliant on, and sensitive to, certain neurons. We implement our model in Python using the TensorFlow library and initialise each weight with a Glorot normal distribution [158].

This is a normal distribution with zero mean and variance $\sigma^2 = 2/(n_{in}+n_{out})$, where n_{in} for a given weight is the number of inputs to the neuron the current weight is providing an input for. Similarly, n_{out} is the number of outputs from the neuron in the previous layer the current weight is providing an output from. Scaling the distribution in this way ensures all neuron inputs have similar initial distributions. It also ensures these distributions are not too wide and the initial inputs to some neurons are erroneously large in magnitude, which would increase the amount of training needed to bring the inputs to the correct size.

3.2.4 Winding number calculation and comparison

Manually labelling the ROIs allows a direct comparison between our method and the current standard technique used in defect detection, calculation of the winding number, to be drawn, as we can also classify each ROI by calculating its winding number. We can then find the accuracy of both methods when compared against our manually labelled ROIs, our 'ground truth'. Previous work on applying machine learning to detect nematic defects in tissues has used the winding number as the ground truth [119], thereby making it impossible to determine if the machine learning method is superior to current techniques. We classify each ROI by calculating the winding number, in the manner detailed in Section 2.3.4 on the fine grid around the edge of the ROI.

3.3 Model performance

3.3.1 Classification performance

The mean performance of our CNN model with each training epoch can be seen in Fig. 3.2a. After training, our model clearly outperforms the winding number for

overall classification accuracy on the training data set, defined as the percentage of correct predictions. However these are ROIs that our model is being trained on, meaning it has 'seen' them before in previous training epochs. The real utility of our method depends on its ability to classify ROIs it has not seen before, which we test using the 500 ROIs in our test data set. Here our model is again more accurate than the winding number, achieving an accuracy of 84.0% compared to the winding numbers 76.6%, demonstrating that our method outperforms the current most widely used technique.

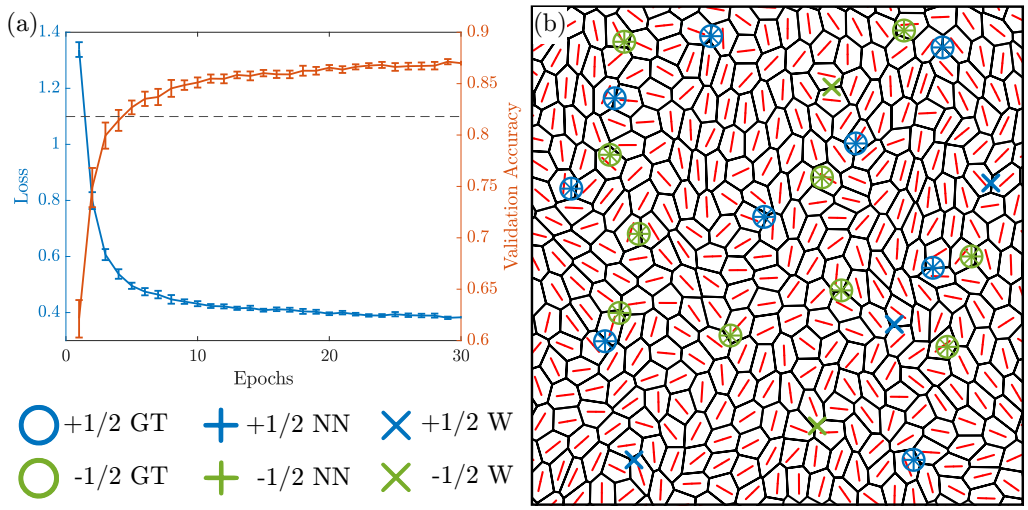

Figure 3.2: Machine learning model outperforms winding number classifier. (a) The loss and validation accuracy of the neural network as it is trained. The dashed line represents the accuracy of the winding number classification on the training data (0.812). Error bars represent the standard error in the mean over 50 realisations. (b) An example domain with defects detected using each method: our ground truth (GT), neural network (NN) and winding number (W).

As an example of the defects detected using each method, we look at an example domain from our AVM containing ROIs from our test data set (Fig. 3.2b). In line with Fig. 3.2a, both techniques show good agreement with manually labelled defects although the winding number appears to detect more false positives than the neural network. To assess this further and properly delineate the efficacy of both methods, we break down their performance for each class in Table 3.1. We calculate the

	+1/2			**No defect**			**-1/2**			**Total**		
	P	S	F1	P	S	F1	P	S	F1	P	S	F1
NN	0.786	0.967	0.867	0.932	0.663	0.775	0.818	0.964	0.885	0.856	0.840	0.834
WN	0.729	0.974	0.834	0.960	0.457	0.619	0.707	1.000	0.828	0.819	0.766	0.743

Table 3.1: Performance of defect detection methods on test data. Precision (P), sensitivity (S) and F1 score for each class, as well as an average over all classes, weighted by the size of that class.

precision, sensitivity and F1 score of each method. The precision is defined as

$$\mathrm{P} = \frac{\text{True Positive}}{\text{True Positive} + \text{False Positive}} \,, \tag{3.5}$$

and determines what proportion of detections are correct. It quantifies how detrimental false positives are to performance. Sensitivity, on the other hand, examines the role of false negatives in performance. It is defined as

$$\mathrm{S} = \frac{\text{True Positive}}{\text{True Positive} + \text{False Negative}} \,, \tag{3.6}$$

and establishes what proportion of true defects are actually identified. The F1 score, defined as

$$\mathrm{F1} = \frac{2\mathrm{PS}}{\mathrm{P} + \mathrm{S}} \,, \tag{3.7}$$

is a weighted average of the precision and sensitivity and so is a broader metric of performance.

Both methods display a similar pattern of having a higher sensitivity than precision for both defect categories, but a higher precision than sensitivity when no defect is present. Additionally, both methods exhibit a lower F1 score when no defect is present, a reflection of the larger differential between precision and sensitivity scores. Errors in both methods, therefore, primarily come from falsely detecting defects, as opposed to missing defects that should be detected. This information is lost when looking just at the weighted average values across all classes, which give more comparable precision and sensitivity scores.

Where the two methods differ is in our CNN model having consistently higher F1 for each category. This is driven by its higher precision in each defect class and higher sensitivity when no defect is present. The winding number, however, is slightly more sensitive to detecting defects when they are present. Taken together, these results show that the improved performance of our neural network compared to the winding number primarily stems from it detecting fewer false positive defects. It could be argued that precision and sensitivity should not be weighted equally, as they are in the F1 score, and that there may be scenarios where ensuring detecting as many defects as possible is more important than minimising detecting defects that are not there. However, we now show that, while the winding number may detect a slightly higher proportion of defects, the higher overall performance of our model can manifest itself in a wider improvement to experimental results.

3.3.2 Impact on data analysis

While results thus far point to the effectiveness of our model. To show that this realises itself in tangible improvements to wider results, we look at the ability of our model, and the winding number, to ascertain the properties of defects. As discussed previously, experimental studies are often more concerned with tissue properties around defects than the positions of defects themselves [29, 20], as this allows one to determine the collective behaviour of the tissue. Here we focus on calculating the average velocity field around $+1/2$ defects, as this is usually of the most in experiments, although we expect the ability of the different methods to capture the velocity field efficiently is indicative of its efficacy in uncovering other tissue properties, such as the stress field.

As we determined in Chapter 2, $+1/2$ defects in this AVM move in a tail-to-head direction, indicating extensile behaviour. However, obtaining the characteristic extensile flow field required averaging the velocity field over many simulations and

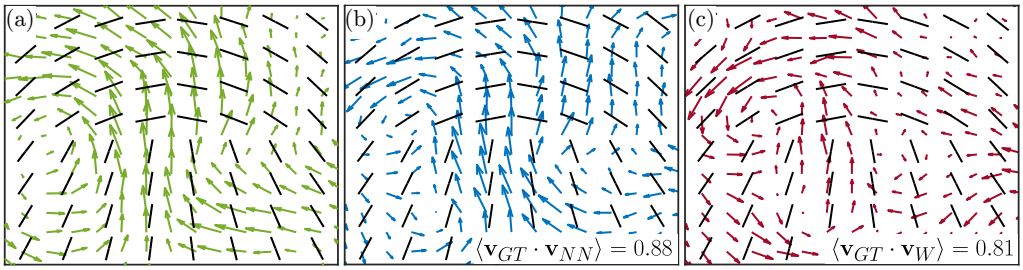

Figure 3.3: Average velocity fields around +1/2 defects for (a) manually labelled defects, (b) defects detected using the neural network and (c) defects detected using the winding number. The single point correlation function ($\langle \mathbf{v}_{GT} \cdot \mathbf{v}_{\square} \rangle$) between the ground truth (GT) field and the neural network (NN) and winding number (W) fields is also shown.

several thousand defects. While this was achievable in a numerical model, time and cost constraints could make the requirements of such vast amounts of data to understand the properties of these defects prohibitive in an experimental setting. Due to the difficulty in collecting experimental data, it is therefore crucial that defect properties can be discerned using a minimal amount of information.

The average velocity fields for manually labelled, winding number detected and CNN detected defects, using 150 +1/2 defects detected from the test data set, can be seen in Fig. 3.3. 150 defects were used as this was number of +1/2 defects manually labelled in the test data set and so the largest number we could use to compare the different methods. The manually labelled defects demonstrate the clearest tail-to-head, vortical flow fields characteristic of extensile systems [66]. The flow field around CNN detected defects clearly show better agreement with the manually labelled flow field than the flow field found using the winding number, reflected in the higher correlation between the two fields. The improvement between the two methods is even more stark when looking at the difference in velocity magnitudes between each method and the manually labelled flow field (Fig. 3.4). This illustrates the impact of the reduced performance, particularly the reduced precision, of the winding number and confirms the primacy of our model in detecting 'better' defects, as the anticipated mean-field behaviour is clearer.

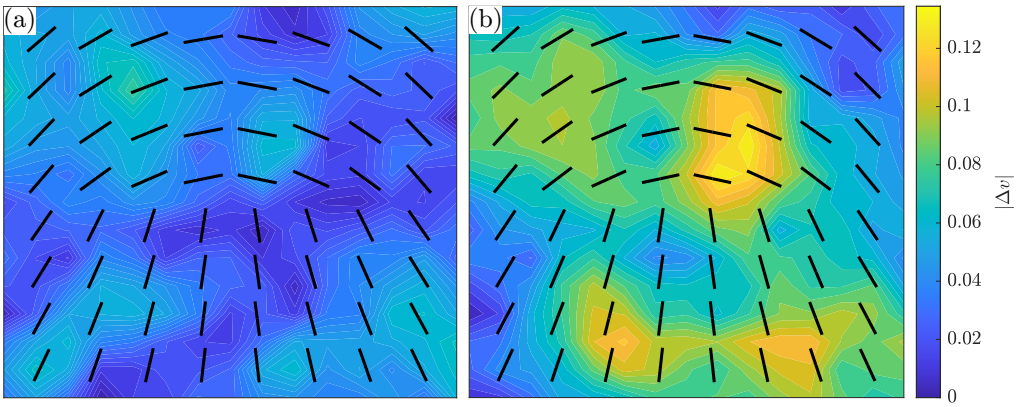

Figure 3.4: Difference in velocity magnitudes between average velocity fields for manually labelled defects and (a) defects detected using the neural network and (b) defects detected using the winding number.

Additionally, we compared the velocity field around defects detected using the CNN and defects detected on the same data using the 'on-lattice' winding number method used in the previous chapter (Fig. 3.5). The difference between the two is even starker than between our model and the off-lattice winding number method used in the present study. As well as highlighting the improvement using an off-lattice method can bring, it further underlines the benefits of our model compared to techniques used currently.

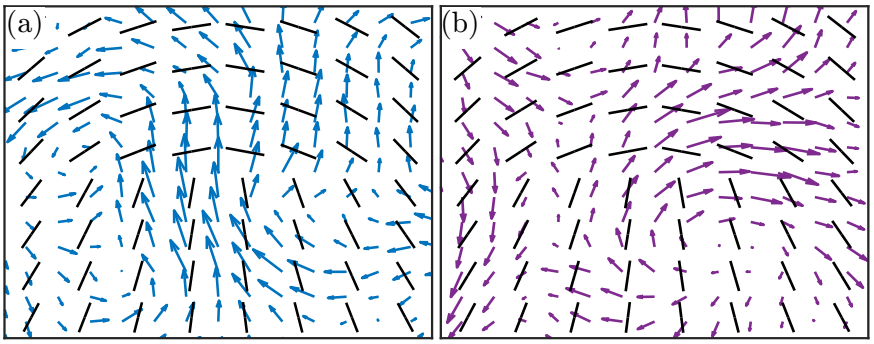

Figure 3.5: Mean tissue velocity fields around 150 +1/2 defects detected using (a) our CNN model and (b) the winding number at predefined points in the domain, used in Chapter 2.

3.3.3 Sensitivity to grid size

Defect detection techniques can often be sensitive to the window size used to detect them. While we choose our grid and window size to properly capture defects in our system, if our trained model is to be readily usable on experimental data, it should achieve accurate results over a range of window sizes. To investigate this, we assess the accuracy of our trained model and the winding number method in classifying the test data at different grid sizes. As our model takes as input a 9×9 grid of points, changing the grid size is akin to changing the ROI size. We do not retrain our model with inputs at the new grid size, we use the original model where the weights were trained on data interpolated to the original grid size.

To enable comparisons with our ground truth, for each ROI we take the coordinates of the centre and interpolate the cell data to a new grid size about this central point. We look at a range of grid sizes from $\Delta x = 0.1$, which gives an ROI with a window length approximately one cell across, to $\Delta x = 0.8$, meaning our interpolated grid is of the same order as the typical cell length and the ROI window lengths are approximately four times larger than the typical defect size. When smoothing the interpolated field, we scale the size of our sliding window such that the area over which we average is approximately constant.

The classification accuracy as a function of grid size can be seen in Fig. 3.6. With the exception of the smallest grid size, our CNN consistently outperforms the winding number. Our method is also less sensitive to the grid size than the winding number, whose performance drops sharply when the grid size varies from that which gives the highest accuracy, and is not much better than random selection when the grid size is greater than 0.5. The CNN, however, is able to maintain a level of accuracy greater than, or similar to, the winding number's best performance even when the ROI is approximately four times larger than the size of the defect ($\Delta x = 0.4$). This demonstrates the robustness of our approach and the ability of method to de-

tect defects even when the parameters of the model are not perfectly tuned to the system.

3.4 Discussion

Here we have developed a new method for detecting nematic defects in confluent tissues which, crucially, is readily implementable on experimental data. While there are several steps in pre-processing the input data to prepare it for the CNN, all that is required from users of the method is to input appropriately scaled cell coordinates and orientations. Our model can therefore aid in the expanding study of active nematic defects in biological systems [138]. Importantly, we demonstrate that our method displays superior performance to the current standard use of the winding number in detecting defects and in capturing the mean-field properties of these defects. This reduces the amount of data required to obtain these properties, potentially improving experimental data interpretation.

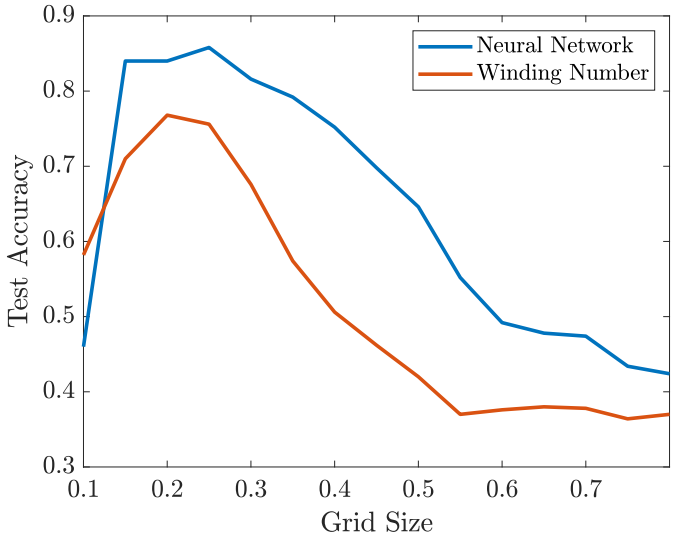

Figure 3.6: Classification accuracy vs. grid size for the CNN and the winding number method.

Interestingly, although the overall performance of our model is better, the winding number is slightly more sensitive to detecting defects. This means there could be applications where using the winding number would be more suitable, if the cost of missing a defect in the domain is very high. However, the improved performance in finding mean defect flow fields demonstrates that, in practice, the increase in overall performance of our model makes it more advantageous. This improved performance is likely due to the winding number only using information around the edge of the ROI, where as our CNN can take advantage of spatial information and correlations across the whole region.

In contrast to previous studies on using machine learning to detect nematic defects [119], our method is specifically designed for noisy experimental systems where the nematic field may not be well defined everywhere, and consequently low nematic order may not guarantee the presence of a defect. However, we anticipate our method will work well with any system whose nematic field can be easily interpolated to a 2D grid. Additionally, the approximate defect size must be known to properly scale the interpolation grid and, consequently the ROI window size. Our grid sensitivity study demonstrated that accuracy is maintained for window lengths between approximately $0.75w_D$ and $2w_D$, where w_D is the typical defect width, but outside of this range the accuracy drops off. If w_D can be approximated, the method developed here should be applicable to a variety of experimental systems.

Chapter 4

Interfacial dynamics in growing tissues

4.1 Introduction

4.1.1 Characterising interfacial dynamics

Many biological processes, from cancer metastasis to morphogenesis, rely on the integration of cell proliferation and collective cell movement. While cell proliferation is known to be regulated by the mechanical properties of the tissue [159], it is also becoming increasingly clear that proliferation alters the properties, and consequently the dynamics, of the tissue in return [109, 160, 161]. Whereas the forces generated during cell division events are well understood [9], our understanding of how these affect dynamics at the collective level is comparatively more limited [162]. This is due to the difficulty in determining how cellular scale processes manifest themselves as macroscopic dynamics.

A case in point is the dynamics of the interface of growing tissues. The tissue

boundary does not grow in an ordered manner, but rather a chaotic one, and it is unclear how cell division can produce such behaviour. Due to the chaotic dynamics, it is also unclear how to characterise the dynamics of the interface. Some studies describe the dynamics as governed by the onset of an instability of the tissue interface [14, 45, 46, 47], while others characterise the fluctuations as arising due to the intrinsic noise within the system.

If the latter approach is taken, the interface is characterised by calculating how the roughness of the interface, or interface width, scales in space and time. If the scaling for space and time can each be described by a single exponent, the values these exponents take can be used to deduce which universality class the interface growth belongs to [163]. A universality class is a collection of mathematical models that exhibit the same scaling behaviour as the system is viewed at larger and larger length-scales. In the context of interface growth, this allows one to write down a canonical equation describing the growth process, as this equation possesses the same scaling as that observed. This equation highlights the mechanisms governing interface dynamics.

However, interface growth in biological systems has been characterised in this manner experimentally [49, 50, 51, 52] and numerically [164, 165, 166, 167], and there is disagreement as to which universality class it belongs to. Scaling in agreement with the Kardar-Parisi-Zhang (KPZ) universality class has been observed [49, 164, 165, 166], which indicates the interface is governed by the KPZ equation, defined in one spatial and one growth dimension as

$$\partial_t h(y,t) = \gamma \partial_y^2 h(y,t) + \lambda [\partial_y h(y,t)]^2 + \eta, \tag{4.1}$$

where h is the interface height, the growth dimension, and y is the spatial dimension. The noise η is described by random Gaussian white noise of the type considered in Chapter 2. The other two terms indicate the processes controlling interfacial

dynamics. The first term on the RHS stems from surface tension and seeks to smooth out fluctuations in the interface. The second term arises as the lowest order term allowed by relaxing the enforcement of symmetry in fluctuations about the mean interface position (i.e. by no longer requiring the equation be invariant to the transformation $h \to -h$). This encodes lateral growth into the model, meaning the interface grows normal to its local orientation, and makes interface growth non-conservative, meaning it can grow by *adding* material to the interface.

As biological interfaces can grow either through non-conservative means via cell division, or by spreading laterally outwards via cell migration, one would generally expect these systems to belong to the KPZ universality class. However, scaling in accordance with the Edwards-Wilkinson (EW) universality class has been found for interfaces in active systems [168, 169]. This universality class is governed by the EW equation, which is similar to the Eq. (4.1) but with the nonlinear term excluded [163]. The exclusion of the nonlinear term enforces that interface growth be symmetric about the mean interface position, conserving overall interface length. This is unlikely given that there are clear non-conservative growth mechanisms generated by a proliferating, active material on one side of the interface and a void on the other. The appearance of EW scaling is therefore likely due to the difficulty simulating system sizes large enough to reach a regime where the effects of the nonlinearity can be observed.

However, surprisingly, scaling consistent with the linear molecular beam epitaxy (MBE) universality class has been reported [50, 51, 166]. This universality class, sometimes referred to as the Mullins-Herring (MH) universality class, is governed by the MH equation [170, 171]

$$\partial_t h(y,t) = -K\partial_y^4 h(y,t) + \eta, \tag{4.2}$$

where K is the surface diffusion coefficient. As the coefficient name suggests, the

term on the RHS in Eq. (4.2) indicates that growth processes in the MBE universality class are dominated by surface diffusion effects. Such scaling would suggest cell-cell junctions at the interface are weak, allowing cells to diffuse freely. The appearance of this scaling is surprising, as this growth process is conservative. However, it opens up the possibility of further growth equations describing the process, such as the one proposed by Villain, Lai and Das Sarma (VLDS) [172, 173]. Derived to model MBE at high temperatures, the VLDS equation involves an additional of the nonlinear correction $\partial_y^2(\partial_y h)^2$ to the MH equation. Although scaling consistent with this equation has not been reported in the literature, the reporting of scaling consistent with the MH equation means it could describe the growth processes at long enough length scales or if fluctuations are sufficiently large.

Additionally, scaling inconsistent with any known universality class has been seen [52, 174, 167]. As well as the difficulty modelling large enough systems, this debate on the correct scaling often stems from subtleties in the models used, such as heterogeneity in the surrounding environment [167], or the difficulty of using experimental data to perform the scaling analysis [175]. Nevertheless, taken together, these results indicate that the universality class of, and hence mechanisms governing, growing cellular interfaces is not settled.

Interfacial dynamics have also been described as being governed by the onset of an instability in a variety of scenarios, usually by analysing hydrodynamic models analytically. Active traction forces have been found to destabilise a spreading tissue front in the absence of proliferation [14, 45]. Coupling these motility forces to the tissue velocity field through alignment has also been shown to induce an instability in a stationary front [46, 47]. Introducing special *leader* cells with higher motility at the tissue front can also lead to fingering [176, 177], as can including a mechanochemical coupling [178]. Fingering instabilities have also been studied numerically, with particle-based studies reporting that motility forces can induce fingering in a

tissue in the absence of proliferation [179], in a similar manner to analytical models. Most of these studies focus on the role of motility in precipitating the instability, although tissue growth was also found to induce an instability at a boundary between two tissues [180, 181], or when a tissue is growing into another viscous medium [182, 183]. However, it has not been found to cause an instability in a tissue freely expanding, where the dynamics of any other medium can be ignored.

4.1.2 Modelling growing tissues

Models incorporating growth and cell proliferation are becoming increasingly prominent within active matter, and have been used to study a variety of phenomena. Cell-based simulations have shown how cell division affects the structure of, and fluidises, epithelial tissues [184, 185, 91, 186]. They have also delineated the effect of cell division on different macroscopic dynamics, such as on coherent angular motion in morphogenesis [187] and how the interplay of mechanical stresses and cell proliferation can drive fronts of growing cells [188]. However, due to the increase in computational complexity as the number of cells increase, cell based models are limited in the length-scale of system they can model, leading to a need for methods that can describe these growing systems in the hydrodynamic limit. At larger length-scales, continuum models have been employed to study growing bacterial colonies in two [56, 189] and three dimensions [190], while multiple studies have described growing biological systems in 2D using a hybrid lattice-Boltzmann method (LBM) [34, 191, 109].

While LBMs offer an incredibly efficient means of modelling growing systems, previous LBM studies of active systems have either used periodic domains in which the entire system is active, or have described the boundary of the active material using a phase separating system with a phase field [109]. These approaches are valid if the phenomena under study relate to behaviour in the bulk or if the system is not

completely phase separated, i.e. the 'vapour' phase has a non-vanishing, albeit low, density. However, they are not appropriate in systems with well-defined boundaries and areas completely devoid of cells, such as expanding tissue layers or densely packed bacterial biofilms. In such systems, properly capturing this separation is important for describing the dynamics of the boundary, and the biological processes that depend on this, such as wound healing [2].

In this chapter, we address this issue by introducing a novel LBM for growing biological tissues capable of describing faithfully the dynamics of growing fronts. Crucially, our method for modelling the interface of our tissue ensures there is no low density vapour phase and our tissue has a sharp edge. Using this model, we study the dynamics and stability of the growth front. We find that the interface of a tissue growing due to bulk driven cell proliferation pertains to the KPZ universality class. We then consider tissue growth with a density dependent proliferation regime where proliferation occurs around the growing front, where we again find KPZ scaling in the interface width for small system sizes. However, we also find a previously unreported mechanical instability at larger system sizes, which we explain by performing linear stability analysis on a minimal model for the front.

We first introduce our novel LBM for a growing system with a fluctuating interface. We then charactise the scaling behaviour of the interface using a bulk driven growth regime, followed by studying interface fluctuations using a density dependent growth regime. We then examine the emergent instability and how it forms.

4.2 Lattice-Boltzmann method

4.2.1 A lattice-Boltzmann method for a dry active fluid

As the starting point for our present model we take a recently developed LBM for a dry active fluid system [106]. The efficiency of the LBM stems from solving, instead of the hydrodynamic EOM, a simplified system that obeys the same hydrodynamic symmetries as the real system, leading to identical behaviour in the hydrodynamic limit [104, 192]. This simplified system describes the dynamics of a distribution function $f(t, \mathbf{r}, \boldsymbol{\zeta})$, which represents the distribution of mass at time t and position $\mathbf{r}$, moving with velocity $\boldsymbol{\zeta}$. From f the hydrodynamic variables of interest can then be found

$$\rho(t, \mathbf{r}) = \int \mathrm{d}^{\mathrm{D}}\boldsymbol{\zeta} f(t, \mathbf{r}, \boldsymbol{\zeta}), \quad \rho(t, \mathbf{r})\mathbf{v}(t, \mathbf{r}) = \int \mathrm{d}^{\mathrm{D}}\boldsymbol{\zeta} f(t, \mathbf{r}, \boldsymbol{\zeta})\boldsymbol{\zeta} \ , \tag{4.3}$$

where D is the spatial dimension. We map this continuous distribution function onto a lattice by discretising $\boldsymbol{\zeta}$ into a finite number of velocity vectors $c\mathbf{e}_i$. This means we can describe the dynamics of f using the discretised Boltzmann equation

$$\partial_t f_i + c\mathbf{e}_i \cdot \nabla f_i(t, \mathbf{r}) = \Omega_i \ , \tag{4.4}$$

where f_i is the mass density moving with velocity $c\mathbf{e}_i$ and Ω_i is a collision operator that ensures matter in our system interacts while obeying the same symmetries as the system we wish to mode.

We simulate Eq. (4.4) on a 2D triangular lattice (Fig. 4.1a), termed D2Q7 in standard LBM notation, meaning mass moves along lattice vectors $\mathbf{e}_i = \cos[(i-1)\pi/6]\hat{\mathbf{x}} + \sin[(i-1)\pi/6]\hat{\mathbf{y}}$ for $i \in \{1, 2, ...6\}$ and $\mathbf{e}_0 = 0$ corresponding to mass which is at rest. The lattice speed c is the ratio of our grid spacing Δx to time-step Δt, which we choose to be 1. The hydrodynamic variables of interest, cell density ρ and velocity

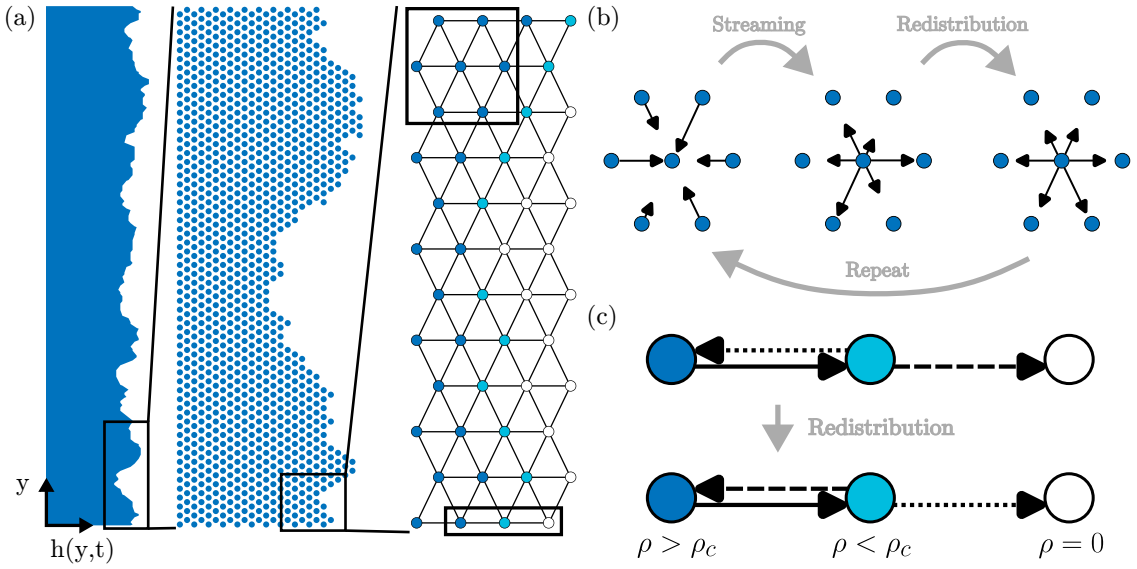

Figure 4.1: A LBM for a growing biological system. (a) We discretise our system (left) onto a hexagonal lattice (middle), with each lattice point representing a number of cells. There is a growing front beyond which the distribution function f_i is zero in all lattice directions, (white sites in right). (b) Each time-step is subdivided into a streaming step and redistribution step. In the streaming step, f_i is advanced by one time-step to get an intermediate distribution f_i^*. A steady-state distribution f_i^{ss} is then calculated using f_i^* and f_i is redistributed such that it relaxes towards f_i^{ss}. (c) The growing periphery is enforced using a 'bounce-back' condition during the redistribution step. When the density at a site is below a critical density ρ_c, instead of relaxing f_i towards the steady state distribution f_i^{ss}, the directions of the distribution function are reversed such that the mass that would next stream to an empty site is now bounced back in the opposite direction (dashed arrow). The mass just streamed from an empty site, which would be zero, is then set to stream back out instead (dotted arrow).

$\mathbf{v}$ can then be calculated from f_i using

$$\rho(t,\mathbf{r}) = \sum_{i=0}^{6} f_i(t,\mathbf{r})\,,\ \mathbf{v}(t,\mathbf{r}) = \frac{\sum_{i=0}^{6} f_i(t,\mathbf{r})\, c\mathbf{e}_i}{\rho(t,\mathbf{r})}\ . \tag{4.5}$$

We then evolve the discretised Boltzmann equation using the Bhatnagar-Gross-Krook collision operator [193] with additional fluctuations η_i, meaning f_i evolves according to:

$$f_i(t+\Delta t, \mathbf{r}+c\mathbf{e}_i\Delta t) = f_i(t,\mathbf{r}) - \frac{1}{\tau}\left[f_i(t,\mathbf{r}) - f_i^{SS}(t,\mathbf{r})\right] + \eta_i(t,\mathbf{r})\ , \tag{4.6}$$

where τ is a relaxation parameter, η_i are random fluctuations and f_i^{SS} is a steady state distribution which respects the same symmetries as our system, meaning our system obeys the correct symmetries as it relaxes towards f_i^{SS}. While 'steady state' implies a quantity that does not change, f_i^{SS} refers to the distribution function the system would have were it in steady state given the current density and velocity fields, and so it changes as these quantities change. We define f_i^{SS} as

$$f_i^{SS} = w_i \rho \left(1 + 4\frac{\mathbf{e}_i \cdot \mathbf{v}^*}{c} + 8\frac{(\mathbf{e}_i \cdot \mathbf{v}^*)^2}{c^2} - 2\frac{|\mathbf{v}^*|^2}{c^2} \right) , \tag{4.7}$$

where w_i are lattice direction weights, with $w_0 = 1/2$ and $w_{i\neq 0} = 1/12$, and $\mathbf{v}^*$ is our steady-state velocity that depends on the system we are modelling. We define f_i^{SS} in this way because, if $\mathbf{v}^* = \mathbf{v}$, Eq. (4.7) would be the equilibrium distribution used to model passive fluids in 2D with a triangular lattice, as it conserves mass and momentum [192]. However, as active systems do not require the conservation of momentum, we can choose $\mathbf{v}^*$ to be any function of $\mathbf{v}$ and ρ that respects the symmetries of the system of interest. As our focus here is to study the effects of proliferation, here we choose $\mathbf{v}^* = (1-\mu)\mathbf{v}$, where μ encodes dissipation arising from friction with the substrate, although different forms of $\mathbf{v}^*$ can be used to model active self-propulsion [106]. As we have defined it, Eq. (4.6) always conserves mass regardless of our choice of $\mathbf{v}^*$, which is obviously not the case in a growing system. However, choosing f_i^{SS} so as to conserve mass allows easier control over precisely how mass is added to our system and so how cell proliferation is modelled.

The fluctuations η_i in Eq. (4.6) are defined as

$$\eta_i(t, \mathbf{r}) = \tilde{\eta}_i(t, \mathbf{r}) - \frac{1}{7}\sum_{i=0}^{6} \tilde{\eta}_i(t, \mathbf{r}) , \tag{4.8}$$

where $\tilde{\eta}_i$ is an uncorrelated random variable that is uniformly distributed between $[-\sigma, \sigma]$. This form of noise is chosen so as to conserve mass, for reasons discussed

previously.

We evolve Eq. (4.6) in two steps: a streaming step and a redistribution step (Fig. 4.1b). In the streaming step f_i is evolved by one time-step to give an intermediate distribution $f_i^*(t + \Delta t, \mathbf{r} + c\mathbf{e}_i\Delta t) = f_i$. In the redistribution step, f_i^{SS} is then calculated at each point by calculating the hydrodynamic variables based on f_i^*. We then relax f_i^* towards f_i^{SS} using Eq. (4.6) by replacing $f_i(t, \mathbf{r})$ with $f_i^*(t + \Delta t, \mathbf{r} + c\mathbf{e}_i\Delta t)$ on the right hand side. Fluctuations η_i are then added to give the final distribution at the next time-step $f_i(t + \Delta t, \mathbf{r}c\mathbf{e}_i\Delta t)$.

4.2.2 Incorporating cell proliferation and the tissue boundary

From this model, we incorporate both cell proliferation and a growing tissue boundary. To model cell proliferation, in-between the streaming and redistribution steps, we add mass at a chosen a site by increasing f_i of two opposite lattice vectors, for example f_1 and f_4, by $\rho_{\text{cell}}/2$. Here ρ_{cell} corresponds to the mass of one cell. The direction in which mass is injected is chosen at random and replicates the extensile nematic nature of cell division [109]. We determine the number of sites at which we inject mass by setting growth to be at a constant rate g. The number of sites to be randomly selected is then $n_s = g\, m_{\text{tot}}/\rho_{\text{cell}}$, where m_{tot} is the total cell mass, found by summing ρ over all lattice points. Proliferation sites are then selected, with replacement, at random until enough mass has been added to the system. Time or position dependant proliferation rates can then be implemented depending on the probability distribution from which proliferation sites are selected.

Here, we look at two growth regimes. Initially, we select proliferation sites from a uniform distribution, meaning proliferation in the active portion of our tissue is equally likely in any occupied site in the bulk or at the interface, meaning the

majority occurs in the bulk. We use the phrase 'active portion' because, as the tissue grows and the interface advances, we advance the rear wall of the model with it. This greatly improves efficiency and reflects the fact that biological tissues typically have a section near to the boundary that is actively proliferating, with cells far from the boundary becoming quiescent. Secondly, we implement a more biologically relevant growth regime where the local proliferation rate is dependent on the local density in the system, which concentrates proliferation to the interfacial region. This is motivated by increased cell density causing increases in tissue pressure away from the tissue boundary, [79], which can inhibit cell proliferation [38]. Now, when a lattice site is randomly selected, cell division occurs with probability $p_{\text{div}}(\mathbf{r})$, which decays linearly with the local density according to

$$p_{\text{div}}(\mathbf{r}) = \begin{cases} 1 - \rho(\mathbf{r})/\rho_0 \ , & \text{if } \rho(\mathbf{r}) > \rho_c \\ 0 & \text{otherwise} \end{cases} \tag{4.9}$$

where ρ_0 the critical density above which proliferation ceases. This regime models a scenario where crowding suppresses proliferation due to increased compressive stresses, such as in epithelial layers [194], meaning the bulk of the tissue becomes quiescent.

While growth in the form of mass injection can be readily implemented within the LBM framework, a key difficulty in applying it to a growing system is how the interfacial dynamics should be captured. Here, our key innovation is to use a two step thresholding method to accomplish this task. Specifically, our method ensures that the 'vapor' phase is completely devoid of any mass, which also distinguishes our method from existing LBM applied to phase separating systems. This allows the proper modelling of the tissue layers boundaries using a LBM for the first time.

We achieve this by developing a type of freely moving bounce-back method. In the redistribution step, if the density at a given site is below a threshold value ρ_c,

instead of relaxing towards f_i^{SS}, the directions of f_i^* are reversed such that $f_i^* = f_j^*$ where $\mathbf{e}_j$ is the reverse direction of $\mathbf{e}_i$ ($1 \leftrightarrow 4, 2 \leftrightarrow 5, 3 \leftrightarrow 6$). This means the mass just streamed to a given node in the stream step is reflected such that it now travels back in the direction it came from (Fig. 4.1c). This ensures that any mass that would be streamed 'out' of the system in the next time-step is rebounded back in and the lattice site it would be streamed to remains empty. This ensures that at the edge of the tissue there is one lattice site with $\rho < \rho_c$ and beyond this the system is devoid of mass. This mimics a surface tension like force and allows our LBM to easily model sharp interfaces such as an epithelial tissue edge.

4.2.3 Implementation details and algorithm

We implement our LBM on rectangular domains with periodic boundary conditions at the top and bottom boundaries, and a bounce-back condition at the rear wall. We initialise our system by setting the initial velocity field to zero everywhere and generating an initial density distribution with a flat interface, centered around some initial average density ρ_{init}, uniformly distributed on $[0.9\rho_{\text{init}}, 1.1\rho_{\text{init}}]$. From these initial distributions we calculate an initial f_i^{SS}, which we set as our initial f_i.

The algorithm then proceeds in the following steps:

1. Streaming step to generate intermediate distribution $f_i^*(t+\Delta t, \mathbf{r}+c\mathbf{e}_i\Delta t) = f_i$.
2. Calculate ρ and $\mathbf{v}$ from f_i^*.
3. Add mass from cell proliferation.
4. Calculate $\mathbf{v}^*$ and hence f_i^{SS}.
5. Redistribution step:
    - If $\rho(\mathbf{r}) \geq \rho_c$: redistribute $f_i = f_i^* - \left[f_i^* - f_i^{SS} \right] / \tau$.

- If $\rho(\mathbf{r}) < \rho_c$: for $i > 0$, set $f_i = f_j$ where $\mathbf{e}_j$ is the reverse direction of $\mathbf{e}_i$ ($1 \leftrightarrow 4, 2 \leftrightarrow 5, 3 \leftrightarrow 6$).

6. Add noise: $f_i \to f_i + \eta_i$, provided $\rho > \rho_c$.

7. Correct any negative values of f_i that arise from adding noise:

   - If $f_0 < 0$: set $f_0 = 0$. This will change the density, so rescale each direction according to $f_i \to \rho f_i / \Sigma_j f_j$.
   - If $f_i < 0$ for $i > 0$: Set $f_j = f_j + |f_i|$ where $\mathbf{e}_j$ is the reverse direction of $\mathbf{e}_i$ ($1 \leftrightarrow 4, 2 \leftrightarrow 5, 3 \leftrightarrow 6$) and set $f_i = 0$.

As our tissue grows we advance the rear wall such that it is always at least $\max(50, 10w)$ lattice units behind $\bar{h}$. We use system parameters $\Delta x = 1$, $\Delta t = 1$, $\rho_c = 0.05$, $\tau = 1$, $\rho_{\text{init}} = 0.1$, $\sigma = 0.01$, $\mu = 0.001$, $g = 0.001$ and $\rho_{\text{cell}} = 0.01$. For the density dependent growth regime we use $\rho_0 = 0.15$.

4.3 Bulk driven growth

We initially investigate a regime where proliferation is taken to happen uniformly across the active portion of the tissue, meaning the majority of it occurs in the bulk. To examine how the interface evolves, we calculate the interface width w, defined as the standard deviation of the interface height $h(y, t)$

$$w(t) = \sqrt{\frac{1}{L} \int_0^L \left[h(y,t) - \bar{h}(t) \right]^2 \mathrm{d}y} \,, \tag{4.10}$$

where L is the width of the domain. How the interface scales in time and space can be completely described by two scaling exponents α and β. The growth exponent β describes how w grows before it reaches its steady-state, saturation value w_∞ at time t_∞, that is $w \sim t^\beta$ ($t \ll t_\infty$). The roughness exponent α describes how w_∞

scales with the system size L, $w_{sat} \sim L^{\alpha}$ ($t \gg t_{\infty}$). The time for the system to reach steady-state then scales according to the dynamic exponent $z = \alpha/\beta$, meaning $t_{\infty} \sim L^{z}$. For KPZ scaling one would expect $\alpha = 1/2$ and $\beta = 1/3$, leading to $z = 3/2$, whereas scaling consistent with MBE would give $\alpha = 3/2$ and $\beta = 3/8$, leading to $z = 4$.

We implement our LBM on rectangular domains of different widths L. Fig. 4.2a shows the time evolution of w for different system sizes, showing, as anticipated, that each systems interface grows at the same rate but that larger systems permit rougher interfaces. Upon rescaling w and t by the appropriate KPZ exponents, $L^{1/2}$ and $L^{3/2}$ respectively, we find a very good curve collapse, indicating the system is exhibiting KPZ scaling (Fig. 4.2b). This is underlined in Fig. 4.2c and d, which show the appropriate scaling of w_{∞} and t_{∞} with L.

4.4 Density dependent growth

4.4.1 Interface growth

We now implement a more realistic scenario, where proliferation concentrated towards the boundary of the system. We do this by implementing a density dependent growth regime following Eq. (4.9), keeping other parameters the same. Upon studying the growth of the interface in this regime, we again see KPZ scaling for systems with $L < 640$, however, for larger system sizes KPZ scaling is not observed and the interface width appears to diverge (Fig. 4.3a).

To investigate the cause of this divergence, we plot the steady-state profile of the boundary for systems of different sizes (Fig. 4.3b). Surprisingly, upon doing this we see that, for sufficiently large L, the interface is subject to a system-spanning mechanical instability, at the largest wavelength permitted by the system. To gain

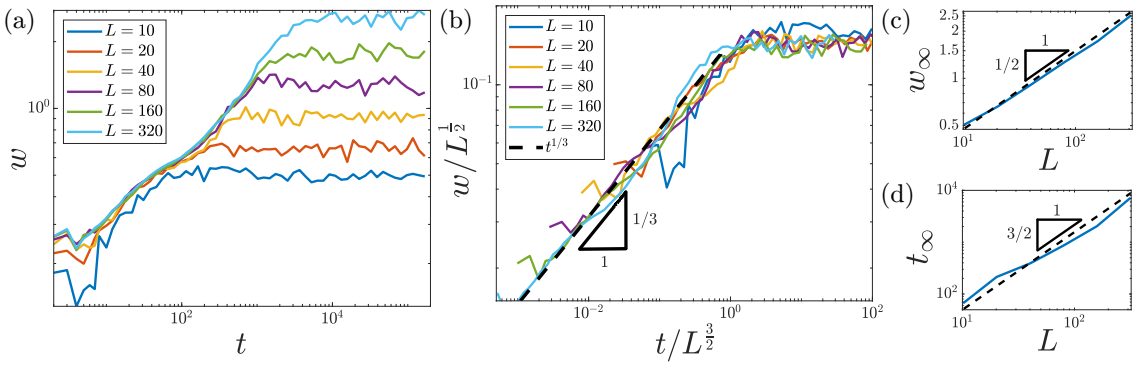

Figure 4.2: Bulk driven growth exhibits KPZ scaling. (a) Time evolution of the interface width w for systems of different length L. (b) Curves collapse when rescaled by KPZ exponents. The dashed line showing scaling $t^{1/3}$ highlights the corresponding KPZ growth exponent. KPZ scaling of (c) w_∞ and (d) t_∞ with L. The dashed line is a guide showing KPZ scaling for (c) the roughness exponent α, $w_\infty \sim L^{1/2}$ and (d) the dynamic exponent z, $t_\infty \sim L^{3/2}$. All results are averaged over 30 independent simulations.

an insight into the cause of the instability, we studied proliferation in the tissue in the area around the most advanced ($h_{\max}$) and least advanced ($h_{\min}$) positions of the interface. We define these areas as rectangular regions extending 10 lattice sites above and below $h_{\max}$ or $h_{\min}$, and 20 lattice sites into the bulk. We find that, for larger system sizes, there were more proliferation events around $h_{\max}$ than $h_{\min}$, although this bias was not seen for smaller system sizes (Fig. 4.3c). This led us to hypothesise that a local increase in the proliferation rate around protrusions to the interface could lead to an increase in the local interface velocity, thus driving the instability (Fig. 4.3c, inset). To understand the mechanism driving the instability further we now develop a minimal model of interface growth in our system.

4.4.2 Linear stability analysis

The mechanism driving the instability is unclear as, while cell proliferation has been found to induce an instability at the tissue boundary when it is growing into another viscous medium [180, 182, 183, 181], an instability arising from a purely proliferative

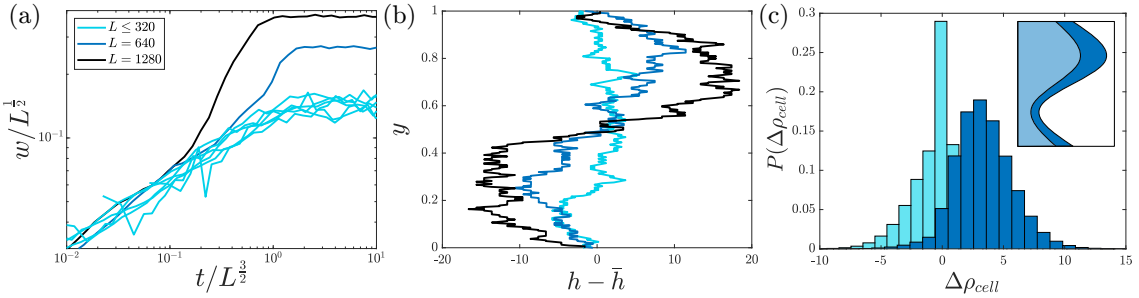

Figure 4.3: A system spanning instability causes divergence from KPZ scaling. (a) Interface growth curves for systems with $L < 320$ collapse when rescaled by KPZ exponents, but diverge for $L > 320$. (b) Examples of steady-state profiles of the interface position h shifted by the average interface position $\bar{h}$ for systems with $L = 320$ (light blue), $L = 640$ (dark blue) and $L = 1280$ (black). (c) Probability distributions for the difference between the number of cell divisions $\Delta\rho_{\text{cell}}$ around h_{max} and h_{min} for $L = 40$ (light blue) and $L = 640$ (dark blue). (inset) Schematic of the proposed instability mechanism, proliferative regions are shown in dark blue. The more advanced sections of the interface are more proliferative. All results are averaged over 30 independent simulations.

system expanding into a void has not been reported in the literature. To illustrate the mechanism at play, we write down an EOM for the interface position h. Our numerical results suggest that for the instability to occur we require the growth rate of the interface to increase as we move from h_{min} to h_{max}, and so depend on h.

This can be understood by considering what happens when the boundary locally advances. Any local increase in h will necessarily have a lower density than the area preceding it and so a higher likelihood of cell division. Due to friction, and the limits on how quickly information can propagate in the system, the effect of these changes in density can only propagate back into the bulk at a finite speed. Consequently, if the timescale for cell proliferation is shorter than that of this propagation, areas where the interface is more advanced grow faster. Along with this, surface tension, coming from the bounceback condition in our LBM, also clearly has an effect on interface dynamics. The dynamics of h can thus, to lowest order, be described by

$$\partial_t h(y,t) = kh(y,t) + \gamma \partial_y^2 h(y,t) \ , \tag{4.11}$$

where k is the growth rate and γ the surface tension. While this is obviously a very simple, minimal model for our interfacial dynamics, it is the simplest means of introducing the proliferation difference between the peak and trough into an analytical model. We note that this equation is far more general than our LBM and applies to any system in which the growth rate of the interface depends on its position.

Introducing growth in this way allows us to illustrate the instability mechanism as, by adding a small amplitude perturbation of the form $\delta h = h_0 e^{\omega t + iqy}$, where $|\delta h| \ll 1$ and ω describes the growth rate of each wave number q, to a flat interface in a frame of reference comoving with the mean interface height, yields the dispersion relation

$$\omega(q) = k - \gamma q^2 \ , \tag{4.12}$$

which can be seen in Fig. 4.4.

From Fig. 4.4 it is clear that the fastest growing mode will always be the largest one permitted by the system, the system size, and that the growth rate can be

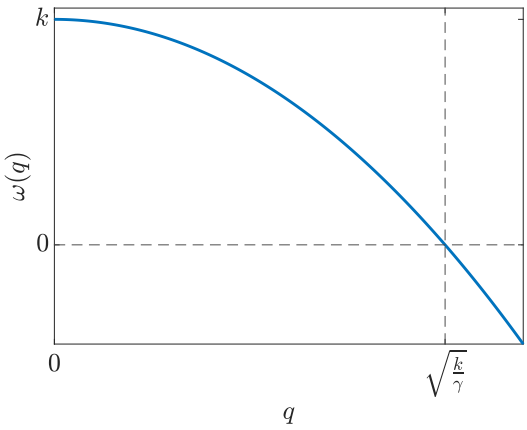

Figure 4.4: Growth rate of perturbations of different wave numbers. Perturbations only become unstable at wave numbers $q < \sqrt{k/\gamma}$, corresponding to lengths $L > \sqrt{\gamma/k}$. Beyond this threshold, the fastest growing mode is always the longest wavelength permitted by the system.

positive if wave numbers less than $\sqrt{k/\gamma}$ are permitted, corresponding to system sizes $L > \sqrt{\gamma/k}$. This is why the instability is only seen at sufficiently large system sizes, as the system only becomes unstable at a critical length $L_c = \sqrt{\gamma/k}$. However, we note that L_c is dependent on system parameters and so may not be very large if the growth rate is sufficiently fast or the surface tension weak.

To demonstrate this instability mechanism, we implement a different growth regime while keeping the overall growth rate constant. We restrict growth to being in the first 30 columns of lattice sites from the rear wall, but uniform within this region, such that width of proliferating tissue is constant. We do this in a system of size $L = 640$, where the instability was previously observed. While the biological plausibility of this scenario is debatable, introducing this type of growth removes the purported instability mechanism as the width of proliferating region is constant across the entire domain length L and so independent of the interface position. As can be seen in Fig. 4.5, introducing this growth regime eliminates the instability. These results suggest that *any* growing system where the number of constituents that are able to proliferate increases locally where the interface advances could be susceptible to this system spanning instability.

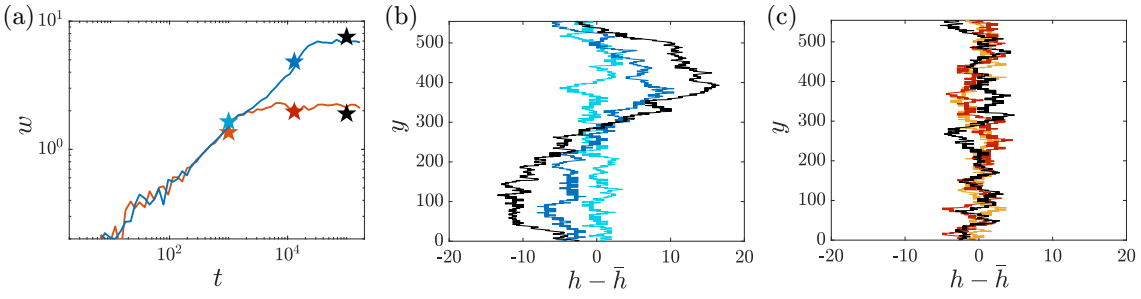

Figure 4.5: Restricting proliferation to the bulk removes the instability. (a) Time evolution of w when proliferation is (blue) density dependent and (orange) permitted only in the bulk. Stars indicate times at when profiles of the same colour are depicted in b and c.Time evolution of the interface position h shifted by the average interface position $\bar{h}$ for a system of size $L = 640$ with (a) density dependent proliferation and (b) proliferation restricted to the bulk, away from the interface. Darker colours indicate later times.

4.5 Discussion

In this chapter, we present a novel LBM for modelling growing, active systems. Our bounce-back method for the interfacial dynamics ensures well-defined, freely moving boundaries that allow for the proper physics of growing tissues to be captured using a LBM. Using this model, we demonstrate that the growth of the boundary driven purely by proliferation displays KPZ-like scaling, but also displays an instability in a physiologically relevant proliferation regime where proliferation is concentrated at the boundary. We formulate an analytical theory to demonstrate this instability arises due to a proliferation rate dependant on the position of the interface. This theory is more general than the specific model in which we observed the instability, and asserts that any system where the local growth rate is dependent on the interface position will be susceptible to this instability. These findings demonstrate the efficacy of using this LBM, as its mesoscopic scale and efficiency made it possible to simulate large enough systems to observe this instability and allow us to clearly exhibit KPZ scaling.

The results presented here are for a single value of the friction coefficient μ, although our results do not qualitatively change over a range of μ values. However, we note that for very high values of μ the system appears to undergo a roughening transition, where the steady-state interface width becomes independent of the system size L. Roughening transitions are known to occur when fluctuations at the interface of a given system are sufficiently suppressed [163]. However, due to the suppressed fluctuations, the interface in this regime is very ordered and flat and it it most likely not a physically relevant regime.

Obtaining KPZ scaling at small system sizes suggests that, if stable, growing tissue interfaces belong to the KPZ universality class. This emphasises that lateral growth and surface tension effects control the dynamics of the interface. This is in contrast

to the MBE scaling found previously [50, 51], that would indicate surface diffusion is controlling the process. The generality of our LBM adds further weight to this finding as it suggests that all systems that obey the same symmetries as those in our model exhibit KPZ scaling.

The onset of an instability at larger sizes is unexpected, as an instability arising from a purely proliferative system freely expanding into a void has not previously been reported in the literature. This highlights that proliferation should be considered along with motility in studies examining the stability of tissue interfaces. The role of motility has been studied in depth, while its interplay with growth has been less explored in theoretical investigations. The appearance of this instability suggests the tissue boundary in experimental systems may be susceptible to a fingering instability. However, as the most unstable mode in our model is the largest permitted by the system, this would suggest the typical size of the fingers seen would be of the order of the size of the system, which is not the case experimentally. This could be due to experimental systems not being large enough to be in the unstable regime. However, as we formulated our LBM through considering the symmetries of the system, it is difficult to link parameters in the LBM to parameters in experimental systems and obtain a value for the typical length-scale at which we expect the instability to occur experimentally. Nevertheless, as this instability is not seen experimentally, this study indicates that the chaotic dynamics seen in experimental wound healing assays could be governed by fluctuations that scale according to the KPZ universality class.

Chapter 5

Conclusions

5.1 Summary of Results

Confluent tissue layers are ubiquitous throughout our bodies, from endothelial cells lining the inner surface of blood vessels [27], to epithelial layers lining our intestines [195], kidneys [29] and lungs [22]. Their dynamics play crucial roles in many biological process, yet often these dynamics, and many of the phenomena contingent upon them, are poorly understood. In this thesis we have sought to characterise confluent tissue dynamics and understand how they emerge from the microscopic behaviour of constituent cells. Due to the different interactions involved in these different phenomena, and different length-scales at which they occur, they cannot be studied simultaneously. Here we have focussed on nematic collective behaviour, and nematic defects that arise as a result of this, as well as the dynamics of the boundary of a growing tissue. We have done this using physical theories, employing tools from the emerging field of active matter physics, in an effort to strip away complexity from these systems and pinpoint the underlying physical mechanisms behind these processes.

In Chapter 2 we investigated the cause of the extensile nematic behaviour recently observed in epithelial tissues [29]. This has attracted much recent interest due to the biological process extensile $+1/2$ defects were found to control, cell extrusion, but also because epithelial cells generate contractile nematic forces, with how the behaviour transitions to extensile at the tissue level being unclear. Thus far this behaviour has been largely understood through the emerging paradigm of characterising biological systems as active nematic systems [86, 85]. However, epithelial layers do not possess the typical ingredients of an active nematic material as they are not rod-shaped and display polar motility.

Due to this, we focussed on the role of polar forces and showed, through hydrodynamic modelling of solid and fluid tissues, that fluctuating polar traction forces arising from cell-substrate interactions manifest in extensile behaviour in the nematic field. When polar fluctuations are included along with fluctuating active cellular contractility, we find that both extensile and contractile behaviour is possible depending on which type of active fluctuations dominate over the other. Extensile behaviour, therefore, is still possible in the presence of contractile nematic forces. We then illustrated our findings by examining the dynamics of $+1/2$ defects in an active vertex model (AVM) with purely polar active forces, where exclusively extensile behaviour was seen. This numerical work also allowed us to show the equivalence between this widely used method for determining the nature of nematic behaviour and the method used in our analytical findings, in which we calculated the correlation $\langle \mathbf{v} \cdot (\nabla \cdot \mathbf{Q}) \rangle$, as we could also calculate the correlation numerically. Our motivation for describing the nematic behaviour using this correlation stemmed most studies characterising systems as extensile or contractile by the sign of the activity coefficient α in the active nematic term $\alpha \cdot (\nabla \cdot \mathbf{Q})$. Determining the sign of the correlation allows one to ascertain the nature of the nematic field under the systems dynamics even in the absence of explicitly nematic active forces.

There are several important implications that result from our findings. The first is the key role cell-substrate interactions play in governing the collective nematic behaviour. Previous studies have focussed on the role of cell-cell interactions in controlling collective behaviour [85, 20, 86], with our work highlighting that key features of the system are missed if cell-substrate interactions are neglected. Secondly, our findings highlight the vital role fluctuations play in dictating the collective behaviour of the system, which many studies on active nematics neglect to include. Additionally, characterising nematic behaviour using the correlation $\langle \mathbf{v} \cdot (\nabla \cdot \mathbf{Q}) \rangle$ represents a new perspective for viewing active nematic systems, as this incorporates the effects of fluctuations and allows a more complete picture of the systems dynamics to be gained. Finally, due to the use of a hydrodynamic model, this result is far more general in its application than just epithelial tissues, suggesting polar fluctuations driving nematic behaviour in any disordered system of elongated or deformable constituents. For example, it could explain the extensile nematic behaviour seen in system of vibrated rods [146].

During our investigation in Chapter 2, it became clear that current defect detection techniques in confluent tissues are inefficient and require large amounts of data to properly analyse defects in the system. While it was possible to collect this data in our numerical model, this may not be the case in experimental studies, where data is much more costly to collect. Moreover, this emergent behaviour is much harder to characterise if it cannot be reliably identified.

This type of identification task, where effective theoretical approaches are lacking, is well suited to machine learning methods, specifically convolutional neural networks (CNNs). Due to this, we developed a CNN to detect nematic defects in confluent tissues. Upon identifying regions of low orientational order, our method classifies these regions as containing no defect, a $+1/2$ defect or a $-1/2$ defect. In contrast to other studies [119], including a third category for the region not contain-

ing a defect accounts for the nematic field in confluent cell layers often being poorly defined, with a region of low orientational order not necessarily meaning a defect is present like it does in other systems. Upon training our model using manually labelled data collected from an AVM, we demonstrated that our CNN outperforms current detection methods. This led to improvements in determining the properties of defects, and therefore the collective behaviour, in the tissue. This has the potential to improve the analysis of experimental data, obtaining tissue properties in noisy environments where the average signal may be very weak. Additionally, although our focus here has been on confluent tissues, our method is readily implementable on any system which can be reliably cast in the form of the inputs to our model: where each constituent is described by a single x and y coordinate, as well as an orientation.

In Chapter 4 we studied the dynamics of the boundary of a growing tissue interface. This phenomena has been widely studied due to its relevance to wound healing, however, the role of growth is often ignored at the expense of traction forces and collective migration. In addition to a lack of understanding of how proliferation manifests in the macroscopic dynamics of the boundary, it also is unclear exactly how the dynamics of the boundary should be described. The dynamics have been characterised by determining conditions dictating the stability of the interface [14, 45, 46, 47], although it is not clear from experiments whether an instability is present or if the fluctuations of the interface are merely the result of intrinsic noise within the system [164, 165, 166, 167].

We aimed to clarify these points by studying a growing tissue using a novel lattice-Boltzmann method (LBM) that incorporates a sharp boundary akin to what is found in epithelial tissues. To focus on the role of cell proliferation, this is the only activity we included in our model. We find that, for sufficiently small systems, the interface is stable and fluctuations grow according to the Kardar-Parisi-Zhang (KPZ)

universality class. However, for larger systems, where proliferation is dependent on the local density in the tissue, the system becomes unstable and a system-spanning instability governs the dynamics of the interface. Through a minimal analytical model we demonstrate that the instability arises due to a coupling between the area of tissue actively proliferating and the position of the interface.

Our study indicates that, in the absence of motility and if growth is sufficiently slow, tissue interface growth is stable and belongs to the KPZ universality class. While KPZ scaling has been found before in particle based models [164, 165, 166], obtaining it using our LBM allows a broader conclusion about tissue behaviour to be drawn, as the model is based on the symmetries of confluent tissues, as opposed to a particular incarnation of them. It also highlights that growth can cause the interface to become unstable and begs the question as to whether this should be included more widely along with motility when the stability of the interface is characterised. Further, as we found the system becomes unstable, but only above some critical length, it remains unclear whether edge dynamics seen in experiments are unstable or merely a result of system noise. Finally, this work demonstrates the efficacy of our LBM to model growing tissues and properly capture the dynamics of the interface, as its mesoscopic scale and efficiency made it possible, for the parameter regime we used, to simulate large enough systems to observe KPZ scaling and the instability.

5.2 Future Work

The different findings in this thesis raise numerous questions and directions for further research. Our work on extensile nematic collective behaviour focussed on the disordered regime, however, epithelial layers can collectively migrate with a non-zero mean velocity. Although the dynamics here are clearly dominated by polar forces, it would be interesting to examine the effect this has on the behaviour of

the nematic field and whether this promotes, or inhibits, extensile forces. Moreover, while epithelial layers do not show orientational order at long length and time-scales, other confluent tissues of different cell types, such as fibroblasts, do [21]. Further, fibroblasts also exhibit contractile collective behaviour [28]. It would therefore be interesting to examine effects of polar forces on the active nematic behaviour of the system in the presence of order in the nematic field, to investigate whether this promotes contractile behaviour.

In addition, although our numerical findings using the AVM supported our results in the case of passive nematics, we are still yet to illustrate the case where a change in behaviour occurs as active contractility and cell shape fluctuations increase in magnitude. Introducing active contractile nematic forces to our AVM [196], and investigating defect dynamics as they are increased in magnitude, would demonstrate this and allow us to examine this transition in more detail.

This would also allow a more thorough investigation into the relative roles of cell-cell and cell-substrate interactions in tissue dynamics. Current methods for experimentally determining the internal stress in cell layers assume cell-substrate interactions arising from active traction forces are negligible, and that experimentally measured traction forces on a substrate are entirely the result of cell-cell interactions [197]. From this assumption, Bayesian inference techniques are used to deduce the internal tissue stress from the measured traction forces. However, our results in Chapter 2 point to the importance of cell-substrate interactions in controlling tissue collective behaviour. If the proportion of the measured traction that is generated from active traction forces is non-negligible, this could cause a significant error in the calculated stress field. Using the AVM, where we have access to all the component forces in the tissue, along with the resultant traction force cells exert, would allow us to investigate in detail whether this is the case and what impact the inclusion of active traction forces has on the measured tissue stress. This could have a profound

impact on our understanding of the contributions different forces and interactions have on the internal state of the tissue.

Our defect detection method could be readily implemented to aid analysis on this extended AVM. It could also be valuable to the field to extend this method to detect other defect types, such as ± 1 defects. Integer defects have been engineered to arise in cellular systems [198, 199] and have also been linked to morphogenetic processes [31, 200], making effective methods to detect increasingly relevant. Moreover, using machine learning methods creates the possibility of being able to differentiate between different types of $+1$ defect, such as aster and spiral defects. The difficulty here, however, would be obtaining the necessary training data, as ± 1 defects very rarely form in the AVM, meaning a different or modified model would be needed.

The investigation in Chapter 4 focussed on the role cell proliferation plays in tissue interface dynamics. However, this process often occurs in tandem with collective cell migration at the tissue edge. As previous work has shown how motility and collective motion can be introduced into our LBM model [106], the next step in this investigation would be to introduce this along with proliferation to investigate how the two different forms of activity integrate to govern the dynamics of the front. While we do not anticipate this would alter the KPZ scaling of a stable interface, how motility forces impact the stability of the interface is far from trivial and could stimulate further theoretical investigation. Additionally, active nematic stresses have previously been studied in connection to tissue interface stability [14, 45]. It would, therefore, be interesting to implement a nematic field in our LBM, to enable us to study how active nematic forces integrate with cell proliferation and motility to govern interfacial dynamics. More broadly, there is currently no active nematic LBM for a dry system, so its development would be beneficial for the field of active matter.

Further, as previously discussed, our investigation focussed on a single value of

frictional dissipation in our system, and at very high values of friction our system appears to undergo a roughening transition, where the steady-state interface width becomes independent of the size of the system [163]. Although this is most likely not a physically relevant regime, investigating the nature of the transition in detail, and the impact of friction on the system more generally, would aid our understanding of the model.

There is still much to understand about the emergent behaviour of confluent tissues, with physical theories offering a wide variety of tools and concepts through which to characterise and investigate this behaviour. This work focusses on only sections of the broad array of phenomena available for study. However, we hope the tools and understanding developed here provide, and stimulate, fruitful avenues of future research into these important biological systems.

Bibliography

[1] P. W. Anderson, "More is different," *Science*, vol. 177, no. 4047, pp. 393–396, 1972.

[2] B. Ladoux and R. M. Mège, "Mechanobiology of collective cell behaviours," *Nature Reviews Molecular Cell Biology*, vol. 18, no. 12, pp. 743–757, 2017.

[3] B. Alberts, A. Johnson, J. Lewis, M. Raff, K. Roberts, and P. Walter, *Molecular biology of the cell*. New York: Garland Science, 5th ed. ed., 2008.

[4] R. Moll, W. W. Franke, D. L. Schiller, B. Geiger, and R. Krepler, "The catalog of human cytokeratins: Patterns of expression in normal epithelia, tumors and cultured cells," *Cell*, vol. 31, no. 1, pp. 11–24, 1982.

[5] J. Dai and Y. Yao, "Adaptive ordering and filament polymerization of cell cytoskeleton by tunable nanoarrays," *Nano Research*, vol. 14, no. 3, pp. 620–627, 2021.

[6] R. Ananthakrishnan and A. Ehrlicher, "The forces behind cell movement," *International Journal of Biological Sciences*, vol. 3, no. 5, pp. 303–317, 2007.

[7] U. S. Schwarz and S. A. Safran, "Physics of adherent cells," *Reviews of Modern Physics*, vol. 85, no. 3, pp. 1327–1381, 2013.

[8] V. K. Gupta, S. Nam, D. Yim, J. Camuglia, J. L. Martin, E. N. Sanders, L. E. O'Brien, A. C. Martin, T. Kim, and O. Chaudhuri, "The nature of cell

division forces in epithelial monolayers," *Journal of Cell Biology*, vol. 220, no. 8, p. e202011106, 2021.

[9] N. S. Rossen, J. M. Tarp, J. Mathiesen, M. H. Jensen, and L. B. Oddershede, "Long-range ordered vorticity patterns in living tissue induced by cell division," *Nature Communications*, vol. 5, p. 5720, 2014.

[10] W. Xi, T. B. Saw, D. Delacour, C. T. Lim, and B. Ladoux, "Material approaches to active tissue mechanics," *Nature Reviews Materials*, vol. 4, no. 1, pp. 23–44, 2019.

[11] N. Khalilgharibi, J. Fouchard, P. Recho, G. Charras, and A. Kabla, "The dynamic mechanical properties of cellularised aggregates," *Current Opinion in Cell Biology*, vol. 42, pp. 113–120, 2016.

[12] S. M. Zehnder, M. Suaris, M. M. Bellaire, and T. E. Angelini, "Cell volume fluctuations in MDCK monolayers," *Biophysical Journal*, vol. 108, no. 2, pp. 247–250, 2015.

[13] F. Peglion, F. Llense, and S. Etienne-Manneville, "Adherens junction treadmilling during collective migration," *Nature Cell Biology*, vol. 16, no. 7, pp. 639–651, 2014.

[14] R. Alert, C. Blanch-Mercader, and J. Casademunt, "Active fingering instability in tissue spreading," *Physical Review Letters*, vol. 122, no. 8, p. 88104, 2019.

[15] K. J. Green and J. C. R. Jones, "Desmosomes and hemidesmosomes: structure and function of molecular components," *The FASEB Journal*, vol. 10, no. 8, pp. 871–881, 1996.

[16] A. S. Fanning, B. J. Jameson, L. A. Jesaitis, and J. M. Anderson, "The tight junction protein ZO-1 establishes a link between the transmembrane protein

occludin and the actin cytoskeleton," *Journal of Biological Chemistry*, vol. 273, no. 45, pp. 29745–29753, 1998.

[17] T. Yano, T. Matsui, A. Tamura, M. Uji, and S. Tsukita, "The association of microtubules with tight junctions is promoted by cingulin phosphorylation by AMPK," *Journal of Cell Biology*, vol. 203, no. 4, pp. 605–614, 2013.

[18] S. Jain, V. M. Cachoux, G. H. Narayana, S. de Beco, J. D'Alessandro, V. Cellerin, T. Chen, M. L. Heuzé, P. Marcq, R. M. Mège, A. J. Kabla, C. T. Lim, and B. Ladoux, "The role of single-cell mechanical behaviour and polarity in driving collective cell migration," *Nature Physics*, vol. 16, no. 7, pp. 802–809, 2020.

[19] M. Ozawa, S. Hiver, T. Yamamoto, T. Shibata, S. Upadhyayula, Y. Mimori-Kiyosue, and M. Takeichi, "Adherens junction regulates cryptic lamellipodia formation for epithelial cell migration," *The Journal of cell biology*, vol. 219, no. 10, p. e202006196, 2020.

[20] L. Balasubramaniam, A. Doostmohammadi, T. B. Saw, G. H. N. S. Narayana, R. Mueller, T. Dang, M. Thomas, S. Gupta, S. Sonam, A. S. Yap, Y. Toyama, R.-M. Mège, J. M. Yeomans, and B. Ladoux, "Investigating the nature of active forces in tissues reveals how contractile cells can form extensile monolayers," *Nature Materials*, vol. 20, p. 1156–1166, 2021.

[21] G. Duclos, S. Garcia, H. G. Yevick, and P. Silberzan, "Perfect nematic order in confined monolayers of spindle-shaped cells," *Soft Matter*, vol. 10, no. 14, pp. 2346–2353, 2014.

[22] C. Blanch-Mercader, V. Yashunsky, S. Garcia, G. Duclos, L. Giomi, and P. Silberzan, "Turbulent Dynamics of Epithelial Cell Cultures," *Physical Review Letters*, vol. 120, no. 20, p. 208101, 2018.

[23] M. A. Swartz, D. J. Tschumperlin, R. D. Kamm, and J. M. Drazen, "Mechanical stress is communicated between different cell types to elicit matrix remodeling," *Proceedings of the National Academy of Sciences of the United States of America*, vol. 98, no. 11, pp. 6180–6185, 2001.

[24] A. Chatterjee, P. Kondaiah, and N. Gundiah, "Stress fiber growth and remodeling determines cellular morphomechanics under uniaxial cyclic stretch," *Biomechanics and Modeling in Mechanobiology*, vol. 21, no. 2, pp. 553–567, 2022.

[25] H. L. Sweeney and D. W. Hammers, "Muscle contraction," *Cold Spring Harbour Perspectives in Biology*, vol. 10, p. a023200, 2018.

[26] M. Petrtýl, J. Heřt, and P. Fiala, "Spatial organization of the haversian bone in man," *Journal of Biomechanics*, vol. 29, no. 2, pp. 161–167, 1996.

[27] C. Wang, B. M. Baker, C. S. Chen, and M. A. Schwartz, "Endothelial cell sensing of flow direction," *Arteriosclerosis, Thrombosis, and Vascular Biology*, vol. 33, no. 9, pp. 2130–2136, 2013.

[28] G. Duclos, C. Erlenkämper, J. F. Joanny, and P. Silberzan, "Topological defects in confined populations of spindle-shaped cells," *Nature Physics*, vol. 13, no. 1, pp. 58–62, 2017.

[29] T. B. Saw, A. Doostmohammadi, V. Nier, L. Kocgozlu, S. Thampi, Y. Toyama, P. Marcq, C. T. Lim, J. M. Yeomans, and B. Ladoux, "Topological defects in epithelia govern cell death and extrusion," *Nature*, vol. 544, pp. 212–216, April 2017.

[30] K. Kawaguchi, R. Kageyama, and M. Sano, "Topological defects control collective dynamics in neural progenitor cell cultures," *Nature*, vol. 545, no. 7654, pp. 327–331, 2017.

[31] Y. Maroudas-Sacks, L. Garion, L. Shani-Zerbib, A. Livshits, E. Braun, and K. Keren, "Topological defects in the nematic order of actin fibres as organization centres of hydra morphogenesis," *Nature Physics*, vol. 17, no. 2, pp. 251–259, 2021.

[32] K. Copenhagen, R. Alert, N. S. Wingreen, and J. W. Shaevitz, "Topological defects promote layer formation in myxococcus xanthus colonies," *Nature Physics*, vol. 17, no. 2, pp. 211–215, 2021.

[33] O. J. Meacock, A. Doostmohammadi, K. R. Foster, J. M. Yeomans, and W. M. Durham, "Bacteria solve the problem of crowding by moving slowly," *Nature Physics*, vol. 17, no. 2, pp. 205–210, 2021.

[34] A. Doostmohammadi, S. P. Thampi, and J. M. Yeomans, "Defect-Mediated Morphologies in Growing Cell Colonies," *Physical Review Letters*, vol. 117, no. 4, p. 048102, 2016.

[35] J. Rosenblatt, M. C. Raff, and L. P. Cramer, "An epithelial cell destined for apoptosis signals its neighbors to extrude it by an actin- and myosin-dependent mechanism," *Current Biology*, vol. 11, no. 22, pp. 1847–1857, 2001.

[36] G. T. Eisenhoffer, P. D. Loftus, M. Yoshigi, H. Otsuna, C. B. Chien, P. A. Morcos, and J. Rosenblatt, "Crowding induces live cell extrusion to maintain homeostatic cell numbers in epithelia," *Nature*, vol. 484, no. 7395, pp. 546–549, 2012.

[37] M. Delarue, F. Montel, D. Vignjevic, J. Prost, J.-F. Joanny, and G. Cappello, "Compressive stress inhibits proliferation in tumor spheroids through a volume limitation," *Biophysical Journal*, vol. 107, no. 8, pp. 1821–1828, 2014.

[38] F. Montel, M. Delarue, J. Elgeti, D. Vignjevic, G. Cappello, and J. Prost, "Isotropic stress reduces cell proliferation in tumor spheroids," *New Journal of Physics*, vol. 14, p. 055008, 2012.

[39] M. Louveaux, J. D. Julien, V. Mirabet, A. Boudaoud, and O. Hamant, "Cell division plane orientation based on tensile stress in Arabidopsis thaliana," *Proceedings of the National Academy of Sciences of the United States of America*, vol. 113, no. 30, pp. E4294–E4303, 2016.

[40] E. Scarpa and R. Mayor, "Collective cell migration in development," *Journal of Cell Biology*, vol. 212, no. 2, pp. 143–155, 2016.

[41] S. Alexander, G. E. Koehl, M. Hirschberg, E. K. Geissler, and P. Friedl, "Dynamic imaging of cancer growth and invasion: A modified skin-fold chamber model," *Histochemistry and Cell Biology*, vol. 130, no. 6, pp. 1147–1154, 2008.

[42] D. Cai, S. C. Chen, M. Prasad, L. He, X. Wang, V. Choesmel-Cadamuro, J. K. Sawyer, G. Danuser, and D. J. Montell, "Mechanical feedback through E-cadherin promotes direction sensing during collective cell migration," *Cell*, vol. 157, no. 5, pp. 1146–1159, 2014.

[43] D. T. Tambe, C. Corey Hardin, T. E. Angelini, K. Rajendran, C. Y. Park, X. Serra-Picamal, E. H. Zhou, M. H. Zaman, J. P. Butler, D. A. Weitz, J. J. Fredberg, and X. Trepat, "Collective cell guidance by cooperative intercellular forces," *Nature Materials*, vol. 10, no. 6, pp. 469–475, 2011.

[44] X. Trepat, M. R. Wasserman, T. E. Angelini, E. Millet, D. A. Weitz, J. P. Butler, and J. J. Fredberg, "Physical forces during collective cell migration," *Nature Physics*, vol. 5, no. 6, pp. 426–430, 2009.

[45] C. Trenado, L. L. Bonilla, and A. Martínez-Calvo, "Fingering instability in spreading epithelial monolayers: roles of cell polarisation, substrate friction and contractile stresses," *Soft Matter*, vol. 17, no. 36, pp. 8276–8290, 2021.

[46] D. Nesbitt, G. Pruessner, and C. F. Lee, "Edge instability in incompressible planar active fluids," *Physical Review E*, vol. 96, no. 6, p. 062615, 2017.

[47] J. Zimmermann, M. Basan, and H. Levine, "An instability at the edge of a tissue of collectively migrating cells can lead to finger formation during wound healing," *European Physical Journal: Special Topics*, vol. 223, no. 7, pp. 1259–1264, 2014.

[48] X. Serra-Picamal, V. Conte, R. Vincent, E. Anon, D. T. Tambe, E. Bazellieres, J. P. Butler, J. J. Fredberg, and X. Trepat, "Mechanical waves during tissue expansion," *Nature Physics*, vol. 8, no. 8, pp. 628–634, 2012.

[49] M. A. Huergo, M. A. Pasquale, A. E. Bolzán, A. J. Arvia, and P. H. González, "Morphology and dynamic scaling analysis of cell colonies with linear growth fronts," *Physical Review E - Statistical, Nonlinear, and Soft Matter Physics*, vol. 82, no. 3, p. 031903, 2010.

[50] A. Brú, J. M. Pastor, I. Fernaud, I. Brú, S. Melle, and C. Berenguer, "Super-rough dynamics on tumor growth," *Physical Review Letters*, vol. 81, no. 18, pp. 4008–4011, 1998.

[51] A. Brú, S. Albertos, J. L. Subiza, J. L. García-Asenjo, and I. Brú, "The Universal Dynamics of Tumor Growth," *Biophysical Journal*, vol. 85, no. 5, pp. 2948–2961, 2003.

[52] J. Galeano, J. Buceta, K. Juarez, B. Pumariño, J. De la Torre, and J. M. Iriondo, "Dynamical scaling analysis of plant callus growth," *Europhysics Letters*, vol. 63, no. 1, pp. 83–89, 2003.

[53] M. C. Marchetti, J. F. Joanny, S. Ramaswamy, T. B. Liverpool, J. Prost, M. Rao, and R. A. Simha, "Hydrodynamics of soft active matter," *Reviews of Modern Physics*, vol. 85, no. 3, pp. 1143–1189, 2013.

[54] F. Ginelli, F. Peruani, M. H. Pillot, H. Chaté, G. Theraulaz, and R. Bon, "Intermittent collective dynamics emerge from conflicting imperatives in sheep

herds," *Proceedings of the National Academy of Sciences of the United States of America*, vol. 112, no. 41, pp. 12729–12734, 2015.

[55] W. Bialek, A. Cavagna, I. Giardina, T. Mora, O. Pohl, E. Silvestri, M. Viale, and A. M. Walczak, "Social interactions dominate speed control in poising natural flocks near criticality," *Proceedings of the National Academy of Sciences of the United States of America*, vol. 111, no. 20, pp. 7212–7217, 2014.

[56] Z. You, D. J. Pearce, A. Sengupta, and L. Giomi, "Geometry and Mechanics of Microdomains in Growing Bacterial Colonies," *Physical Review X*, vol. 8, no. 3, p. 31065, 2018.

[57] V. Schaller, C. Weber, C. Semmrich, E. Frey, and A. R. Bausch, "Polar patterns of driven filaments," *Nature*, vol. 467, no. 7311, pp. 73–77, 2010.

[58] S. Henkes, K. Kostanjevec, J. M. Collinson, R. Sknepnek, and E. Bertin, "Dense active matter model of motion patterns in confluent cell monolayers," *Nature Communications*, vol. 11, no. 1, p. 1405, 2020.

[59] S. F. Schoeller and E. E. Keaveny, "From flagellar undulations to collective Motion: Predicting the dynamics of sperm suspensions," *Journal of the Royal Society Interface*, vol. 15, no. 140, p. 20170834, 2018.

[60] H. H. Wensink, J. Dunkel, S. Heidenreich, K. Drescher, R. E. Goldstein, H. Löwen, and J. M. Yeomans, "Meso-scale turbulence in living fluids," *Proceedings of the National Academy of Sciences*, vol. 109, no. 36, pp. 14308–14313, 2012.

[61] T. Sanchez, D. T. Chen, S. J. Decamp, M. Heymann, and Z. Dogic, "Spontaneous motion in hierarchically assembled active matter," *Nature*, vol. 491, no. 7424, pp. 431–434, 2012.

[62] H. Chaté, F. Ginelli, and R. Montagne, "Simple model for active nematics: Quasi-long-range order and giant fluctuations," *Physical Review Letters*, vol. 96, no. 18, p. 180602, 2006.

[63] A. Chardac, L. A. Hoffmann, Y. Poupart, L. Giomi, and D. Bartolo, "Topology-Driven Ordering of Flocking Matter," *Physical Review X*, vol. 11, no. 3, p. 031069, 2021.

[64] D. Huterer and T. Vachaspati, "Distribution of singularities in the cosmic microwave background polarization," *Physical Review D - Particles, Fields, Gravitation and Cosmology*, vol. 72, no. 4, p. 043004, 2005.

[65] S. Rafaï, L. Jibuti, and P. Peyla, "Effective viscosity of microswimmer suspensions," *Physical Review Letters*, vol. 104, no. 9, p. 098102, 2010.

[66] L. Giomi, M. J. Bowick, P. Mishra, R. Sknepnek, and M. Cristina Marchetti, "Defect dynamics in active nematics," *Philosophical Transactions of the Royal Society A: Mathematical, Physical and Engineering Sciences*, vol. 372, no. 2029, p. 20130365, 2014.

[67] T. Vicsek, A. Czirók, E. Ben-Jacob, I. Cohen, and O. Shochet, "Novel type of phase transition in a system of self-driven particles," *Phys. Rev. Lett.*, vol. 75, pp. 1226–1229, Aug 1995.

[68] B. Szabó, G. J. Szöllösi, B. Gönci, Z. Jurányi, D. Selmeczi, and T. Vicsek, "Phase transition in the collective migration of tissue cells: Experiment and model," *Physical Review E - Statistical, Nonlinear, and Soft Matter Physics*, vol. 74, no. 6, p. 061908, 2006.

[69] F. Ginelli and H. Chaté, "Relevance of metric-free interactions in flocking phenomena," *Physical Review Letters*, vol. 105, no. 16, p. 168103, 2010.

[70] A. Cavagna, A. Culla, X. Feng, I. Giardina, T. S. Grigera, W. Kion-Crosby, S. Melillo, G. Pisegna, L. Postiglione, and P. Villegas, "Marginal speed confinement resolves the conflict between correlation and control in collective behaviour," *Nature Communications*, vol. 13, no. 1, p. 2315, 2022.

[71] P. Romanczuk, M. Bär, W. Ebeling, B. Lindner, and L. Schimansky-Geier, "Active Brownian particles: From individual to collective stochastic dynamics: From individual to collective stochastic dynamics," *European Physical Journal: Special Topics*, vol. 202, no. 1, pp. 1–162, 2012.

[72] S. Henkes, Y. Fily, and M. C. Marchetti, "Active jamming: Self-propelled soft particles at high density," *Physical Review E - Statistical, Nonlinear, and Soft Matter Physics*, vol. 84, no. 4, pp. 84–87, 2011.

[73] B. Ten Hagen, R. Wittkowski, D. Takagi, F. Kümmel, C. Bechinger, and H. Löwen, "Can the self-propulsion of anisotropic microswimmers be described by using forces and torques?," *Journal of Physics Condensed Matter*, vol. 27, no. 19, p. 194110, 2015.

[74] F. Ginelli, F. Peruani, M. Bär, and H. Chaté, "Large-scale collective properties of self-propelled rods," *Physical Review Letters*, vol. 104, no. 18, p. 184502, 2010.

[75] F. Graner and J. A. Glazier, "Simulation of biological cell sorting using a two-dimensional extended Potts model," *Physical Review Letters*, vol. 69, no. 13, pp. 2013–2016, 1992.

[76] A. Szabó, R. Ünnep, E. Méhes, W. O. Twal, W. S. Argraves, Y. Cao, and A. Czirók, "Collective cell motion in endothelial monolayers," *Physical Biology*, vol. 7, no. 4, p. 046007, 2010.

[77] L. Coburn, H. Lopez, I. M. Schouwenaar, A. S. Yap, V. Lobaskin, and G. A. Gomez, "Role of contact inhibition of locomotion and junctional mechanics

in epithelial collective responses to injury," *Physical Biology*, vol. 15, no. 2, p. 024001, 2018.

[78] F. J. Segerer, F. Thüroff, A. Piera Alberola, E. Frey, and J. O. Rädler, "Emergence and persistence of collective cell migration on small circular micropatterns," *Physical Review Letters*, vol. 114, no. 22, p. 228102, 2015.

[79] D. L. Barton, S. Henkes, C. J. Weijer, and R. Sknepnek, "Active Vertex Model for cell-resolution description of epithelial tissue mechanics," *PLoS Computational Biology*, vol. 13, no. 6, pp. 1–34, 2017.

[80] B. Palmieri, Y. Bresler, D. Wirtz, and M. Grant, "Multiple scale model for cell migration in monolayers: Elastic mismatch between cells enhances motility," *Scientific Reports*, vol. 5, p. 11745, 2015.

[81] F. Campelo and A. Hernández-Machado, "Dynamic model and stationary shapes of fluid vesicles," *European Physical Journal E*, vol. 20, no. 1, pp. 37–45, 2006.

[82] H. Emmerich, H. Löwen, R. Wittkowski, T. Gruhn, G. I. Tóth, G. Tegze, and L. Gránásy, "Phase-field-crystal models for condensed matter dynamics on atomic length and diffusive time scales: an overview," *Advances in Physics*, vol. 61, no. 6, pp. 665–743, 2012.

[83] G. Peyret, R. Mueller, J. D'Alessandro, S. Begnaud, P. Marcq, R. M. Mège, J. M. Yeomans, A. Doostmohammadi, and B. Ladoux, "Sustained Oscillations of Epithelial Cell Sheets," *Biophysical Journal*, vol. 117, no. 3, pp. 464–478, 2019.

[84] S. Monfared, G. Ravichandran, J. E. Andrade, and A. Doostmohammadi, "Stress percolation criticality of glass to fluid transition in active cell layers," *arXiv pre-print*, no. 2210.08112, 2022.

[85] R. Mueller, J. M. Yeomans, and A. Doostmohammadi, "Emergence of active nematic behavior in monolayers of isotropic cells," *Phys. Rev. Lett.*, vol. 122, p. 048004, Feb 2019.

[86] G. Zhang and J. M. Yeomans, "Active forces in confluent cell monolayers," *Phys. Rev. Lett.*, vol. 130, p. 038202, Jan 2023.

[87] D. Bi, J. H. Lopez, J. M. Schwarz, and M. L. Manning, "A density-independent rigidity transition in biological tissues," *Nature Physics*, vol. 11, no. 12, pp. 1074–1079, 2015.

[88] D. M. Sussman, "cellGPU: Massively parallel simulations of dynamic vertex models," *Computer Physics Communications*, vol. 219, pp. 400–406, 2017.

[89] C. Duclut, J. Paijmans, M. M. Inamdar, C. D. Modes, and F. Jülicher, "Active T1 transitions in cellular networks," *European Physical Journal E*, vol. 45, no. 3, p. 29, 2022.

[90] R. Sknepnek, I. Djafer-Cherif, M. Chuai, C. J. Weijer, and S. Henkes, "Generating active T1 transitions through mechanochemical feedback," *arXiv preprint*, no. 2106.12394, 2021.

[91] M. Czajkowski, D. M. Sussman, M. C. Marchetti, and M. L. Manning, "Glassy dynamics in models of confluent tissue with mitosis and apoptosis," *Soft Matter*, vol. 15, pp. 9133–9149, 2019.

[92] S. Kim, M. Pochitaloff, G. A. Stooke-Vaughan, and O. Campàs, "Embryonic tissues as active foams," *Nature Physics*, vol. 17, no. 7, pp. 859–866, 2021.

[93] B. Monier, M. Gettings, G. Gay, T. Mangeat, S. Schott, A. Guarner, and M. Suzanne, "Apico-basal forces exerted by apoptotic cells drive epithelium folding," *Nature*, vol. 518, no. 7538, pp. 245–248, 2015.

[94] X. Li, A. Das, and D. Bi, "Mechanical Heterogeneity in Tissues Promotes Rigidity and Controls Cellular Invasion," *Physical Review Letters*, vol. 123, no. 5, p. 58101, 2019.

[95] D. Bi, X. Yang, M. C. Marchetti, and M. L. Manning, "Motility-driven glass and jamming transitions in biological tissues," *Physical Review X*, vol. 6, no. 2, p. 021011, 2016.

[96] V. Petrolli, M. Le Goff, M. Tadrous, K. Martens, C. Allier, O. Mandula, L. Hervé, S. Henkes, R. Sknepnek, T. Boudou, G. Cappello, and M. Balland, "Confinement-Induced Transition between Wavelike Collective Cell Migration Modes," *Physical Review Letters*, vol. 122, no. 16, p. 168101, 2019.

[97] J. Toner and Y. Tu, "Long-Range Order in a Two-Dimensional Dynamical *XY* Model: How Birds Fly Together," *Physical Review Letters*, vol. 75, no. 23, pp. 4326–4329, 1995.

[98] J. Toner and Y. Tu, "Flocks, herds, and schools: A quantitative theory of flocking," *Physical Review E*, vol. 58, pp. 4828–4858, oct 1998.

[99] A. N. Beris and B. J. Edwards, *Thermodynamics of Flowing Systems: With Internal Microstructure*. Oxford: Oxford University Press, 1994.

[100] D. Marenduzzo, E. Orlandini, M. E. Cates, and J. M. Yeomans, "Steady-state hydrodynamic instabilities of active liquid crystals: Hybrid lattice Boltzmann simulations," *Physical Review E - Statistical, Nonlinear, and Soft Matter Physics*, vol. 76, no. 3, p. 031921, 2007.

[101] J. D. Gibbon, K. V. Kiran, N. B. Padhan, and R. Pandit, "An analytical and computational study of the incompressible Toner–Tu Equations," *Physica D: Nonlinear Phenomena*, vol. 444, p. 133594, 2023.

[102] N. Rana and P. Perlekar, "Coarsening in the two-dimensional incompressible Toner-Tu equation: Signatures of turbulence," *Physical Review E*, vol. 102, no. 3, p. 032617, 2020.

[103] U. Frisch, B. Hasslacher, and Y. Pomeau, "Lattice-gas automata for the Navier-Stokes equation," *Physical Review Letters*, vol. 56, no. 14, pp. 1505–1508, 1986.

[104] H. Chen, S. Chen, and W. H. Matthaeus, "Recovery of the Navier-Stokes equations using a lattice-gas Boltzmann method," *Physical Review A*, vol. 45, no. 8, pp. 5339–5342, 1992.

[105] C. Denniston, E. Orlandini, and J. M. Yeomans, "Lattice Boltzmann simulations of liquid crystal hydrodynamics," *Physical Review E - Statistical Physics, Plasmas, Fluids, and Related Interdisciplinary Topics*, vol. 63, no. 5, p. 056702, 2001.

[106] D. Nesbitt, G. Pruessner, and C. F. Lee, "Uncovering novel phase transitions in dense dry polar active fluids using a lattice boltzmann method," *New Journal of Physics*, vol. 23, no. 4, p. 043047, 2021.

[107] S. P. Thampi, R. Golestanian, and J. M. Yeomans, "Instabilities and topological defects in active nematics," *EPL (Europhysics Letters)*, vol. 105, no. 1, p. 18001, 2014.

[108] A. Doostmohammadi, T. N. Shendruk, K. Thijssen, and J. M. Yeomans, "Onset of meso-scale turbulence in active nematics," *Nature Communications*, vol. 8, p. 15326, 2017.

[109] A. Doostmohammadi, S. P. Thampi, T. B. Saw, C. T. Lim, B. Ladoux, and J. M. Yeomans, "Celebrating Soft Matter's 10th Anniversary: Cell division: a source of active stress in cellular monolayers," *Soft Matter*, vol. 11, no. 37, pp. 7328–7336, 2015.

[110] J. Colen, M. Han, R. Zhang, S. A. Redford, L. M. Lemma, and L. Morgan, "Machine learning active-nematic hydrodynamics," *PNAS*, vol. 118, no. 10, p. e2016708118, 2021.

[111] M. J. Bowick, N. Fakhri, M. C. Marchetti, and S. Ramaswamy, "Symmetry, thermodynamics, and topology in active matter," *Phys. Rev. X*, vol. 12, p. 010501, Feb 2022.

[112] I. H. Sarker, "Machine Learning: Algorithms, Real-World Applications and Research Directions," *SN Computer Science*, vol. 2, no. 3, p. 160, 2021.

[113] M. Nielsen, *Neural Networks and Deep Learning*. Determination Press, 2015.

[114] C. Joshi, S. Ray, L. Lemma, M. Varghese, G. Sharp, Z. Dogic, A. Baskaran, and M. F. Hagan, "Data-driven discovery of active nematic hydrodynamics," *Physical Review Letters*, vol. 129, no. 25, p. 258001, 2022.

[115] M. Golden, R. Grigoriev, J. Nambisan, and A. Fernandez-Nieves, "Physically-informed data-driven modeling of active nematics," *arXiv pre-print*, no. 2202.12853, 2022.

[116] R. Supekar, B. Song, A. Hastewell, G. P. T. Choi, A. Mietke, and J. Dunkel, "Learning hydrodynamic equations for active matter from particle simulations and experiments," *arXiv pre-print*, no. 2101.06568, 2021.

[117] A. R. Dulaney and J. F. Brady, "Machine learning for phase behavior in active matter systems," *Soft Matter*, vol. 17, no. 28, pp. 6808–6816, 2021.

[118] M. Walters, Q. Wei, and J. Z. Chen, "Machine learning topological defects of confined liquid crystals in two dimensions," *Physical Review E*, vol. 99, no. 6, p. 062701, 2019.

[119] D. Wenzel, M. Nestler, S. Reuther, M. Simon, and A. Voigt, "Defects in Active Nematics-Algorithms for Identification and Tracking," *Computational Methods in Applied Mathematics*, vol. 21, no. 3, pp. 683–692, 2021.

[120] W. Pomp, K. Schakenraad, H. E. Balcloğlu, H. Van Hoorn, E. H. Danen, R. M. Merks, T. Schmidt, and L. Giomi, "Cytoskeletal Anisotropy Controls Geometry and Forces of Adherent Cells," *Physical Review Letters*, vol. 121, no. 17, p. 178101, 2018.

[121] D. Volfson, S. Cookson, J. Hasty, and L. S. Tsimring, "Biomechanical ordering of dense cell populations," *Proceedings of the National Academy of Sciences of the United States of America*, vol. 105, no. 40, pp. 15346–15351, 2008.

[122] G. Duclos, C. Blanch-Mercader, V. Yashunsky, G. Salbreux, J. F. Joanny, J. Prost, and P. Silberzan, "Spontaneous shear flow in confined cellular nematics," *Nature Physics*, vol. 14, no. 7, pp. 728–732, 2018.

[123] N. D. Bade, R. D. Kamien, R. K. Assoian, and K. J. Stebe, "Edges impose planar alignment in nematic monolayers by directing cell elongation and enhancing migration," *Soft Matter*, vol. 14, no. 33, pp. 6867–6874, 2018.

[124] T. B. Saw, W. Xi, B. Ladoux, and C. T. Lim, "Biological Tissues as Active Nematic Liquid Crystals," *Advanced Materials*, vol. 30, no. 47, p. 1802579, 2018.

[125] A. Baskaran and M. C. Marchetti, "Hydrodynamics of self-propelled hard rods," *Phys. Rev. E*, vol. 77, p. 011920, Jan 2008.

[126] S. P. Thampi, A. Doostmohammadi, R. Golestanian, and J. M. Yeomans, "Intrinsic free energy in active nematics," *EPL (Europhysics Letters)*, vol. 112, no. 2, p. 28004, 2015.

[127] S. Santhosh, M. R. Nejad, A. Doostmohammadi, J. M. Yeomans, and S. P. Thampi, "Activity Induced Nematic Order in Isotropic Liquid Crystals," *Journal of Statistical Physics*, vol. 180, p. 699–709, 2020.

[128] S. Thutupalli, M. Sun, F. Bunyak, K. Palaniappan, and J. W. Shaevitz, "Directional reversals enable Myxococcus xanthus cells to produce collective one-dimensional streams during fruiting-body formation," *Journal of the Royal Society Interface*, vol. 12, no. 109, p. 20150049, 2015.

[129] F. Vafa, M. J. Bowick, B. I. Shraiman, and M. C. Marchetti, "Fluctuations can induce local nematic order and extensile stress in monolayers of motile cells," *Soft Matter*, vol. 17, pp. 3068–3073, 2021.

[130] T. Svitkina, "The actin cytoskeleton and actin-based motility," *Cold Spring Harbor Perspectives in Biology*, vol. 10, no. 1, p. a018267, 2018.

[131] L. Chen, C. F. Lee, and J. Toner, "Mapping two-dimensional polar active fluids to two-dimensional soap and one-dimensional sandblasting," *Nature Communications*, vol. 7, p. 12215, nov 2016.

[132] R. Aditi Simha and S. Ramaswamy, "Hydrodynamic fluctuations and instabilities in ordered suspensions of self-propelled particles," *Physical review letters*, vol. 89, no. 5, p. 058101, 2002.

[133] S. Ramaswamy, R. A. Simha, and J. Toner, "Active nematics on a substrate: Giant number fluctuations and long-time tails," *Europhysics Letters*, vol. 62, no. 2, pp. 196–202, 2003.

[134] S. Mishra, A. Simha, and S. Ramaswamy, "A dynamic renormalization group study of active nematics," *Journal of Statistical Mechanics: Theory and Experiment*, vol. 2010, no. 2, p. P02003, 2010.

[135] S. Shankar, S. Ramaswamy, and M. C. Marchetti, "Low-noise phase of a two-dimensional active nematic system," *Physical Review E*, vol. 97, p. 012707, jan 2018.

[136] P. Sartori and C. F. Lee, "Scaling behaviour of non-equilibrium planar N -atic spin systems under weak fluctuations," *New Journal of Physics*, vol. 21, p. 073064, jul 2019.

[137] L. Chen, J. Toner, and C. F. Lee, "Critical phenomenon of the order-disorder transition in incompressible active fluids," *New Journal of Physics*, vol. 17, p. 042002, 2015.

[138] A. Doostmohammadi, J. Ignés-Mullol, J. M. Yeomans, and F. Sagués, "Active nematics," *Nature Communications*, vol. 9, no. 1, p. 3246, 2018.

[139] L. Giomi, M. J. Bowick, X. Ma, and M. C. Marchetti, "Defect annihilation and proliferation in active Nematics," *Physical Review Letters*, vol. 110, no. 22, pp. 1–5, 2013.

[140] L. D. Landau, E. M. Lifshitz, A. M. Kosevich, J. B. Sykes, L. P. Pitaevskii, and W. H. Reid, *Theory of Elasticity: Volume 7*. Course of theoretical physics, Elsevier Science, 1986.

[141] A. Maitra and S. Ramaswamy, "Oriented Active Solids," *Physical Review Letters*, vol. 123, no. 23, p. 238001, 2019.

[142] M. R. Shaebani, A. Wysocki, R. G. Winkler, G. Gompper, and H. Rieger, "Computational models for active matter," *Nature Reviews Physics*, vol. 2, no. 4, pp. 181–199, 2020.

[143] X. Yang, D. Bi, M. Czajkowski, M. Merkel, M. L. Manning, and M. C. Marchetti, "Correlating cell shape and cellular stress in motile confluent tis-

sues," *Proceedings of the National Academy of Sciences of the United States of America*, vol. 114, no. 48, pp. 12663–12668, 2017.

[144] A. J. Vromans and L. Giomi, "Orientational properties of nematic disclinations," *Soft Matter*, vol. 12, no. 30, pp. 6490–6495, 2016.

[145] L. Bonn, A. Ardaševa, R. Mueller, T. N. Shendruk, and A. Doostmohammadi, "Fluctuation-induced dynamics of nematic topological defects," *Physical Review E*, vol. 106, no. 4, p. 044706, 2022.

[146] V. Narayan, S. Ramaswamy, N. Menon, T. Caspt, and T. Caspt, "Long-Lived Giant Number Fluctuations in a Swarming Granular Nematic," *Science*, vol. 317, no. July, pp. 105–108, 2007.

[147] P.-G. de Gennes, *The physics of liquid crystals*. Oxford: Oxford University Press, 1974.

[148] S. J. DeCamp, G. S. Redner, A. Baskaran, M. F. Hagan, and Z. Dogic, "Orientational order of motile defects in active nematics," *Nature Materials*, vol. 14, no. 11, pp. 1110–1115, 2015.

[149] P. W. Ellis, D. J. Pearce, Y. W. Chang, G. Goldsztein, L. Giomi, and A. Fernandez-Nieves, "Curvature-induced defect unbinding and dynamics in active nematic toroids," *Nature Physics*, vol. 14, no. 1, pp. 85–90, 2018.

[150] L. Giomi, J. Toner, and N. Sarkar, "Hydrodynamic theory of p -atic liquid crystals," *Physical Review E*, vol. 106, no. 2, pp. 1–23, 2022.

[151] J.-M. Armengol-Collado, L. N. Carenza, J. Eckert, D. Krommydas, and L. Giomi, "Epithelia are multiscale active liquid crystals," *arXiv pre-print*, no. 2210.08112, 2022.

[152] S. Sonam, L. Balasubramaniam, S. Z. Lin, Y. M. Y. Ivan, I. Pi-Jaumà, C. Jebane, M. Karnat, Y. Toyama, P. Marcq, J. Prost, R. M. Mège, J. F. Rupprecht,

and B. Ladoux, "Mechanical stress driven by rigidity sensing governs epithelial stability," *Nature Physics*, vol. 19, no. 1, pp. 132–141, 2023.

[153] E. Hedlund, K. Hedlund, A. Green, R. Chowdhury, C. S. Park, J. E. Maclennan, and N. A. Clark, "Detection of islands and droplets on smectic films using machine learning," *Physics of Fluids*, vol. 34, no. 10, p. 103608, 2022.

[154] Z. Zhou, C. Joshi, R. Liu, M. M. Norton, L. Lemma, Z. Dogic, M. F. Hagan, S. Fraden, and P. Hong, "Machine learning forecasting of active nematics," *Soft Matter*, vol. 17, no. 3, pp. 738–747, 2021.

[155] M. J. Beach, A. Golubeva, and R. G. Melko, "Machine learning vortices at the Kosterlitz-Thouless transition," *Physical Review B*, vol. 97, no. 4, p. 045207, 2018.

[156] E. N. Minor, S. D. Howard, A. A. Green, M. A. Glaser, C. S. Park, and N. A. Clark, "End-to-end machine learning for experimental physics: Using simulated data to train a neural network for object detection in video microscopy," *Soft Matter*, vol. 16, no. 7, pp. 1751–1759, 2020.

[157] J. Schindelin, I. Arganda-Carreras, E. Frise, V. Kaynig, M. Longair, T. Pietzsch, S. Preibisch, C. Rueden, S. Saalfeld, B. Schmid, J. Y. Tinevez, D. J. White, V. Hartenstein, K. Eliceiri, P. Tomancak, and A. Cardona, "Fiji: An open-source platform for biological-image analysis," *Nature Methods*, vol. 9, no. 7, pp. 676–682, 2012.

[158] X. Glorot and Y. Bengio, "Understanding the difficulty of training deep feedforward neural networks," in *Proceedings of the Thirteenth International Conference on Artificial Intelligence and Statistics* (Y. W. Teh and M. Titterington, eds.), vol. 9 of *Proceedings of Machine Learning Research*, (Chia Laguna Resort, Sardinia, Italy), pp. 249–256, 2010.

[159] T. Mammoto and D. E. Ingber, "Mechanical control of tissue and organ development," *Development*, vol. 137, no. 9, pp. 1407–1420, 2010.

[160] J. Ranft, M. Basan, J. Elgeti, J. F. Joanny, J. Prost, and F. Jülicher, "Fluidization of tissues by cell division and apoptosis," *Proceedings of the National Academy of Sciences of the United States of America*, vol. 107, no. 49, pp. 20863–20868, 2010.

[161] R. Etournay, M. Popović, M. Merkel, A. Nandi, C. Blasse, B. Aigouy, H. Brandl, G. Myers, G. Salbreux, F. Jülicher, and S. Eaton, "Interplay of cell dynamics and epithelial tension during morphogenesis of the *Drosophila* pupal wing," *eLife*, vol. 4, p. e07090, jun 2015.

[162] V. Hakim and P. Silberzan, "Collective cell migration: a physics perspective," *Reports on Progress in Physics*, vol. 80, no. 7, p. 076601, 2017.

[163] A.-L. Barabási and H. E. Stanley, *Fractal Concepts in Surface Growth*. Cambridge University Press, 1995.

[164] M. Block, E. Schöll, and D. Drasdo, "Classifying the expansion kinetics and critical surface dynamics of growing cell populations," *Physical Review Letters*, vol. 99, no. 24, p. 248101, 2007.

[165] S. N. Santalla and S. C. Ferreira, "Eden model with nonlocal growth rules and kinetic roughening in biological systems," *Physical Review E*, vol. 98, no. 2, p. 022405, 2018.

[166] M. Mazarei, J. Åström, J. Westerholm, and M. Karttunen, "Epithelial Tissue Growth Dynamics: Universal or Not?," *arXiv*, p. 2203.15883, 2022.

[167] Y. Azimzade, A. A. Saberi, and M. Sahimi, "Effect of heterogeneity and spatial correlations on the structure of a tumor invasion front in cellular environments," *Physical Review E*, vol. 100, no. 6, p. 62409, 2019.

[168] C. F. Lee, "Interface stability, interface fluctuations, and the gibbs–thomson relationship in motility-induced phase separations," *Soft Matter*, vol. 13, pp. 376–385, 2017.

[169] A. Patch, D. M. Sussman, D. Yllanes, and M. C. Marchetti, "Curvature-dependent tension and tangential flows at the interface of motility-induced phases," *Soft Matter*, vol. 14, pp. 7435–7445, 2018.

[170] W. W. Mullins, "Metal Surfaces: Structure, Energetics and Kinetics," *Journal of Applied Physics*, vol. 28, no. 333, pp. 17–66, 1957.

[171] C. Herring, *The Physics of Powder Metallurgy*. New York: McGraw-Hill, 1957.

[172] J. Villain, "Kinetic growth with surface relaxation: Continuum versus atomistic models," *Journal de Physique*, vol. 1, no. 19, pp. 19–42, 1991.

[173] Z. W. Lai and S. Das Sarma, "Kinetic growth with surface relaxation: Continuum versus atomistic models," *Physical Review Letters*, vol. 66, no. 18, pp. 2348–2351, 1991.

[174] T. Vicsek, M. Cserző, and V. K. Horváth, "Self-affine growth of bacterial colonies," *Physica A: Statistical Mechanics and its Applications*, vol. 167, no. 2, pp. 315–321, 1990.

[175] J. Buceta and J. Galeano, "Comments on the article "the universal dynamics of tumor growth" by a. bru et al.," *Biophysical Journal*, vol. 88, no. 5, pp. 3734–3738, 2005.

[176] Y. Yang and H. Levine, "Leader-cell-driven epithelial sheet fingering," *Physical Biology*, vol. 17, no. 4, p. 046003, 2020.

[177] S. Mark, R. Shlomovitz, N. S. Gov, M. Poujade, E. Grasland-Mongrain, and P. Silberzan, "Physical model of the dynamic instability in an expanding cell culture," *Biophysical Journal*, vol. 98, no. 3, pp. 361–370, 2010.

[178] M. H. Köpf and L. M. Pismen, "A continuum model of epithelial spreading," *Soft Matter*, vol. 9, no. 14, pp. 3727–3734, 2013.

[179] M. Basan, J. Elgeti, E. Hannezo, W. J. Rappel, and H. Levine, "Alignment of cellular motility forces with tissue flow as a mechanism for efficient wound healing," *Proceedings of the National Academy of Sciences of the United States of America*, vol. 110, no. 7, pp. 2452–2459, 2013.

[180] M. Basan, J. F. Joanny, J. Prost, and T. Risler, "Undulation instability of epithelial tissues," *Physical Review Letters*, vol. 106, no. 15, p. 158101, 2011.

[181] T. Büscher, A. L. Diez, G. Gompper, and J. Elgeti, "Instability and fingering of interfaces in growing tissue," *New Journal of Physics*, vol. 22, no. 8, p. 083005, 2020.

[182] M. J. Bogdan and T. Savin, "Fingering instabilities in tissue invasion: An active fluid model," *Royal Society Open Science*, vol. 5, no. 12, p. 181579, 2018.

[183] J. J. Williamson and G. Salbreux, "Stability and Roughness of Interfaces in Mechanically Regulated Tissues," *Physical Review Letters*, vol. 121, no. 23, p. 238102, 2018.

[184] J. Devany, D. M. Sussman, T. Yamamoto, M. L. Manning, and M. L. Gardel, "Cell cycle–dependent active stress drives epithelia remodeling," *Proceedings of the National Academy of Sciences of the United States of America*, vol. 118, no. 10, p. e1917853118, 2021.

[185] A. N. Malmi-Kakkada, X. Li, H. S. Samanta, S. Sinha, and D. Thirumalai, "Cell Growth Rate Dictates the Onset of Glass to Fluidlike Transition and Long Time Superdiffusion in an Evolving Cell Colony," *Physical Review X*, vol. 8, no. 2, p. 21025, 2018.

[186] D. A. Matoz-Fernandez, K. Martens, R. Sknepnek, J. L. Barrat, and S. Henkes, "Cell division and death inhibit glassy behaviour of confluent tissues," *Soft Matter*, vol. 13, pp. 3205–3212, 2017.

[187] M. J. Siedlik, S. Manivannan, I. G. Kevrekidis, and C. M. Nelson, "Cell Division Induces and Switches Coherent Angular Motion within Bounded Cellular Collectives," *Biophysical Journal*, vol. 112, no. 11, pp. 2419–2427, 2017.

[188] J. Li, S. K. Schnyder, M. S. Turner, and R. Yamamoto, "Role of the Cell Cycle in Collective Cell Dynamics," *Physical Review X*, vol. 11, no. 3, p. 31025, 2021.

[189] D. Dell'Arciprete, M. L. Blow, A. T. Brown, F. D. Farrell, J. S. Lintuvuori, A. F. McVey, D. Marenduzzo, and W. C. Poon, "A growing bacterial colony in two dimensions as an active nematic," *Nature Communications*, vol. 9, no. 1, p. 4190, 2018.

[190] P. Pearce, B. Song, D. J. Skinner, R. Mok, R. Hartmann, P. K. Singh, H. Jeckel, J. S. Oishi, K. Drescher, and J. Dunkel, "Flow-Induced Symmetry Breaking in Growing Bacterial Biofilms," *Physical Review Letters*, vol. 123, no. 25, p. 258101, 2019.

[191] F. Kempf, R. Mueller, E. Frey, J. M. Yeomans, and A. Doostmohammadi, "Active matter invasion," *Soft Matter*, vol. 15, no. 38, pp. 7538–7546, 2019.

[192] T. Krueger, H. Kusumaatmaja, A. Kuzmin, O. Shardt, G. Silva, and E. Viggen, *The Lattice Boltzmann Method: Principles and Practice*. Graduate Texts in Physics, Springer, 2016.

[193] P. L. Bhatnagar, E. P. Gross, and M. Krook, "A model for collision processes in gases. i. small amplitude processes in charged and neutral one-component systems," *Phys. Rev.*, vol. 94, pp. 511–525, May 1954.

[194] A. Puliafito, L. Hufnagel, P. Neveu, S. Streichan, A. Sigal, D. K. Fygenson, and B. I. Shraiman, "Collective and single cell behavior in epithelial contact inhibition," *Proceedings of the National Academy of Sciences*, vol. 109, no. 3, pp. 739–744, 2012.

[195] J. R. Turner, "Intestinal mucosal barrier function in health and disease," *Nature Reviews Immunology*, vol. 9, no. 11, pp. 799–809, 2009.

[196] S.-z. Lin, M. Merkel, and J.-f. Rupprecht, "Structure and Rheology in Vertex Models under Cell-Shape-Dependent Active Stresses," *Physical Review Letters*, vol. 130, no. 5, p. 58202, 2023.

[197] V. Nier, S. Jain, C. T. Lim, S. Ishihara, B. Ladoux, and P. Marcq, "Inference of internal stress in a cell monolayer," *Biophysical Journal*, vol. 110, no. 7, pp. 1625–1635, 2016.

[198] T. Turiv, J. Krieger, G. Babakhanova, H. Yu, S. V. Shiyanovskii, Q. H. Wei, M. H. Kim, and O. D. Lavrentovich, "Topology control of human fibroblast cells monolayer by liquid crystal elastomer," *Science Advances*, vol. 6, no. 20, p. eaaz6485, 2020.

[199] K. D. Endresen, M. S. Kim, M. Pittman, Y. Chen, and F. Serra, "Topological defects of integer charge in cell monolayers," *Soft Matter*, vol. 17, no. 24, pp. 5878–5887, 2021.

[200] P. Guillamat, C. Blanch-Mercader, G. Pernollet, K. Kruse, and A. Roux, "Integer topological defects organize stresses driving tissue morphogenesis," *Nature Materials*, vol. 21, no. 5, pp. 588–597, 2022.

Appendix A

Reuse and permissions licenses

SPRINGER NATURE LICENSE
TERMS AND CONDITIONS

Feb 14, 2023

This Agreement between Imperial College London -- Andrew Killeen ("You") and Springer Nature ("Springer Nature") consists of your license details and the terms and conditions provided by Springer Nature and Copyright Clearance Center.

License Number	5487570140510
License date	Feb 14, 2023
Licensed Content Publisher	Springer Nature
Licensed Content Publication	Nano Research
Licensed Content Title	Adaptive ordering and filament polymerization of cell cytoskeleton by tunable nanoarrays
Licensed Content Author	Jing Dai et al
Licensed Content Date	Nov 6, 2020
Type of Use	Thesis/Dissertation
Requestor type	academic/university or research institute
Format	electronic
Portion	figures/tables/illustrations
Number of figures/tables/illustrations	1
Will you be translating?	no
Circulation/distribution	1 - 29

Author of this Springer Nature content	no
Title	Emergent dynamics of confluent tissues in homeostasis and growth
Institution name	Imperial College London
Expected presentation date	Mar 2023
Portions	Figure 2a
Requestor Location	Imperial College London 47a Kingsgate Road London, other NW6 4TD United Kingdom Attn: Imperial College London
Total	0.00 GBP

Terms and Conditions

Springer Nature Customer Service Centre GmbH Terms and Conditions

The following terms and conditions ("Terms and Conditions") together with the terms specified in your [RightsLink] constitute the License ("License") between you as Licensee and Springer Nature Customer Service Centre GmbH as Licensor. By clicking 'accept' and completing the transaction for your use of the material ("Licensed Material"), you confirm your acceptance of and obligation to be bound by these Terms and Conditions.

1. Grant and Scope of License

1. 1. The Licensor grants you a personal, non-exclusive, non-transferable, non-sublicensable, revocable, world-wide License to reproduce, distribute, communicate to the public, make available, broadcast, electronically transmit or create derivative works using the Licensed Material for the purpose(s) specified in your RightsLink Licence Details only. Licenses are granted for the specific use requested in the order and for no other use, subject to these Terms and Conditions. You acknowledge and agree that the rights granted to you under this License do not include the right to modify, edit, translate, include in collective works, or create derivative works of the Licensed Material in whole or in part unless expressly stated in your RightsLink Licence Details. You may use the Licensed Material only as permitted under this Agreement and will not reproduce, distribute, display, perform, or otherwise use or exploit any Licensed Material in any way, in whole or in part, except as expressly permitted by this License.

1. 2. You may only use the Licensed Content in the manner and to the extent permitted by these Terms and Conditions, by your RightsLink Licence Details and by any applicable laws.

1. 3. A separate license may be required for any additional use of the Licensed Material, e.g. where a license has been purchased for print use only, separate permission must be obtained for electronic re-use. Similarly, a License is only valid in the language selected and does not apply for editions in other languages unless additional translation rights have been granted separately in the License.

1. 4. Any content within the Licensed Material that is owned by third parties is expressly excluded from the License.

1. 5. Rights for additional reuses such as custom editions, computer/mobile applications, film or TV reuses and/or any other derivative rights requests require additional permission and may be subject to an additional fee. Please apply to journalpermissions@springernature.com or bookpermissions@springernature.com for these rights.

2. Reservation of Rights

Licensor reserves all rights not expressly granted to you under this License. You acknowledge and agree that nothing in this License limits or restricts Licensor's rights in or use of the Licensed Material in any way. Neither this License, nor any act, omission, or statement by Licensor or you, conveys any ownership right to you in any Licensed Material, or to any element or portion thereof. As between Licensor and you, Licensor owns and retains all right, title, and interest in and to the Licensed Material subject to the license granted in Section 1.1. Your permission to use the Licensed Material is expressly conditioned on you not impairing Licensor's or the applicable copyright owner's rights in the Licensed Material in any way.

3. Restrictions on use

3. 1. Minor editing privileges are allowed for adaptations for stylistic purposes or formatting purposes provided such alterations do not alter the original meaning or intention of the Licensed Material and the new figure(s) are still accurate and representative of the Licensed Material. Any other changes including but not limited to, cropping, adapting, and/or omitting material that affect the meaning, intention or moral rights of the author(s) are strictly prohibited.

3. 2. You must not use any Licensed Material as part of any design or trademark.

3. 3. Licensed Material may be used in Open Access Publications (OAP), but any such reuse must include a clear acknowledgment of this permission visible at the same time as the figures/tables/illustration or abstract and which must indicate that the Licensed Material is not part of the governing OA license but has been reproduced with permission. This may be indicated according to any standard referencing system but must include at a minimum 'Book/Journal title, Author, Journal Name (if applicable), Volume (if applicable), Publisher, Year, reproduced with permission from SNCSC'.

4. STM Permission Guidelines

4. 1. An alternative scope of license may apply to signatories of the STM Permissions Guidelines ("STM PG") as amended from time to time and made available at https://www.stm-assoc.org/intellectual-property/permissions/permissions-guidelines/.

4. 2. For content reuse requests that qualify for permission under the STM PG, and which may be updated from time to time, the STM PG supersede the terms and

conditions contained in this License.

4. 3. If a License has been granted under the STM PG, but the STM PG no longer apply at the time of publication, further permission must be sought from the Rightsholder. Contact journalpermissions@springernature.com or bookpermissions@springernature.com for these rights.

5. Duration of License

5. 1. Unless otherwise indicated on your License, a License is valid from the date of purchase ("License Date") until the end of the relevant period in the below table:

Reuse in a medical communications project	Reuse up to distribution or time period indicated in License
Reuse in a dissertation/thesis	Lifetime of thesis
Reuse in a journal/magazine	Lifetime of journal/magazine
Reuse in a book/textbook	Lifetime of edition
Reuse on a website	1 year unless otherwise specified in the License
Reuse in a presentation/slide kit/poster	Lifetime of presentation/slide kit/poster. Note: publication whether electronic or in print of presentation/slide kit/poster may require further permission.
Reuse in conference proceedings	Lifetime of conference proceedings
Reuse in an annual report	Lifetime of annual report
Reuse in training/CME materials	Reuse up to distribution or time period indicated in License
Reuse in newsmedia	Lifetime of newsmedia
Reuse in coursepack/classroom materials	Reuse up to distribution and/or time period indicated in license

6. Acknowledgement

6. 1. The Licensor's permission must be acknowledged next to the Licensed Material in print. In electronic form, this acknowledgement must be visible at the same time as the figures/tables/illustrations or abstract and must be hyperlinked to the journal/book's homepage.

6. 2. Acknowledgement may be provided according to any standard referencing system and at a minimum should include "Author, Article/Book Title, Journal name/Book imprint, volume, page number, year, Springer Nature".

7. Reuse in a dissertation or thesis

7. 1. Where 'reuse in a dissertation/thesis' has been selected, the following terms apply: Print rights of the Version of Record are provided for; electronic rights for use only on institutional repository as defined by the Sherpa guideline (www.sherpa.ac.uk/romeo/) and only up to what is required by the awarding institution.

7. 2. For theses published under an ISBN or ISSN, separate permission is required. Please contact journalpermissions@springernature.com or bookpermissions@springernature.com for these rights.

7. 3. Authors must properly cite the published manuscript in their thesis according to current citation standards and include the following acknowledgement: '*Reproduced with permission from Springer Nature*'.

8. License Fee

You must pay the fee set forth in the License Agreement (the "License Fees"). All amounts payable by you under this License are exclusive of any sales, use, withholding, value added or similar taxes, government fees or levies or other assessments. Collection and/or remittance of such taxes to the relevant tax authority shall be the responsibility of the party who has the legal obligation to do so.

9. Warranty

9. 1. The Licensor warrants that it has, to the best of its knowledge, the rights to license reuse of the Licensed Material. **You are solely responsible for ensuring that the material you wish to license is original to the Licensor and does not carry the copyright of another entity or third party (as credited in the published version).** If the credit line on any part of the Licensed Material indicates that it was reprinted or adapted with permission from another source, then you should seek additional permission from that source to reuse the material.

9. 2. EXCEPT FOR THE EXPRESS WARRANTY STATED HEREIN AND TO THE EXTENT PERMITTED BY APPLICABLE LAW, LICENSOR PROVIDES THE LICENSED MATERIAL "AS IS" AND MAKES NO OTHER REPRESENTATION OR WARRANTY. LICENSOR EXPRESSLY DISCLAIMS ANY LIABILITY FOR ANY CLAIM ARISING FROM OR OUT OF THE CONTENT, INCLUDING BUT NOT LIMITED TO ANY ERRORS, INACCURACIES, OMISSIONS, OR DEFECTS CONTAINED THEREIN, AND ANY IMPLIED OR EXPRESS WARRANTY AS TO MERCHANTABILITY OR FITNESS FOR A PARTICULAR PURPOSE. IN NO EVENT SHALL LICENSOR BE LIABLE TO YOU OR ANY OTHER PARTY OR ANY OTHER PERSON OR FOR ANY SPECIAL, CONSEQUENTIAL, INCIDENTAL, INDIRECT, PUNITIVE, OR EXEMPLARY DAMAGES, HOWEVER CAUSED, ARISING OUT OF OR IN CONNECTION WITH THE DOWNLOADING, VIEWING OR USE OF THE LICENSED MATERIAL REGARDLESS OF THE FORM OF ACTION, WHETHER FOR BREACH OF CONTRACT, BREACH OF WARRANTY, TORT, NEGLIGENCE, INFRINGEMENT OR OTHERWISE (INCLUDING, WITHOUT LIMITATION, DAMAGES BASED ON LOSS OF PROFITS, DATA, FILES, USE, BUSINESS OPPORTUNITY OR CLAIMS OF THIRD PARTIES), AND WHETHER OR NOT THE PARTY HAS BEEN ADVISED OF THE POSSIBILITY OF SUCH DAMAGES. THIS LIMITATION APPLIES NOTWITHSTANDING ANY FAILURE OF ESSENTIAL PURPOSE OF ANY LIMITED REMEDY PROVIDED HEREIN.

10. Termination and Cancellation

10. 1. The License and all rights granted hereunder will continue until the end of the applicable period shown in Clause 5.1 above. Thereafter, this license will be terminated and all rights granted hereunder will cease.

10. 2. Licensor reserves the right to terminate the License in the event that payment is not received in full or if you breach the terms of this License.

11. General

11. 1. The License and the rights and obligations of the parties hereto shall be construed, interpreted and determined in accordance with the laws of the Federal

Republic of Germany without reference to the stipulations of the CISG (United Nations Convention on Contracts for the International Sale of Goods) or to Germany´s choice-of-law principle.

11. 2. The parties acknowledge and agree that any controversies and disputes arising out of this License shall be decided exclusively by the courts of or having jurisdiction for Heidelberg, Germany, as far as legally permissible.

11. 3. This License is solely for Licensor's and Licensee's benefit. It is not for the benefit of any other person or entity.

Questions? For questions on Copyright Clearance Center accounts or website issues please contact springernaturesupport@copyright.com or +1-855-239-3415 (toll free in the US) or +1-978-646-2777. For questions on Springer Nature licensing please visit https://www.springernature.com/gp/partners/rights-permissions-third-party-distribution

Other Conditions:

Version 1.4 - Dec 2022

Questions? customercare@copyright.com.

Marketplace

Order Date	25-Jan-2023	**Type of Use**	Republish in a thesis/dissertation
Order License ID	1315687-1		
ISSN	1947-5462	**Publisher**	Annual Reviews
		Portion	Image/photo/illustration

LICENSED CONTENT

Publication Title	Annual review of condensed matter physics	**Rightsholder**	Annual Reviews, Inc.
		Publication Type	Journal
Date	01/01/2010	**URL**	http://www.annualreviews.org/journal/conmatphys
Language	English		
Country	United States of America		

REQUEST DETAILS

Portion Type	Image/photo/illustration	**Distribution**	Worldwide
Number of Images / Photos / Illustrations	1	**Translation**	Original language of publication
Format (select all that apply)	Electronic	**Copies for the Disabled?**	No
		Minor Editing Privileges?	No
Who Will Republish the Content?	Academic institution	**Incidental Promotional Use?**	No
Duration of Use	Life of current edition	**Currency**	GBP
Lifetime Unit Quantity	Up to 499		
Rights Requested	Main product		

NEW WORK DETAILS

Title	Emergent dynamics of confluent tissues in homeostasis and growth	**Institution Name**	Imperial College London
		Expected Presentation Date	2023-03-31
Instructor Name	Andrew Killeen		

ADDITIONAL DETAILS

Order Reference Number	N/A	**The Requesting Person/Organization to Appear on the License**	Andrew Killeen

REQUESTED CONTENT DETAILS

Title, Description or Numeric Reference of the Portion(s)	Figure 2	**Title of the Article/Chapter the Portion Is From**	Physical Models of Collective Cell Migration
Editor of Portion(s)	N/A	**Author of Portion(s)**	Ricard Alert, Xavier Trepat

Volume of Serial or Monograph	11	**Issue, if Republishing an Article From a Serial**	1
Page or Page Range of Portion	5	**Publication Date of Portion**	2019-09-27

Marketplace Permissions General Terms and Conditions

The following terms and conditions ("General Terms"), together with any applicable Publisher Terms and Conditions, govern User's use of Works pursuant to the Licenses granted by Copyright Clearance Center, Inc. ("CCC") on behalf of the applicable Rightsholders of such Works through CCC's applicable Marketplace transactional licensing services (each, a "Service").

1) **Definitions.** For purposes of these General Terms, the following definitions apply:

"License" is the licensed use the User obtains via the Marketplace platform in a particular licensing transaction, as set forth in the Order Confirmation.

"Order Confirmation" is the confirmation CCC provides to the User at the conclusion of each Marketplace transaction. "Order Confirmation Terms" are additional terms set forth on specific Order Confirmations not set forth in the General Terms that can include terms applicable to a particular CCC transactional licensing service and/or any Rightsholder-specific terms.

"Rightsholder(s)" are the holders of copyright rights in the Works for which a User obtains licenses via the Marketplace platform, which are displayed on specific Order Confirmations.

"Terms" means the terms and conditions set forth in these General Terms and any additional Order Confirmation Terms collectively.

"User" or "you" is the person or entity making the use granted under the relevant License. Where the person accepting the Terms on behalf of a User is a freelancer or other third party who the User authorized to accept the General Terms on the User's behalf, such person shall be deemed jointly a User for purposes of such Terms.

"Work(s)" are the copyright protected works described in relevant Order Confirmations.

2) **Description of Service.** CCC's Marketplace enables Users to obtain Licenses to use one or more Works in accordance with all relevant Terms. CCC grants Licenses as an agent on behalf of the copyright rightsholder identified in the relevant Order Confirmation.

3) **Applicability of Terms.** The Terms govern User's use of Works in connection with the relevant License. In the event of any conflict between General Terms and Order Confirmation Terms, the latter shall govern. User acknowledges that Rightsholders have complete discretion whether to grant any permission, and whether to place any limitations on any grant, and that CCC has no right to supersede or to modify any such discretionary act by a Rightsholder.

4) **Representations; Acceptance.** By using the Service, User represents and warrants that User has been duly authorized by the User to accept, and hereby does accept, all Terms.

5) **Scope of License; Limitations and Obligations.** All Works and all rights therein, including copyright rights, remain the sole and exclusive property of the Rightsholder. The License provides only those rights expressly set forth in the terms and conveys no other rights in any Works

6) **General Payment Terms.** User may pay at time of checkout by credit card or choose to be invoiced. If the User chooses to be invoiced, the User shall: (i) remit payments in the manner identified on specific invoices, (ii) unless otherwise specifically stated in an Order Confirmation or separate written agreement, Users shall remit payments upon receipt of the relevant invoice from CCC, either by delivery or notification of availability of the invoice via the Marketplace platform, and (iii) if the User does not pay the invoice within 30 days of receipt, the User may incur a service charge of 1.5% per month or the maximum rate allowed by applicable law, whichever is less. While User may exercise the rights in the License immediately upon receiving the Order Confirmation, the License is automatically revoked and is null and void, as if it had never been issued, if CCC does not receive complete payment on a timely basis.

7) **General Limits on Use.** Unless otherwise provided in the Order Confirmation, any grant of rights to User (i) involves only the rights set forth in the Terms and does not include subsequent or additional uses, (ii) is non-exclusive and non-transferable, and (iii) is subject to any and all limitations and restrictions (such as, but not limited to, limitations on duration of use or circulation) included in the Terms. Upon completion of the licensed use as set forth in the Order Confirmation, User shall either secure a new permission for further use of the Work(s) or immediately cease any new use of the Work(s) and shall render inaccessible (such as by deleting or by removing or severing links or other locators) any further copies of the Work. User may only make alterations to the Work if and as expressly set forth in the Order

Confirmation. No Work may be used in any way that is unlawful, including without limitation if such use would violate applicable sanctions laws or regulations, would be defamatory, violate the rights of third parties (including such third parties' rights of copyright, privacy, publicity, or other tangible or intangible property), or is otherwise illegal, sexually explicit, or obscene. In addition, User may not conjoin a Work with any other material that may result in damage to the reputation of the Rightsholder. Any unlawful use will render any licenses hereunder null and void. User agrees to inform CCC if it becomes aware of any infringement of any rights in a Work and to cooperate with any reasonable request of CCC or the Rightsholder in connection therewith.

8) **Third Party Materials.** In the event that the material for which a License is sought includes third party materials (such as photographs, illustrations, graphs, inserts and similar materials) that are identified in such material as having been used by permission (or a similar indicator), User is responsible for identifying, and seeking separate licenses (under this Service, if available, or otherwise) for any of such third party materials; without a separate license, User may not use such third party materials via the License.

9) **Copyright Notice.** Use of proper copyright notice for a Work is required as a condition of any License granted under the Service. Unless otherwise provided in the Order Confirmation, a proper copyright notice will read substantially as follows: "Used with permission of [Rightsholder's name], from [Work's title, author, volume, edition number and year of copyright]; permission conveyed through Copyright Clearance Center, Inc." Such notice must be provided in a reasonably legible font size and must be placed either on a cover page or in another location that any person, upon gaining access to the material which is the subject of a permission, shall see, or in the case of republication Licenses, immediately adjacent to the Work as used (for example, as part of a by-line or footnote) or in the place where substantially all other credits or notices for the new work containing the republished Work are located. Failure to include the required notice results in loss to the Rightsholder and CCC, and the User shall be liable to pay liquidated damages for each such failure equal to twice the use fee specified in the Order Confirmation, in addition to the use fee itself and any other fees and charges specified.

10) **Indemnity.** User hereby indemnifies and agrees to defend the Rightsholder and CCC, and their respective employees and directors, against all claims, liability, damages, costs, and expenses, including legal fees and expenses, arising out of any use of a Work beyond the scope of the rights granted herein and in the Order Confirmation, or any use of a Work which has been altered in any unauthorized way by User, including claims of defamation or infringement of rights of copyright, publicity, privacy, or other tangible or intangible property.

11) **Limitation of Liability.** UNDER NO CIRCUMSTANCES WILL CCC OR THE RIGHTSHOLDER BE LIABLE FOR ANY DIRECT, INDIRECT, CONSEQUENTIAL, OR INCIDENTAL DAMAGES (INCLUDING WITHOUT LIMITATION DAMAGES FOR LOSS OF BUSINESS PROFITS OR INFORMATION, OR FOR BUSINESS INTERRUPTION) ARISING OUT OF THE USE OR INABILITY TO USE A WORK, EVEN IF ONE OR BOTH OF THEM HAS BEEN ADVISED OF THE POSSIBILITY OF SUCH DAMAGES. In any event, the total liability of the Rightsholder and CCC (including their respective employees and directors) shall not exceed the total amount actually paid by User for the relevant License. User assumes full liability for the actions and omissions of its principals, employees, agents, affiliates, successors, and assigns.

12) **Limited Warranties.** THE WORK(S) AND RIGHT(S) ARE PROVIDED "AS IS." CCC HAS THE RIGHT TO GRANT TO USER THE RIGHTS GRANTED IN THE ORDER CONFIRMATION DOCUMENT. CCC AND THE RIGHTSHOLDER DISCLAIM ALL OTHER WARRANTIES RELATING TO THE WORK(S) AND RIGHT(S), EITHER EXPRESS OR IMPLIED, INCLUDING WITHOUT LIMITATION IMPLIED WARRANTIES OF MERCHANTABILITY OR FITNESS FOR A PARTICULAR PURPOSE. ADDITIONAL RIGHTS MAY BE REQUIRED TO USE ILLUSTRATIONS, GRAPHS, PHOTOGRAPHS, ABSTRACTS, INSERTS, OR OTHER PORTIONS OF THE WORK (AS OPPOSED TO THE ENTIRE WORK) IN A MANNER CONTEMPLATED BY USER; USER UNDERSTANDS AND AGREES THAT NEITHER CCC NOR THE RIGHTSHOLDER MAY HAVE SUCH ADDITIONAL RIGHTS TO GRANT.

13) **Effect of Breach.** Any failure by User to pay any amount when due, or any use by User of a Work beyond the scope of the License set forth in the Order Confirmation and/or the Terms, shall be a material breach of such License. Any breach not cured within 10 days of written notice thereof shall result in immediate termination of such License without further notice. Any unauthorized (but licensable) use of a Work that is terminated immediately upon notice thereof may be liquidated by payment of the Rightsholder's ordinary license price therefor; any unauthorized (and unlicensable) use that is not terminated immediately for any reason (including, for example, because materials containing the Work cannot reasonably be recalled) will be subject to all remedies available at law or in equity, but in no event to a payment of less than three times the Rightsholder's ordinary license price for the most closely analogous licensable use plus Rightsholder's and/or CCC's costs and expenses incurred in collecting such payment.

14) **Additional Terms for Specific Products and Services.** If a User is making one of the uses described in this Section 14, the additional terms and conditions apply:

a) ***Print Uses of Academic Course Content and Materials (photocopies for academic coursepacks or classroom handouts).*** For photocopies for academic coursepacks or classroom handouts the following additional terms apply:

i) The copies and anthologies created under this License may be made and assembled by faculty members individually or at their request by on-campus bookstores or copy centers, or by off-campus copy shops and other similar entities.

ii) No License granted shall in any way: (i) include any right by User to create a substantively non-identical copy of the Work or to edit or in any other way modify the Work (except by means of deleting material immediately preceding or following the entire portion of the Work copied) (ii) permit "publishing ventures" where any particular anthology would be systematically marketed at multiple institutions.

iii) Subject to any Publisher Terms (and notwithstanding any apparent contradiction in the Order Confirmation arising from data provided by User), any use authorized under the academic pay-per-use service is limited as follows:

A) any License granted shall apply to only one class (bearing a unique identifier as assigned by the institution, and thereby including all sections or other subparts of the class) at one institution;

B) use is limited to not more than 25% of the text of a book or of the items in a published collection of essays, poems or articles;

C) use is limited to no more than the greater of (a) 25% of the text of an issue of a journal or other periodical or (b) two articles from such an issue;

D) no User may sell or distribute any particular anthology, whether photocopied or electronic, at more than one institution of learning;

E) in the case of a photocopy permission, no materials may be entered into electronic memory by User except in order to produce an identical copy of a Work before or during the academic term (or analogous period) as to which any particular permission is granted. In the event that User shall choose to retain materials that are the subject of a photocopy permission in electronic memory for purposes of producing identical copies more than one day after such retention (but still within the scope of any permission granted), User must notify CCC of such fact in the applicable permission request and such retention shall constitute one copy actually sold for purposes of calculating permission fees due; and

F) any permission granted shall expire at the end of the class. No permission granted shall in any way include any right by User to create a substantively non-identical copy of the Work or to edit or in any other way modify the Work (except by means of deleting material immediately preceding or following the entire portion of the Work copied).

iv) Books and Records; Right to Audit. As to each permission granted under the academic pay-per-use Service, User shall maintain for at least four full calendar years books and records sufficient for CCC to determine the numbers of copies made by User under such permission. CCC and any representatives it may designate shall have the right to audit such books and records at any time during User's ordinary business hours, upon two days' prior notice. If any such audit shall determine that User shall have underpaid for, or underreported, any photocopies sold or by three percent (3%) or more, then User shall bear all the costs of any such audit; otherwise, CCC shall bear the costs of any such audit. Any amount determined by such audit to have been underpaid by User shall immediately be paid to CCC by User, together with interest thereon at the rate of 10% per annum from the date such amount was originally due. The provisions of this paragraph shall survive the termination of this License for any reason.

b) ***Digital Pay-Per-Uses of Academic Course Content and Materials (e-coursepacks, electronic reserves, learning management systems, academic institution intranets).*** For uses in e-coursepacks, posts in electronic reserves, posts in learning management systems, or posts on academic institution intranets, the following additional terms apply:

i) The pay-per-uses subject to this Section 14(b) include:

A) **Posting e-reserves, course management systems, e-coursepacks for text-based content,** which grants authorizations to import requested material in electronic format, and allows electronic access to this material to members of a designated college or university class, under the direction of an instructor designated by the college or university, accessible only under appropriate electronic controls (e.g., password);

B) **Posting e-reserves, course management systems, e-coursepacks for material consisting of photographs or other still images not embedded in text,** which grants not only the authorizations described in Section 14(b)(i)(A) above, but also the following authorization: to include the requested material in course materials for use consistent with Section 14(b)(i)(A) above, including any necessary resizing, reformatting or modification of the resolution of such requested material (provided that such modification does not alter the underlying editorial content or meaning of the requested material, and provided that the resulting modified content is used solely within the scope of, and in a manner consistent with, the particular authorization described in the Order Confirmation and the Terms), but not including any other form of manipulation, alteration or editing of the requested material;

C) **Posting e-reserves, course management systems, e-coursepacks or other academic distribution for audiovisual content,** which grants not only the authorizations described in Section 14(b)(i)(A) above, but also

the following authorizations: (i) to include the requested material in course materials for use consistent with Section 14(b)(i)(A) above; (ii) to display and perform the requested material to such members of such class in the physical classroom or remotely by means of streaming media or other video formats; and (iii) to "clip" or reformat the requested material for purposes of time or content management or ease of delivery, provided that such “clipping” or reformatting does not alter the underlying editorial content or meaning of the requested material and that the resulting material is used solely within the scope of, and in a manner consistent with, the particular authorization described in the Order Confirmation and the Terms. Unless expressly set forth in the relevant Order Conformation, the License does not authorize any other form of manipulation, alteration or editing of the requested material.

ii) Unless expressly set forth in the relevant Order Confirmation, no License granted shall in any way: (i) include any right by User to create a substantively non-identical copy of the Work or to edit or in any other way modify the Work (except by means of deleting material immediately preceding or following the entire portion of the Work copied or, in the case of Works subject to Sections 14(b)(1)(B) or (C) above, as described in such Sections) (ii) permit "publishing ventures" where any particular course materials would be systematically marketed at multiple institutions.

iii) Subject to any further limitations determined in the Rightsholder Terms (and notwithstanding any apparent contradiction in the Order Confirmation arising from data provided by User), any use authorized under the electronic course content pay-per-use service is limited as follows:

A) any License granted shall apply to only one class (bearing a unique identifier as assigned by the institution, and thereby including all sections or other subparts of the class) at one institution;

B) use is limited to not more than 25% of the text of a book or of the items in a published collection of essays, poems or articles;

C) use is limited to not more than the greater of (a) 25% of the text of an issue of a journal or other periodical or (b) two articles from such an issue;

D) no User may sell or distribute any particular materials, whether photocopied or electronic, at more than one institution of learning;

E) electronic access to material which is the subject of an electronic-use permission must be limited by means of electronic password, student identification or other control permitting access solely to students and instructors in the class;

F) User must ensure (through use of an electronic cover page or other appropriate means) that any person, upon gaining electronic access to the material, which is the subject of a permission, shall see:

- a proper copyright notice, identifying the Rightsholder in whose name CCC has granted permission,
- a statement to the effect that such copy was made pursuant to permission,
- a statement identifying the class to which the material applies and notifying the reader that the material has been made available electronically solely for use in the class, and
- a statement to the effect that the material may not be further distributed to any person outside the class, whether by copying or by transmission and whether electronically or in paper form, and User must also ensure that such cover page or other means will print out in the event that the person accessing the material chooses to print out the material or any part thereof.

G) any permission granted shall expire at the end of the class and, absent some other form of authorization, User is thereupon required to delete the applicable material from any electronic storage or to block electronic access to the applicable material.

iv) Uses of separate portions of a Work, even if they are to be included in the same course material or the same university or college class, require separate permissions under the electronic course content pay-per-use Service. Unless otherwise provided in the Order Confirmation, any grant of rights to User is limited to use completed no later than the end of the academic term (or analogous period) as to which any particular permission is granted.

v) Books and Records; Right to Audit. As to each permission granted under the electronic course content Service, User shall maintain for at least four full calendar years books and records sufficient for CCC to determine the numbers of copies made by User under such permission. CCC and any representatives it may designate shall have the right to audit such books and records at any time during User's ordinary business hours, upon two days' prior notice. If any such audit shall determine that User shall have underpaid for, or underreported, any electronic copies used by three percent (3%) or more, then User shall bear all the costs of any such audit; otherwise, CCC

shall bear the costs of any such audit. Any amount determined by such audit to have been underpaid by User shall immediately be paid to CCC by User, together with interest thereon at the rate of 10% per annum from the date such amount was originally due. The provisions of this paragraph shall survive the termination of this license for any reason.

c) ***Pay-Per-Use Permissions for Certain Reproductions (Academic photocopies for library reserves and interlibrary loan reporting) (Non-academic internal/external business uses and commercial document delivery).*** The License expressly excludes the uses listed in Section (c)(i)-(v) below (which must be subject to separate license from the applicable Rightsholder) for: academic photocopies for library reserves and interlibrary loan reporting; and non-academic internal/external business uses and commercial document delivery.

i) electronic storage of any reproduction (whether in plain-text, PDF, or any other format) other than on a transitory basis;

ii) the input of Works or reproductions thereof into any computerized database;

iii) reproduction of an entire Work (cover-to-cover copying) except where the Work is a single article;

iv) reproduction for resale to anyone other than a specific customer of User;

v) republication in any different form. Please obtain authorizations for these uses through other CCC services or directly from the rightsholder.

Any license granted is further limited as set forth in any restrictions included in the Order Confirmation and/or in these Terms.

d) ***Electronic Reproductions in Online Environments (Non-Academic-email, intranet, internet and extranet).*** For "electronic reproductions", which generally includes e-mail use (including instant messaging or other electronic transmission to a defined group of recipients) or posting on an intranet, extranet or Intranet site (including any display or performance incidental thereto), the following additional terms apply:

i) Unless otherwise set forth in the Order Confirmation, the License is limited to use completed within 30 days for any use on the Internet, 60 days for any use on an intranet or extranet and one year for any other use, all as measured from the "republication date" as identified in the Order Confirmation, if any, and otherwise from the date of the Order Confirmation.

ii) User may not make or permit any alterations to the Work, unless expressly set forth in the Order Confirmation (after request by User and approval by Rightsholder); provided, however, that a Work consisting of photographs or other still images not embedded in text may, if necessary, be resized, reformatted or have its resolution modified without additional express permission, and a Work consisting of audiovisual content may, if necessary, be "clipped" or reformatted for purposes of time or content management or ease of delivery (provided that any such resizing, reformatting, resolution modification or “clipping” does not alter the underlying editorial content or meaning of the Work used, and that the resulting material is used solely within the scope of, and in a manner consistent with, the particular License described in the Order Confirmation and the Terms.

15) **Miscellaneous.**

a) User acknowledges that CCC may, from time to time, make changes or additions to the Service or to the Terms, and that Rightsholder may make changes or additions to the Rightsholder Terms. Such updated Terms will replace the prior terms and conditions in the order workflow and shall be effective as to any subsequent Licenses but shall not apply to Licenses already granted and paid for under a prior set of terms.

b) Use of User-related information collected through the Service is governed by CCC's privacy policy, available online at www.copyright.com/about/privacy-policy/.

c) The License is personal to User. Therefore, User may not assign or transfer to any other person (whether a natural person or an organization of any kind) the License or any rights granted thereunder; provided, however, that, where applicable, User may assign such License in its entirety on written notice to CCC in the event of a transfer of all or substantially all of User's rights in any new material which includes the Work(s) licensed under this Service.

d) No amendment or waiver of any Terms is binding unless set forth in writing and signed by the appropriate parties, including, where applicable, the Rightsholder. The Rightsholder and CCC hereby object to any terms contained in any writing prepared by or on behalf of the User or its principals, employees, agents or affiliates and purporting to govern or otherwise relate to the License described in the Order Confirmation, which terms are in any way inconsistent with any Terms set forth in the Order Confirmation, and/or in CCC's standard operating procedures, whether such writing is prepared prior to, simultaneously with or subsequent to the Order Confirmation, and whether such writing appears on a copy of the Order Confirmation or in a separate instrument.

e) The License described in the Order Confirmation shall be governed by and construed under the law of the State of New York, USA, without regard to the principles thereof of conflicts of law. Any case, controversy, suit, action, or proceeding arising out of, in connection with, or related to such License shall be brought, at CCC's sole discretion, in any federal or state court located in the County of New York, State of New York, USA, or in any federal or state court whose geographical jurisdiction covers the location of the Rightsholder set forth in the Order Confirmation. The parties expressly submit to the personal jurisdiction and venue of each such federal or state court.

Last updated October 2022

SPRINGER NATURE LICENSE
TERMS AND CONDITIONS

Feb 13, 2023

This Agreement between Imperial College London -- Andrew Killeen ("You") and Springer Nature ("Springer Nature") consists of your license details and the terms and conditions provided by Springer Nature and Copyright Clearance Center.

License Number	5475860856248
License date	Jan 25, 2023
Licensed Content Publisher	Springer Nature
Licensed Content Publication	Nature Physics
Licensed Content Title	Topological defects in confined populations of spindle-shaped cells
Licensed Content Author	Guillaume Duclos et al
Licensed Content Date	Sep 12, 2016
Type of Use	Thesis/Dissertation
Requestor type	academic/university or research institute
Format	electronic
Portion	figures/tables/illustrations
Number of figures/tables/illustrations	1
High-res required	no
Will you be translating?	no

Circulation/distribution	1 - 29
Author of this Springer Nature content	no
Title	Emergent dynamics of confluent tissues in homeostasis and growth
Institution name	Imperial College London
Expected presentation date	Mar 2023
Portions	Figure 2a
Requestor Location	Imperial College London 47a Kingsgate Road London, other NW6 4TD United Kingdom Attn: Imperial College London
Total	0.00 GBP

Terms and Conditions

Springer Nature Customer Service Centre GmbH Terms and Conditions

The following terms and conditions ("Terms and Conditions") together with the terms specified in your [RightsLink] constitute the License ("License") between you as Licensee and Springer Nature Customer Service Centre GmbH as Licensor. By clicking 'accept' and completing the transaction for your use of the material ("Licensed Material"), you confirm your acceptance of and obligation to be bound by these Terms and Conditions.

1. Grant and Scope of License

1. 1. The Licensor grants you a personal, non-exclusive, non-transferable, non-sublicensable, revocable, world-wide License to reproduce, distribute, communicate to the public, make available, broadcast, electronically transmit or create derivative works using the Licensed Material for the purpose(s) specified in your RightsLink Licence Details only. Licenses are granted for the specific use requested in the order and for no other use, subject to these Terms and Conditions. You acknowledge and agree that the rights granted to you under this License do not include the right to modify, edit, translate, include in collective works, or create derivative works of the Licensed Material in whole or in part unless expressly stated in your RightsLink Licence Details. You may use the Licensed Material only as permitted under this Agreement and will not reproduce, distribute, display, perform, or otherwise use or exploit any Licensed Material in any way, in whole or in part, except as expressly

permitted by this License.

1. 2. You may only use the Licensed Content in the manner and to the extent permitted by these Terms and Conditions, by your RightsLink Licence Details and by any applicable laws.

1. 3. A separate license may be required for any additional use of the Licensed Material, e.g. where a license has been purchased for print use only, separate permission must be obtained for electronic re-use. Similarly, a License is only valid in the language selected and does not apply for editions in other languages unless additional translation rights have been granted separately in the License.

1. 4. Any content within the Licensed Material that is owned by third parties is expressly excluded from the License.

1. 5. Rights for additional reuses such as custom editions, computer/mobile applications, film or TV reuses and/or any other derivative rights requests require additional permission and may be subject to an additional fee. Please apply to journalpermissions@springernature.com or bookpermissions@springernature.com for these rights.

2. Reservation of Rights

Licensor reserves all rights not expressly granted to you under this License. You acknowledge and agree that nothing in this License limits or restricts Licensor's rights in or use of the Licensed Material in any way. Neither this License, nor any act, omission, or statement by Licensor or you, conveys any ownership right to you in any Licensed Material, or to any element or portion thereof. As between Licensor and you, Licensor owns and retains all right, title, and interest in and to the Licensed Material subject to the license granted in Section 1.1. Your permission to use the Licensed Material is expressly conditioned on you not impairing Licensor's or the applicable copyright owner's rights in the Licensed Material in any way.

3. Restrictions on use

3. 1. Minor editing privileges are allowed for adaptations for stylistic purposes or formatting purposes provided such alterations do not alter the original meaning or intention of the Licensed Material and the new figure(s) are still accurate and representative of the Licensed Material. Any other changes including but not limited to, cropping, adapting, and/or omitting material that affect the meaning, intention or moral rights of the author(s) are strictly prohibited.

3. 2. You must not use any Licensed Material as part of any design or trademark.

3. 3. Licensed Material may be used in Open Access Publications (OAP), but any such reuse must include a clear acknowledgment of this permission visible at the same time as the figures/tables/illustration or abstract and which must indicate that the Licensed Material is not part of the governing OA license but has been reproduced with permission. This may be indicated according to any standard referencing system but must include at a minimum 'Book/Journal title, Author, Journal Name (if applicable), Volume (if applicable), Publisher, Year, reproduced with permission from SNCSC'.

4. STM Permission Guidelines

4. 1. An alternative scope of license may apply to signatories of the STM Permissions Guidelines ("STM PG") as amended from time to time and made available at https://www.stm-assoc.org/intellectual-property/permissions/permissions-guidelines/.

4. 2. For content reuse requests that qualify for permission under the STM PG, and which may be updated from time to time, the STM PG supersede the terms and conditions contained in this License.

4. 3. If a License has been granted under the STM PG, but the STM PG no longer apply at the time of publication, further permission must be sought from the Rightsholder. Contact journalpermissions@springernature.com or bookpermissions@springernature.com for these rights.

5. Duration of License

5. 1. Unless otherwise indicated on your License, a License is valid from the date of purchase ("License Date") until the end of the relevant period in the below table:

Reuse in a medical communications project	Reuse up to distribution or time period indicated in License
Reuse in a dissertation/thesis	Lifetime of thesis
Reuse in a journal/magazine	Lifetime of journal/magazine
Reuse in a book/textbook	Lifetime of edition
Reuse on a website	1 year unless otherwise specified in the License
Reuse in a presentation/slide kit/poster	Lifetime of presentation/slide kit/poster. Note: publication whether electronic or in print of presentation/slide kit/poster may require further permission.
Reuse in conference proceedings	Lifetime of conference proceedings
Reuse in an annual report	Lifetime of annual report
Reuse in training/CME materials	Reuse up to distribution or time period indicated in License
Reuse in newsmedia	Lifetime of newsmedia
Reuse in coursepack/classroom materials	Reuse up to distribution and/or time period indicated in license

6. Acknowledgement

6. 1. The Licensor's permission must be acknowledged next to the Licensed Material in print. In electronic form, this acknowledgement must be visible at the same time as the figures/tables/illustrations or abstract and must be hyperlinked to the journal/book's homepage.

6. 2. Acknowledgement may be provided according to any standard referencing system and at a minimum should include "Author, Article/Book Title, Journal name/Book imprint, volume, page number, year, Springer Nature".

7. Reuse in a dissertation or thesis

7. 1. Where 'reuse in a dissertation/thesis' has been selected, the following terms apply: Print rights of the Version of Record are provided for; electronic rights for use only on institutional repository as defined by the Sherpa guideline (www.sherpa.ac.uk/romeo/) and only up to what is required by the awarding institution.

7. 2. For theses published under an ISBN or ISSN, separate permission is required. Please contact journalpermissions@springernature.com or bookpermissions@springernature.com for these rights.

7. 3. Authors must properly cite the published manuscript in their thesis according to current citation standards and include the following acknowledgement: '*Reproduced with permission from Springer Nature*'.

8. License Fee

You must pay the fee set forth in the License Agreement (the "License Fees"). All amounts payable by you under this License are exclusive of any sales, use, withholding, value added or similar taxes, government fees or levies or other assessments. Collection and/or remittance of such taxes to the relevant tax authority shall be the responsibility of the party who has the legal obligation to do so.

9. Warranty

9. 1. The Licensor warrants that it has, to the best of its knowledge, the rights to license reuse of the Licensed Material. **You are solely responsible for ensuring that the material you wish to license is original to the Licensor and does not carry the copyright of another entity or third party (as credited in the published version).** If the credit line on any part of the Licensed Material indicates that it was reprinted or adapted with permission from another source, then you should seek additional permission from that source to reuse the material.

9. 2. EXCEPT FOR THE EXPRESS WARRANTY STATED HEREIN AND TO THE EXTENT PERMITTED BY APPLICABLE LAW, LICENSOR PROVIDES THE LICENSED MATERIAL "AS IS" AND MAKES NO OTHER REPRESENTATION OR WARRANTY. LICENSOR EXPRESSLY DISCLAIMS ANY LIABILITY FOR ANY CLAIM ARISING FROM OR OUT OF THE CONTENT, INCLUDING BUT NOT LIMITED TO ANY ERRORS, INACCURACIES, OMISSIONS, OR DEFECTS CONTAINED THEREIN, AND ANY IMPLIED OR EXPRESS WARRANTY AS TO MERCHANTABILITY OR FITNESS FOR A PARTICULAR PURPOSE. IN NO EVENT SHALL LICENSOR BE LIABLE TO YOU OR ANY OTHER PARTY OR ANY OTHER PERSON OR FOR ANY SPECIAL, CONSEQUENTIAL, INCIDENTAL, INDIRECT, PUNITIVE, OR EXEMPLARY DAMAGES, HOWEVER CAUSED, ARISING OUT OF OR IN CONNECTION WITH THE DOWNLOADING, VIEWING OR USE OF THE LICENSED MATERIAL REGARDLESS OF THE FORM OF ACTION, WHETHER FOR BREACH OF CONTRACT, BREACH OF WARRANTY, TORT, NEGLIGENCE, INFRINGEMENT OR OTHERWISE (INCLUDING, WITHOUT LIMITATION, DAMAGES BASED ON LOSS OF PROFITS, DATA, FILES, USE, BUSINESS OPPORTUNITY OR CLAIMS OF THIRD PARTIES), AND WHETHER OR NOT THE PARTY HAS BEEN ADVISED OF THE POSSIBILITY OF SUCH DAMAGES. THIS LIMITATION APPLIES NOTWITHSTANDING ANY FAILURE OF ESSENTIAL PURPOSE OF ANY LIMITED REMEDY PROVIDED HEREIN.

10. Termination and Cancellation

10. 1. The License and all rights granted hereunder will continue until the end of the applicable period shown in Clause 5.1 above. Thereafter, this license will be terminated and all rights granted hereunder will cease.

10. 2. Licensor reserves the right to terminate the License in the event that payment is not received in full or if you breach the terms of this License.

11. General

11. 1. The License and the rights and obligations of the parties hereto shall be construed, interpreted and determined in accordance with the laws of the Federal Republic of Germany without reference to the stipulations of the CISG (United Nations Convention on Contracts for the International Sale of Goods) or to Germany´s choice-of-law principle.

11. 2. The parties acknowledge and agree that any controversies and disputes arising out of this License shall be decided exclusively by the courts of or having jurisdiction for Heidelberg, Germany, as far as legally permissible.

11. 3. This License is solely for Licensor's and Licensee's benefit. It is not for the benefit of any other person or entity.

Questions? For questions on Copyright Clearance Center accounts or website issues please contact springernaturesupport@copyright.com or +1-855-239-3415 (toll free in the US) or +1-978-646-2777. For questions on Springer Nature licensing please visit https://www.springernature.com/gp/partners/rights-permissions-third-party-distribution

Other Conditions:

Version 1.4 - Dec 2022

Questions? customercare@copyright.com.

SPRINGER NATURE LICENSE
TERMS AND CONDITIONS

Feb 13, 2023

This Agreement between Imperial College London -- Andrew Killeen ("You") and Springer Nature ("Springer Nature") consists of your license details and the terms and conditions provided by Springer Nature and Copyright Clearance Center.

License Number	5475861034437
License date	Jan 25, 2023
Licensed Content Publisher	Springer Nature
Licensed Content Publication	Nature
Licensed Content Title	Topological defects in epithelia govern cell death and extrusion
Licensed Content Author	Thuan Beng Saw et al
Licensed Content Date	Apr 13, 2017
Type of Use	Thesis/Dissertation
Requestor type	academic/university or research institute
Format	electronic
Portion	figures/tables/illustrations
Number of figures/tables/illustrations	1
High-res required	no
Will you be translating?	no

Circulation/distribution	1 - 29
Author of this Springer Nature content	no
Title	Emergent dynamics of confluent tissues in homeostasis and growth
Institution name	Imperial College London
Expected presentation date	Mar 2023
Portions	Figure 1a and 1e
Requestor Location	Imperial College London 47a Kingsgate Road London, other NW6 4TD United Kingdom Attn: Imperial College London
Total	0.00 GBP

Terms and Conditions

Springer Nature Customer Service Centre GmbH Terms and Conditions

The following terms and conditions ("Terms and Conditions") together with the terms specified in your [RightsLink] constitute the License ("License") between you as Licensee and Springer Nature Customer Service Centre GmbH as Licensor. By clicking 'accept' and completing the transaction for your use of the material ("Licensed Material"), you confirm your acceptance of and obligation to be bound by these Terms and Conditions.

1. Grant and Scope of License

1. 1. The Licensor grants you a personal, non-exclusive, non-transferable, non-sublicensable, revocable, world-wide License to reproduce, distribute, communicate to the public, make available, broadcast, electronically transmit or create derivative works using the Licensed Material for the purpose(s) specified in your RightsLink Licence Details only. Licenses are granted for the specific use requested in the order and for no other use, subject to these Terms and Conditions. You acknowledge and agree that the rights granted to you under this License do not include the right to modify, edit, translate, include in collective works, or create derivative works of the Licensed Material in whole or in part unless expressly stated in your RightsLink Licence Details. You may use the Licensed Material only as permitted under this Agreement and will not reproduce, distribute, display, perform, or otherwise use or exploit any Licensed Material in any way, in whole or in part, except as expressly

permitted by this License.

1. 2. You may only use the Licensed Content in the manner and to the extent permitted by these Terms and Conditions, by your RightsLink Licence Details and by any applicable laws.

1. 3. A separate license may be required for any additional use of the Licensed Material, e.g. where a license has been purchased for print use only, separate permission must be obtained for electronic re-use. Similarly, a License is only valid in the language selected and does not apply for editions in other languages unless additional translation rights have been granted separately in the License.

1. 4. Any content within the Licensed Material that is owned by third parties is expressly excluded from the License.

1. 5. Rights for additional reuses such as custom editions, computer/mobile applications, film or TV reuses and/or any other derivative rights requests require additional permission and may be subject to an additional fee. Please apply to journalpermissions@springernature.com or bookpermissions@springernature.com for these rights.

2. Reservation of Rights

Licensor reserves all rights not expressly granted to you under this License. You acknowledge and agree that nothing in this License limits or restricts Licensor's rights in or use of the Licensed Material in any way. Neither this License, nor any act, omission, or statement by Licensor or you, conveys any ownership right to you in any Licensed Material, or to any element or portion thereof. As between Licensor and you, Licensor owns and retains all right, title, and interest in and to the Licensed Material subject to the license granted in Section 1.1. Your permission to use the Licensed Material is expressly conditioned on you not impairing Licensor's or the applicable copyright owner's rights in the Licensed Material in any way.

3. Restrictions on use

3. 1. Minor editing privileges are allowed for adaptations for stylistic purposes or formatting purposes provided such alterations do not alter the original meaning or intention of the Licensed Material and the new figure(s) are still accurate and representative of the Licensed Material. Any other changes including but not limited to, cropping, adapting, and/or omitting material that affect the meaning, intention or moral rights of the author(s) are strictly prohibited.

3. 2. You must not use any Licensed Material as part of any design or trademark.

3. 3. Licensed Material may be used in Open Access Publications (OAP), but any such reuse must include a clear acknowledgment of this permission visible at the same time as the figures/tables/illustration or abstract and which must indicate that the Licensed Material is not part of the governing OA license but has been reproduced with permission. This may be indicated according to any standard referencing system but must include at a minimum 'Book/Journal title, Author, Journal Name (if applicable), Volume (if applicable), Publisher, Year, reproduced with permission from SNCSC'.

4. STM Permission Guidelines

4. 1. An alternative scope of license may apply to signatories of the STM Permissions Guidelines ("STM PG") as amended from time to time and made available at https://www.stm-assoc.org/intellectual-property/permissions/permissions-guidelines/.

4. 2. For content reuse requests that qualify for permission under the STM PG, and which may be updated from time to time, the STM PG supersede the terms and conditions contained in this License.

4. 3. If a License has been granted under the STM PG, but the STM PG no longer apply at the time of publication, further permission must be sought from the Rightsholder. Contact journalpermissions@springernature.com or bookpermissions@springernature.com for these rights.

5. Duration of License

5. 1. Unless otherwise indicated on your License, a License is valid from the date of purchase ("License Date") until the end of the relevant period in the below table:

Reuse in a medical communications project	Reuse up to distribution or time period indicated in License
Reuse in a dissertation/thesis	Lifetime of thesis
Reuse in a journal/magazine	Lifetime of journal/magazine
Reuse in a book/textbook	Lifetime of edition
Reuse on a website	1 year unless otherwise specified in the License
Reuse in a presentation/slide kit/poster	Lifetime of presentation/slide kit/poster. Note: publication whether electronic or in print of presentation/slide kit/poster may require further permission.
Reuse in conference proceedings	Lifetime of conference proceedings
Reuse in an annual report	Lifetime of annual report
Reuse in training/CME materials	Reuse up to distribution or time period indicated in License
Reuse in newsmedia	Lifetime of newsmedia
Reuse in coursepack/classroom materials	Reuse up to distribution and/or time period indicated in license

6. Acknowledgement

6. 1. The Licensor's permission must be acknowledged next to the Licensed Material in print. In electronic form, this acknowledgement must be visible at the same time as the figures/tables/illustrations or abstract and must be hyperlinked to the journal/book's homepage.

6. 2. Acknowledgement may be provided according to any standard referencing system and at a minimum should include "Author, Article/Book Title, Journal name/Book imprint, volume, page number, year, Springer Nature".

7. Reuse in a dissertation or thesis

7. 1. Where 'reuse in a dissertation/thesis' has been selected, the following terms apply: Print rights of the Version of Record are provided for; electronic rights for use only on institutional repository as defined by the Sherpa guideline (www.sherpa.ac.uk/romeo/) and only up to what is required by the awarding institution.

7. 2. For theses published under an ISBN or ISSN, separate permission is required. Please contact journalpermissions@springernature.com or bookpermissions@springernature.com for these rights.

7. 3. Authors must properly cite the published manuscript in their thesis according to current citation standards and include the following acknowledgement: '*Reproduced with permission from Springer Nature*'.

8. License Fee

You must pay the fee set forth in the License Agreement (the "License Fees"). All amounts payable by you under this License are exclusive of any sales, use, withholding, value added or similar taxes, government fees or levies or other assessments. Collection and/or remittance of such taxes to the relevant tax authority shall be the responsibility of the party who has the legal obligation to do so.

9. Warranty

9. 1. The Licensor warrants that it has, to the best of its knowledge, the rights to license reuse of the Licensed Material. **You are solely responsible for ensuring that the material you wish to license is original to the Licensor and does not carry the copyright of another entity or third party (as credited in the published version).** If the credit line on any part of the Licensed Material indicates that it was reprinted or adapted with permission from another source, then you should seek additional permission from that source to reuse the material.

9. 2. EXCEPT FOR THE EXPRESS WARRANTY STATED HEREIN AND TO THE EXTENT PERMITTED BY APPLICABLE LAW, LICENSOR PROVIDES THE LICENSED MATERIAL "AS IS" AND MAKES NO OTHER REPRESENTATION OR WARRANTY. LICENSOR EXPRESSLY DISCLAIMS ANY LIABILITY FOR ANY CLAIM ARISING FROM OR OUT OF THE CONTENT, INCLUDING BUT NOT LIMITED TO ANY ERRORS, INACCURACIES, OMISSIONS, OR DEFECTS CONTAINED THEREIN, AND ANY IMPLIED OR EXPRESS WARRANTY AS TO MERCHANTABILITY OR FITNESS FOR A PARTICULAR PURPOSE. IN NO EVENT SHALL LICENSOR BE LIABLE TO YOU OR ANY OTHER PARTY OR ANY OTHER PERSON OR FOR ANY SPECIAL, CONSEQUENTIAL, INCIDENTAL, INDIRECT, PUNITIVE, OR EXEMPLARY DAMAGES, HOWEVER CAUSED, ARISING OUT OF OR IN CONNECTION WITH THE DOWNLOADING, VIEWING OR USE OF THE LICENSED MATERIAL REGARDLESS OF THE FORM OF ACTION, WHETHER FOR BREACH OF CONTRACT, BREACH OF WARRANTY, TORT, NEGLIGENCE, INFRINGEMENT OR OTHERWISE (INCLUDING, WITHOUT LIMITATION, DAMAGES BASED ON LOSS OF PROFITS, DATA, FILES, USE, BUSINESS OPPORTUNITY OR CLAIMS OF THIRD PARTIES), AND WHETHER OR NOT THE PARTY HAS BEEN ADVISED OF THE POSSIBILITY OF SUCH DAMAGES. THIS LIMITATION APPLIES NOTWITHSTANDING ANY FAILURE OF ESSENTIAL PURPOSE OF ANY LIMITED REMEDY PROVIDED HEREIN.

10. Termination and Cancellation

10. 1. The License and all rights granted hereunder will continue until the end of the applicable period shown in Clause 5.1 above. Thereafter, this license will be terminated and all rights granted hereunder will cease.

10. 2. Licensor reserves the right to terminate the License in the event that payment is not received in full or if you breach the terms of this License.

11. General

11. 1. The License and the rights and obligations of the parties hereto shall be construed, interpreted and determined in accordance with the laws of the Federal Republic of Germany without reference to the stipulations of the CISG (United Nations Convention on Contracts for the International Sale of Goods) or to Germany´s choice-of-law principle.

11. 2. The parties acknowledge and agree that any controversies and disputes arising out of this License shall be decided exclusively by the courts of or having jurisdiction for Heidelberg, Germany, as far as legally permissible.

11. 3. This License is solely for Licensor's and Licensee's benefit. It is not for the benefit of any other person or entity.

Questions? For questions on Copyright Clearance Center accounts or website issues please contact springernaturesupport@copyright.com or +1-855-239-3415 (toll free in the US) or +1-978-646-2777. For questions on Springer Nature licensing please visit https://www.springernature.com/gp/partners/rights-permissions-third-party-distribution

Other Conditions:

Version 1.4 - Dec 2022

Questions? customercare@copyright.com.

SPRINGER NATURE LICENSE
TERMS AND CONDITIONS

Feb 13, 2023

This Agreement between Imperial College London -- Andrew Killeen ("You") and Springer Nature ("Springer Nature") consists of your license details and the terms and conditions provided by Springer Nature and Copyright Clearance Center.

License Number	5475861249154
License date	Jan 25, 2023
Licensed Content Publisher	Springer Nature
Licensed Content Publication	Nature Physics
Licensed Content Title	Mechanical waves during tissue expansion
Licensed Content Author	Xavier Serra-Picamal et al
Licensed Content Date	Jul 8, 2012
Type of Use	Thesis/Dissertation
Requestor type	academic/university or research institute
Format	electronic
Portion	figures/tables/illustrations
Number of figures/tables/illustrations	1
High-res required	no
Will you be translating?	no

Circulation/distribution	1 - 29
Author of this Springer Nature content	no
Title	Emergent dynamics of confluent tissues in homeostasis and growth
Institution name	Imperial College London
Expected presentation date	Mar 2023
Portions	Figure 2a-f
Requestor Location	Imperial College London 47a Kingsgate Road London, other NW6 4TD United Kingdom Attn: Imperial College London
Total	0.00 GBP

Terms and Conditions

Springer Nature Customer Service Centre GmbH Terms and Conditions

The following terms and conditions ("Terms and Conditions") together with the terms specified in your [RightsLink] constitute the License ("License") between you as Licensee and Springer Nature Customer Service Centre GmbH as Licensor. By clicking 'accept' and completing the transaction for your use of the material ("Licensed Material"), you confirm your acceptance of and obligation to be bound by these Terms and Conditions.

1. Grant and Scope of License

1. 1. The Licensor grants you a personal, non-exclusive, non-transferable, non-sublicensable, revocable, world-wide License to reproduce, distribute, communicate to the public, make available, broadcast, electronically transmit or create derivative works using the Licensed Material for the purpose(s) specified in your RightsLink Licence Details only. Licenses are granted for the specific use requested in the order and for no other use, subject to these Terms and Conditions. You acknowledge and agree that the rights granted to you under this License do not include the right to modify, edit, translate, include in collective works, or create derivative works of the Licensed Material in whole or in part unless expressly stated in your RightsLink Licence Details. You may use the Licensed Material only as permitted under this Agreement and will not reproduce, distribute, display, perform, or otherwise use or exploit any Licensed Material in any way, in whole or in part, except as expressly

permitted by this License.

1. 2. You may only use the Licensed Content in the manner and to the extent permitted by these Terms and Conditions, by your RightsLink Licence Details and by any applicable laws.

1. 3. A separate license may be required for any additional use of the Licensed Material, e.g. where a license has been purchased for print use only, separate permission must be obtained for electronic re-use. Similarly, a License is only valid in the language selected and does not apply for editions in other languages unless additional translation rights have been granted separately in the License.

1. 4. Any content within the Licensed Material that is owned by third parties is expressly excluded from the License.

1. 5. Rights for additional reuses such as custom editions, computer/mobile applications, film or TV reuses and/or any other derivative rights requests require additional permission and may be subject to an additional fee. Please apply to journalpermissions@springernature.com or bookpermissions@springernature.com for these rights.

2. Reservation of Rights

Licensor reserves all rights not expressly granted to you under this License. You acknowledge and agree that nothing in this License limits or restricts Licensor's rights in or use of the Licensed Material in any way. Neither this License, nor any act, omission, or statement by Licensor or you, conveys any ownership right to you in any Licensed Material, or to any element or portion thereof. As between Licensor and you, Licensor owns and retains all right, title, and interest in and to the Licensed Material subject to the license granted in Section 1.1. Your permission to use the Licensed Material is expressly conditioned on you not impairing Licensor's or the applicable copyright owner's rights in the Licensed Material in any way.

3. Restrictions on use

3. 1. Minor editing privileges are allowed for adaptations for stylistic purposes or formatting purposes provided such alterations do not alter the original meaning or intention of the Licensed Material and the new figure(s) are still accurate and representative of the Licensed Material. Any other changes including but not limited to, cropping, adapting, and/or omitting material that affect the meaning, intention or moral rights of the author(s) are strictly prohibited.

3. 2. You must not use any Licensed Material as part of any design or trademark.

3. 3. Licensed Material may be used in Open Access Publications (OAP), but any such reuse must include a clear acknowledgment of this permission visible at the same time as the figures/tables/illustration or abstract and which must indicate that the Licensed Material is not part of the governing OA license but has been reproduced with permission. This may be indicated according to any standard referencing system but must include at a minimum 'Book/Journal title, Author, Journal Name (if applicable), Volume (if applicable), Publisher, Year, reproduced with permission from SNCSC'.

4. STM Permission Guidelines

4. 1. An alternative scope of license may apply to signatories of the STM Permissions Guidelines ("STM PG") as amended from time to time and made available at https://www.stm-assoc.org/intellectual-property/permissions/permissions-guidelines/.

4. 2. For content reuse requests that qualify for permission under the STM PG, and which may be updated from time to time, the STM PG supersede the terms and conditions contained in this License.

4. 3. If a License has been granted under the STM PG, but the STM PG no longer apply at the time of publication, further permission must be sought from the Rightsholder. Contact journalpermissions@springernature.com or bookpermissions@springernature.com for these rights.

5. Duration of License

5. 1. Unless otherwise indicated on your License, a License is valid from the date of purchase ("License Date") until the end of the relevant period in the below table:

Reuse in a medical communications project	Reuse up to distribution or time period indicated in License
Reuse in a dissertation/thesis	Lifetime of thesis
Reuse in a journal/magazine	Lifetime of journal/magazine
Reuse in a book/textbook	Lifetime of edition
Reuse on a website	1 year unless otherwise specified in the License
Reuse in a presentation/slide kit/poster	Lifetime of presentation/slide kit/poster. Note: publication whether electronic or in print of presentation/slide kit/poster may require further permission.
Reuse in conference proceedings	Lifetime of conference proceedings
Reuse in an annual report	Lifetime of annual report
Reuse in training/CME materials	Reuse up to distribution or time period indicated in License
Reuse in newsmedia	Lifetime of newsmedia
Reuse in coursepack/classroom materials	Reuse up to distribution and/or time period indicated in license

6. Acknowledgement

6. 1. The Licensor's permission must be acknowledged next to the Licensed Material in print. In electronic form, this acknowledgement must be visible at the same time as the figures/tables/illustrations or abstract and must be hyperlinked to the journal/book's homepage.

6. 2. Acknowledgement may be provided according to any standard referencing system and at a minimum should include "Author, Article/Book Title, Journal name/Book imprint, volume, page number, year, Springer Nature".

7. Reuse in a dissertation or thesis

7. 1. Where 'reuse in a dissertation/thesis' has been selected, the following terms apply: Print rights of the Version of Record are provided for; electronic rights for use only on institutional repository as defined by the Sherpa guideline (www.sherpa.ac.uk/romeo/) and only up to what is required by the awarding institution.

7. 2. For theses published under an ISBN or ISSN, separate permission is required. Please contact journalpermissions@springernature.com or bookpermissions@springernature.com for these rights.

7. 3. Authors must properly cite the published manuscript in their thesis according to current citation standards and include the following acknowledgement: '*Reproduced with permission from Springer Nature*'.

8. License Fee

You must pay the fee set forth in the License Agreement (the "License Fees"). All amounts payable by you under this License are exclusive of any sales, use, withholding, value added or similar taxes, government fees or levies or other assessments. Collection and/or remittance of such taxes to the relevant tax authority shall be the responsibility of the party who has the legal obligation to do so.

9. Warranty

9. 1. The Licensor warrants that it has, to the best of its knowledge, the rights to license reuse of the Licensed Material. **You are solely responsible for ensuring that the material you wish to license is original to the Licensor and does not carry the copyright of another entity or third party (as credited in the published version).** If the credit line on any part of the Licensed Material indicates that it was reprinted or adapted with permission from another source, then you should seek additional permission from that source to reuse the material.

9. 2. EXCEPT FOR THE EXPRESS WARRANTY STATED HEREIN AND TO THE EXTENT PERMITTED BY APPLICABLE LAW, LICENSOR PROVIDES THE LICENSED MATERIAL "AS IS" AND MAKES NO OTHER REPRESENTATION OR WARRANTY. LICENSOR EXPRESSLY DISCLAIMS ANY LIABILITY FOR ANY CLAIM ARISING FROM OR OUT OF THE CONTENT, INCLUDING BUT NOT LIMITED TO ANY ERRORS, INACCURACIES, OMISSIONS, OR DEFECTS CONTAINED THEREIN, AND ANY IMPLIED OR EXPRESS WARRANTY AS TO MERCHANTABILITY OR FITNESS FOR A PARTICULAR PURPOSE. IN NO EVENT SHALL LICENSOR BE LIABLE TO YOU OR ANY OTHER PARTY OR ANY OTHER PERSON OR FOR ANY SPECIAL, CONSEQUENTIAL, INCIDENTAL, INDIRECT, PUNITIVE, OR EXEMPLARY DAMAGES, HOWEVER CAUSED, ARISING OUT OF OR IN CONNECTION WITH THE DOWNLOADING, VIEWING OR USE OF THE LICENSED MATERIAL REGARDLESS OF THE FORM OF ACTION, WHETHER FOR BREACH OF CONTRACT, BREACH OF WARRANTY, TORT, NEGLIGENCE, INFRINGEMENT OR OTHERWISE (INCLUDING, WITHOUT LIMITATION, DAMAGES BASED ON LOSS OF PROFITS, DATA, FILES, USE, BUSINESS OPPORTUNITY OR CLAIMS OF THIRD PARTIES), AND WHETHER OR NOT THE PARTY HAS BEEN ADVISED OF THE POSSIBILITY OF SUCH DAMAGES. THIS LIMITATION APPLIES NOTWITHSTANDING ANY FAILURE OF ESSENTIAL PURPOSE OF ANY LIMITED REMEDY PROVIDED HEREIN.

10. Termination and Cancellation

10. 1. The License and all rights granted hereunder will continue until the end of the applicable period shown in Clause 5.1 above. Thereafter, this license will be terminated and all rights granted hereunder will cease.

10. 2. Licensor reserves the right to terminate the License in the event that payment is not received in full or if you breach the terms of this License.

11. General

11. 1. The License and the rights and obligations of the parties hereto shall be construed, interpreted and determined in accordance with the laws of the Federal Republic of Germany without reference to the stipulations of the CISG (United Nations Convention on Contracts for the International Sale of Goods) or to Germany´s choice-of-law principle.

11. 2. The parties acknowledge and agree that any controversies and disputes arising out of this License shall be decided exclusively by the courts of or having jurisdiction for Heidelberg, Germany, as far as legally permissible.

11. 3. This License is solely for Licensor's and Licensee's benefit. It is not for the benefit of any other person or entity.

Questions? For questions on Copyright Clearance Center accounts or website issues please contact springernaturesupport@copyright.com or +1-855-239-3415 (toll free in the US) or +1-978-646-2777. For questions on Springer Nature licensing please visit https://www.springernature.com/gp/partners/rights-permissions-third-party-distribution

Other Conditions:

Version 1.4 - Dec 2022

Questions? customercare@copyright.com.

American Physical Society
Reuse and Permissions License

25-Jan-2023

This license agreement between the American Physical Society ("APS") and Andrew Killeen ("You") consists of your license details and the terms and conditions provided by the American Physical Society and SciPris.

Licensed Content Information

License Number:	**RNP/23/JAN/062471**
License date:	25-Jan-2023
DOI:	10.1103/PhysRevLett.114.228102
Title:	Emergence and Persistence of Collective Cell Migration on Small Circular Micropatterns
Author:	Felix J. Segerer et al.
Publication:	Physical Review Letters
Publisher:	American Physical Society
Cost:	USD $ 0.00

Request Details

Does your reuse require significant modifications: No

Specify intended distribution locations:	Worldwide
Reuse Category:	Reuse in a thesis/dissertation
Requestor Type:	Student
Items for Reuse:	Figures/Tables
Number of Figure/Tables:	1
Figure/Tables Details:	Supplementary Figure 1
Format for Reuse:	Electronic

Information about New Publication:

University/Publisher:	Imperial College London
Title of dissertation/thesis:	Emergent dynamics of confluent tissues in homeostasis and growth
Author(s):	Andrew Killeen
Expected completion date:	Mar. 2023

License Requestor Information

Name:	Andrew Killeen
Affiliation:	Individual
Email Id:	
Country:	United Kingdom

American Physical Society
Reuse and Permissions License

TERMS AND CONDITIONS

The American Physical Society (APS) is pleased to grant the Requestor of this license a non-exclusive, non-transferable permission, limited to Electronic format, provided all criteria outlined below are followed.

1. You must also obtain permission from at least one of the lead authors for each separate work, if you haven't done so already. The author's name and affiliation can be found on the first page of the published Article.
2. For electronic format permissions, Requestor agrees to provide a hyperlink from the reprinted APS material using the source material's DOI on the web page where the work appears. The hyperlink should use the standard DOI resolution URL, http://dx.doi.org/{DOI}. The hyperlink may be embedded in the copyright credit line.
3. For print format permissions, Requestor agrees to print the required copyright credit line on the first page where the material appears: "Reprinted (abstract/excerpt/figure) with permission from [(FULL REFERENCE CITATION) as follows: Author's Names, APS Journal Title, Volume Number, Page Number and Year of Publication.] Copyright (YEAR) by the American Physical Society."
4. Permission granted in this license is for a one-time use and does not include permission for any future editions, updates, databases, formats or other matters. Permission must be sought for any additional use.
5. Use of the material does not and must not imply any endorsement by APS.
6. APS does not imply, purport or intend to grant permission to reuse materials to which it does not hold copyright. It is the requestor's sole responsibility to ensure the licensed material is original to APS and does not contain the copyright of another entity, and that the copyright notice of the figure, photograph, cover or table does not indicate it was reprinted by APS with permission from another source.
7. The permission granted herein is personal to the Requestor for the use specified and is not transferable or assignable without express written permission of APS. This license may not be amended except in writing by APS.
8. You may not alter, edit or modify the material in any manner.
9. You may translate the materials only when translation rights have been granted.
10. APS is not responsible for any errors or omissions due to translation.
11. You may not use the material for promotional, sales, advertising or marketing purposes.
12. The foregoing license shall not take effect unless and until APS or its agent, Aptara, receives payment in full in accordance with Aptara Billing and Payment Terms and Conditions, which are incorporated herein by reference.
13. Should the terms of this license be violated at any time, APS or Aptara may revoke the license with no refund to you and seek relief to the fullest extent of the laws of the USA. Official written notice will be made using the contact information provided with the permission request. Failure to receive such notice will not nullify revocation of the permission.
14. APS reserves all rights not specifically granted herein.
15. This document, including the Aptara Billing and Payment Terms and Conditions, shall be the entire agreement between the parties relating to the subject matter hereof.

American Physical Society
Reuse and Permissions License

25-Jan-2023

This license agreement between the American Physical Society ("APS") and Andrew Killeen ("You") consists of your license details and the terms and conditions provided by the American Physical Society and SciPris.

Licensed Content Information

License Number:	**RNP/23/JAN/062467**
License date:	25-Jan-2023
DOI:	10.1103/PhysRevLett.128.078001
Title:	Polar Fluctuations Lead to Extensile Nematic Behavior in Confluent Tissues
Author:	Andrew Killeen, Thibault Bertrand, and Chiu Fan Lee
Publication:	Physical Review Letters
Publisher:	American Physical Society
Cost:	USD $ 0.00

Request Details

Does your reuse require significant modifications: Yes

Modification Details:

Yes, I am the lead author and have permission from the other authors

Specify intended distribution locations:	Worldwide
Reuse Category:	Reuse in a thesis/dissertation
Requestor Type:	Author of requested content
Items for Reuse:	Whole Article
Format for Reuse:	Electronic

Information about New Publication:

University/Publisher:	Imperial College London
Title of dissertation/thesis:	Emergent dynamics of confluent tissues in homeostasis and growth
Author(s):	Andrew Killeen
Expected completion date:	Mar. 2023

License Requestor Information

Name:	Andrew Killeen
Affiliation:	Individual
Email Id:	
Country:	United Kingdom

American Physical Society
Reuse and Permissions License

TERMS AND CONDITIONS

The American Physical Society (APS) is pleased to grant the Requestor of this license a non-exclusive, non-transferable permission, limited to Electronic format, provided all criteria outlined below are followed.

1. You must also obtain permission from at least one of the lead authors for each separate work, if you haven't done so already. The author's name and affiliation can be found on the first page of the published Article.
2. For electronic format permissions, Requestor agrees to provide a hyperlink from the reprinted APS material using the source material's DOI on the web page where the work appears. The hyperlink should use the standard DOI resolution URL, http://dx.doi.org/{DOI}. The hyperlink may be embedded in the copyright credit line.
3. For print format permissions, Requestor agrees to print the required copyright credit line on the first page where the material appears: "Reprinted (abstract/excerpt/figure) with permission from [(FULL REFERENCE CITATION) as follows: Author's Names, APS Journal Title, Volume Number, Page Number and Year of Publication.] Copyright (YEAR) by the American Physical Society."
4. Permission granted in this license is for a one-time use and does not include permission for any future editions, updates, databases, formats or other matters. Permission must be sought for any additional use.
5. Use of the material does not and must not imply any endorsement by APS.
6. APS does not imply, purport or intend to grant permission to reuse materials to which it does not hold copyright. It is the requestor's sole responsibility to ensure the licensed material is original to APS and does not contain the copyright of another entity, and that the copyright notice of the figure, photograph, cover or table does not indicate it was reprinted by APS with permission from another source.
7. The permission granted herein is personal to the Requestor for the use specified and is not transferable or assignable without express written permission of APS. This license may not be amended except in writing by APS.
8. You may not alter, edit or modify the material in any manner.
9. You may translate the materials only when translation rights have been granted.
10. APS is not responsible for any errors or omissions due to translation.
11. You may not use the material for promotional, sales, advertising or marketing purposes.
12. The foregoing license shall not take effect unless and until APS or its agent, Aptara, receives payment in full in accordance with Aptara Billing and Payment Terms and Conditions, which are incorporated herein by reference.
13. Should the terms of this license be violated at any time, APS or Aptara may revoke the license with no refund to you and seek relief to the fullest extent of the laws of the USA. Official written notice will be made using the contact information provided with the permission request. Failure to receive such notice will not nullify revocation of the permission.
14. APS reserves all rights not specifically granted herein.
15. This document, including the Aptara Billing and Payment Terms and Conditions, shall be the entire agreement between the parties relating to the subject matter hereof.